(NASA-CR-4179) AN ADVANCED ACTUATOR FOR HIGH-PERFORMANCE SLEWING Final Report (SatCon Technology Corp.) 163 p CSCL 13I

N89-11921

Unclas
H1/31 0158879

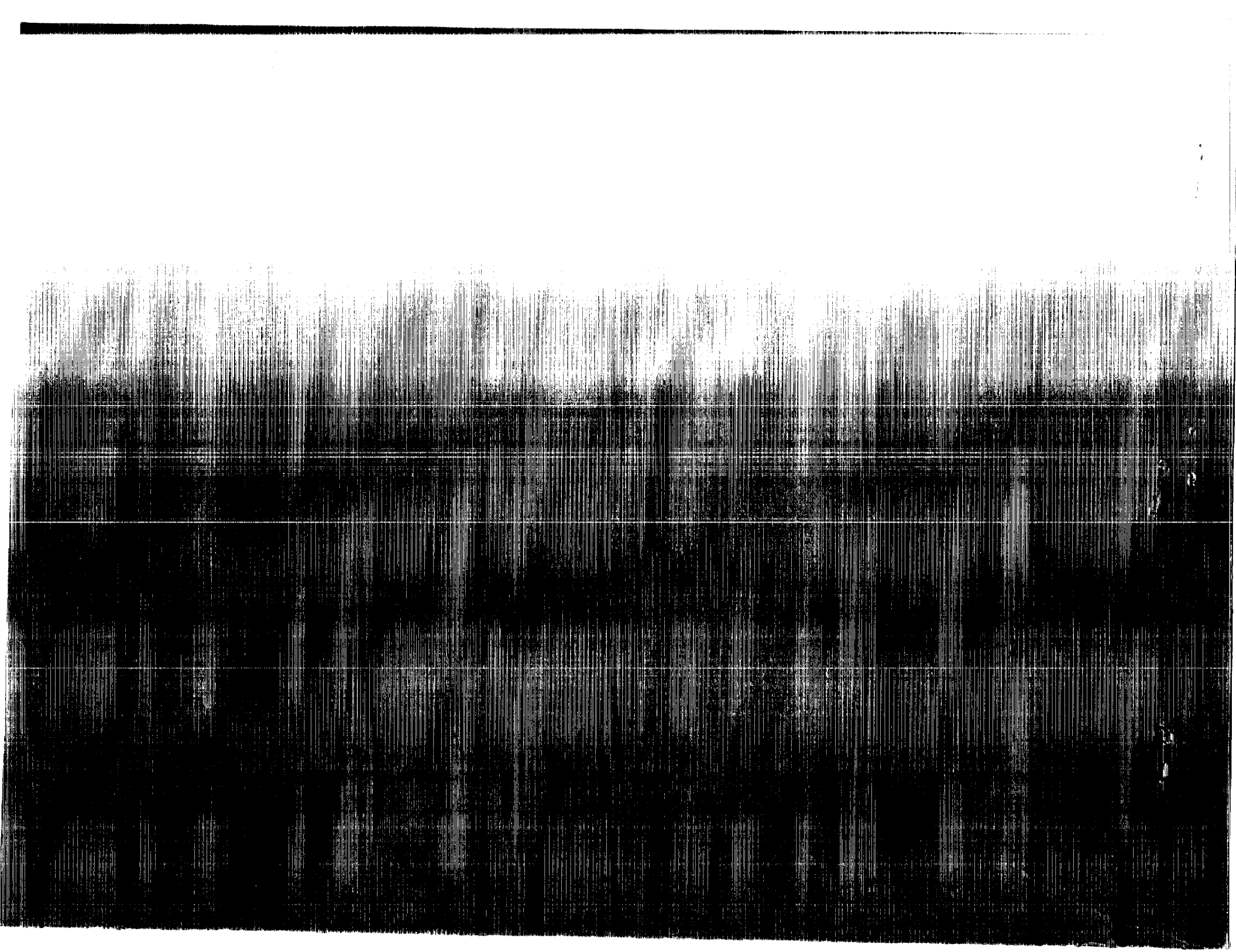

NASA Contractor Report 4179

An Advanced Actuator for High-Performance Slewing

James Downer, David Eisenhaure,
and Richard Hockney
SatCon Technology Corporation
Cambridge, Massachusetts

Prepared for
Langley Research Center
under Contract NAS1-18322

National Aeronautics
and Space Administration

**Scientific and Technical
Information Division**

1988

SUMMARY

This report describes a conceptual design for an advanced momentum-exchange type of slew actuator. The actuator is a magnetically-suspended and magnetically-gimballed control moment gyro (CMG). A scissored-pair of these CMGs is sized to provide the torque and angular momentum required to reorient a large spacecraft or other space-based payload through a large angle (a slew maneuver). The control-torque and angular-momentum storage required for rigid-body slewing of such large spacecraft are substantially greater than the capabilities of available momentum-exchange actuators which implies that a reaction-control (thruster) system would typically be employed.

The slew actuator described in this report would be used in large-spacecraft slewing applications where the disadvantages of reaction-control systems cannot be tolerated. In order to meet the requirements of slewing large spacecraft, a number of advanced component technologies have been employed in the design of the actuator. Each of the individual technologies is mature, but is not used in the design of conventional CMGs.

The angular-momentum storage device (flywheel) of available CMGs is typically made from a high-strength metal such as maraging steel. Advanced composite materials such as high-strength graphite fibers in an epoxy matrix, however, have much greater angular-momentum density.

The use of magnetic bearings in angular momentum exchange effectors has the primary advantage that physical contact between the rotor and stator is eliminated. This leads to greatly extended life, increased reliability, and reduced vibrations. The advanced CMG uses an alternative magnetic bearing design which employs a superconducting coil and eliminates all conventional magnetic structures in order to produce an energy-efficient, light-weight design.

The design of the advanced CMG uses several components to perform more than one function. An alternative to the use of conventional gimbal structures and torquers is to consolidate the functions of conventional bearing and gimbal systems. A large-angle magnetic suspension is a five-axes, actively-controlled magnetic bearing which is designed to accommodate angular motion about the lateral axes of the flywheel. The magnetic bearing is described in this report is an extension to this technology. The superconducting coil also provides the field excitation for an axial-air-gap spin motor.

PRECEDING PAGE BLANK NOT FILMED

PAGE ii INTENTIONALLY BLANK

ACKNOWLEDGEMENT

The research presented in this final report was prepared under Task B (An Advanced Momentum Exchange Effector for High Performance Pointing Applications) of NASA Contract NAS1-18322 (Analysis of Active Control of Magnetic Systems). This research was administered by the NASA Langley Research Center.

The authors would like to acknowledge the guidance provided by Claude Keckler of NASA Langley, the technical monitor for Tasks A and B of the contract.

PRECEDING PAGE BLANK NOT FILMED

PAGE iv INTENTIONALLY BLANK

TABLE OF CONTENTS

PRECEDING PAGE BLANK NOT FILMED

PAGE vi INTENTIONALLY BLANK

TABLE OF CONTENTS (Cont'd)

LIST OF ILLUSTRATIONS

List of Illustrations (Cont'd)

LIST OF TABLES

1. INTRODUCTION

This report documents a design definition study for an advanced momentum-exchange type of slew actuator. The actuator, shown in Figure 1, is a magnetically-suspended and gimballed control moment gyro (CMG). A scissored-pair of these CMGs is sized to provide the torque and angular momentum required to reorient a large spacecraft or other space-based payload through a large angle (a slew maneuver). Large spacecraft are defined as those having moments of inertia on the order of 100 $kNms^2$ (100,000 kgm^2). The control torque (27 kNm) and angular momentum storage (45 kNms) required for rigid-body slewing of such large spacecraft are substantially greater than the capabilities of available momentum-exchange actuators [1, 2, 3] which implies that a reaction-control (thruster) system would typically be employed.

The slew actuator described in this report would be used in large-spacecraft slewing applications where the disadvantages of reaction-control systems cannot be tolerated. Reaction-control systems expel a pressurized fluid in order to apply torque to a spacecraft. The mission life of the spacecraft is therefore limited by the amount of fluid which may be stored. The fluid expelled by the reaction-control system (effluent) may also be detrimental to on-board optics. Both of these disadvantages are eliminated by the use of a momentum-exchange effector.

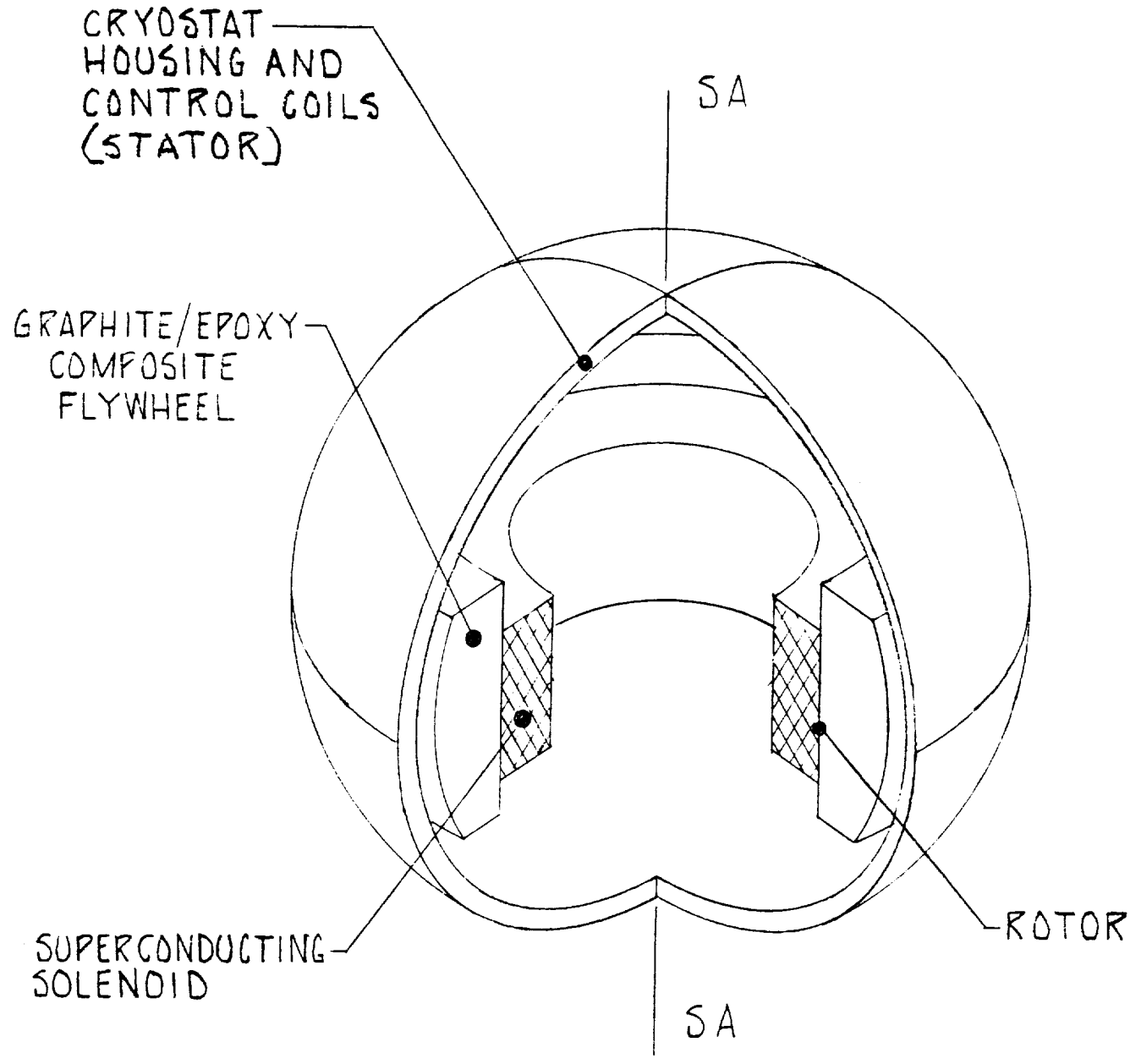

Figure 1. Advanced-concept Control Moment Gyro

In order to meet the requirements of slewing large spacecraft, a number of advanced component technologies have been employed in the design of the actuator. Each of the individual technologies is relatively mature, but is not used in the design of conventional CMGs.

The angular-momentum storage device (flywheel) of available CMGs is typically made from a high-strength metal such as maraging steel [1]. Advanced composite materials such as high-strength graphite fibers in an epoxy matrix, however, have much greater angular-momentum density (angular momentum per unit mass).

The use of magnetic bearings in angular momentum exchange effectors has the primary advantage that physical contact between the rotor and stator is eliminated. This leads to greatly extended life, increased reliability, and reduced vibrations. Although several magnetically-suspended momentum-exchange actuators have been advertised [3] and in one case flown [4], the vast majority are supported by mechanical bearings. The actuators which operated on magnetic bearings were sized for use in small satellites. For conventional magnetic bearings, which employ magnetic cores, high mechanical loading may require that the magnetic structure be excessively large.

The advanced CMG uses an alternative magnetic bearing design which employs a superconducting coil and eliminates all conventional magnetic structures. The baseline approach is to replace the magnetic structure of a conventional magnetic bearing

with a superconducting coil. In the superconducting magnetic bearing, a single coil replaces two permanent magnet structures in order to produce an energy-efficient, light-weight design.

The design of the advanced CMG uses several components to perform more than one function. An alternative to the use of conventional gimbal structures and torquers is to consolidate the functions of conventional bearing and gimbal systems. A large-angle magnetic suspension (LAMS) is a five-axes, actively-controlled magnetic bearing which is designed to accommodate angular motion about the lateral axes of the flywheel [5]. The magnetic bearing is described in this report is an extension to this technology. The superconducting coil also provides the field excitation for an axial-air-gap spin motor.

1.1 Overview of the Study

This section describes the approach which was taken for this design definition study. Initially a set of requirements for the slew actuator were identified through a combination of first-order analysis and discussions with other researchers in the field. Specifications for torque, angular momentum storage, and mechanical power transfer capabilities were determined.

Alternate types and array configurations of momentum-exchange actuators were considered. A novel approach, the "constant-energy array", was also analyzed. The state-of-the-art in various component technologies was established through literature surveys and analysis. The key components were high-

performance flywheel rotors, magnetic bearings (conventional and advanced designs), as well as spin motors.

The design definition for the baseline slew actuator was determined through trade-off analysis of the various actuator types, actuator array configurations, and components. The final choice, scissored pairs of advanced technology CMGs, was selected based on considerations of mass and power consumption during the delivery of maximum torque.

1.2 Performance of the Slew Actuator

Table I contains the performance parameters (mass and power consumption) for the key components of the slew actuator. These represent a vast improvement over what could be achieved with more conventional technology.

Table I. Slew Actuator Performance

Control Torque	27 kNm
Angular Momentum	45 kNms
Mass	1,027 kg
Power	1,106 W

1.3 Organization of the Report

The remainder of this report documents the design definition study. Chapter 2 presents the assessment of the slew actuator requirements. Chapter 3 identifies alternate actuator types and possible configurations for the actuator arrays. Chapters 4-7 analyze alternate component technologies. Flywheel rotors are discussed in Chapter 4. Conventional and superconducting

magnetic bearings are discussed in Chapters 5 and 6 respectively. A survey of conventional spin motors and their compatibility with the field of the superconducting magnetic bearing is included in Chapter 7. Chapter 8 contains conclusions and recommendations for further work. Whenever possible, analytical detail and sample calculations have been summarized in appendices.

2. SLEW ACTUATOR REQUIREMENTS ASSESSMENT

This chapter discusses the development of specifications for the slew actuator. The items of interest consist of the maximum values of control torque, angular momentum storage capacity, and mechanical power transfer to the load. In addition, a set of parameters which describe the trajectory for a typical slewing maneuver (the angle through which the payload must be moved and the time allowed) were developed. Table II below summarizes the results of the requirements assessment survey.

Table II. Slew Actuator Requirements

Trajectory Parameters	
Slew Angle	1 rad.
Slew Time	4.4 sec.
Actuator Requirements	
Max. Control Torque	27 kNm
Max. Angular Momentum	45 kNms
Max. Mechanical Power	9.4 kW

2.1 Approach for the Requirements Assessment

These specifications were developed through a combination of a literature survey, first-order analysis, and direct discussions with other researchers in the field. The initial literature survey and discussions focused on early studies of slew maneuvers for rigid space-based payloads. Typical payload inertias and methods (such as command shaping) for dealing with the inherent flexibility of the payload were of particular interest. Early estimates of "typical" requirements for slewing were also disclosed. Given baseline payload inertias, slew requirements,

and techniques for command shaping, a single-axis model was developed and analyzed. More recent techniques for dealing with the flexibility of payloads indicate that the early torque estimate may have been somewhat high and was reduced accordingly. The resulting slew actuator requirements were presented at the mid-term program review. Following this review, the requirements were again revised downward.

2.2 Initial Literature Survey and Technical Discussions

As an initial step toward the development of specifications for the slew actuator, a survey of available literature and a series of discussions with researchers in the field of large space structures were performed. These disclosed an existing assessment of typical requirements for slewing large space structures [6], a procedure for dealing with the flexibility of large payloads, and a baseline payload. This section documents this background material.

2.2.1 Typical Specifications for Slewing Maneuvers

Reference 6 is considered to be the most complete survey of the requirements for large precision space structures. This document contains preliminary estimates for the requirements of large-angle retargeting and slewing. Figure 2 is a reproduction of Figure 7 of Reference 6. This is a mapping in torque-momentum space of the capabilities of existing actuators and of areas where additional development is needed. "Typical" requirements

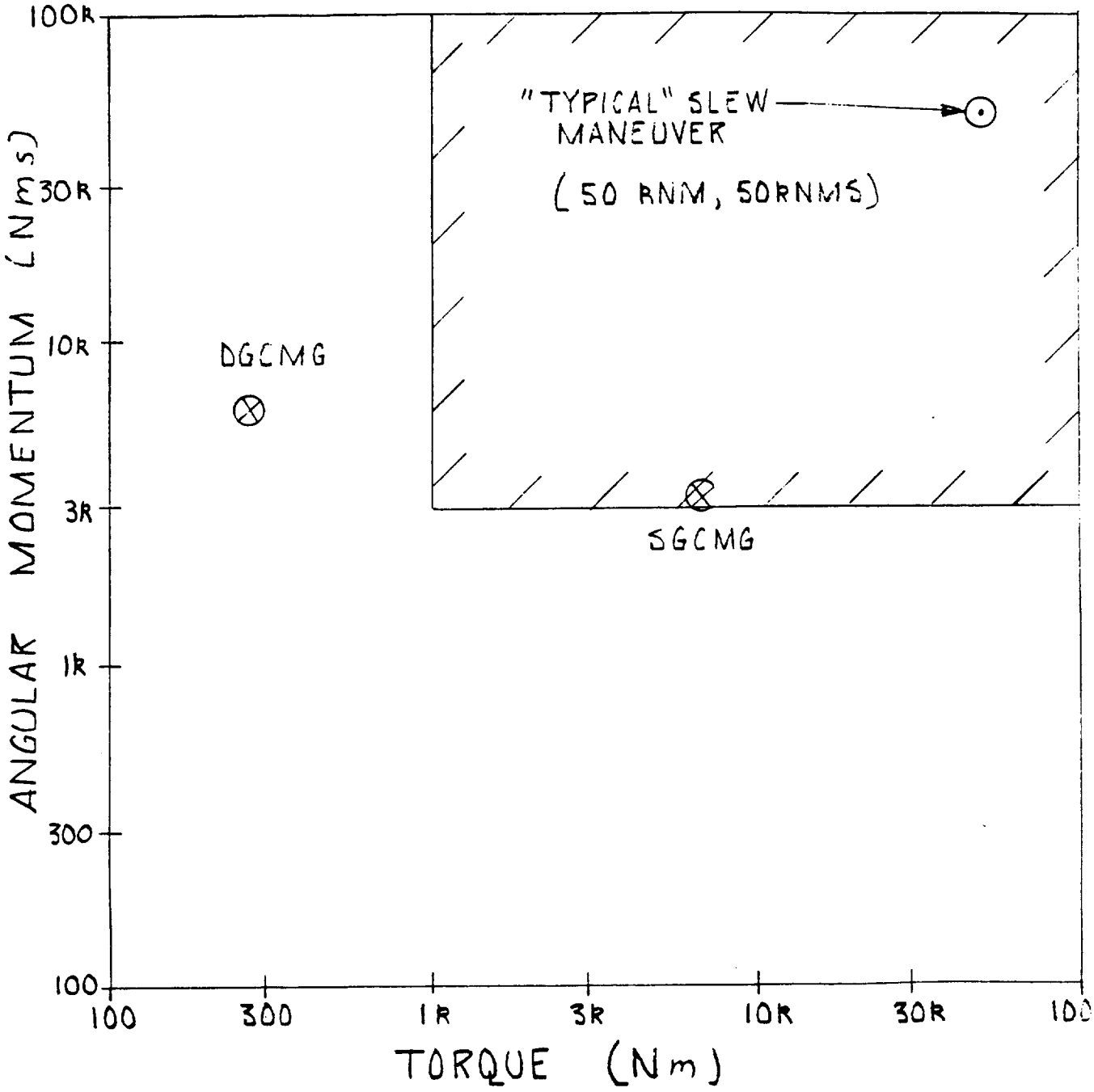

Figure 2. Typical Slewing Requirements

for slewing of large space structures are shown in the upper right-hand corner of the figure. This combination occurs at a point which is approximately 50 kNm of torque and 50 kNms of angular momentum.

2.2.2 Command Shaping

Reference 6 also describes the principal need for slewing large space structures as the development of open- and closed-loop control laws to reduce flexible mode interactions. Closed-loop algorithms for reducing the vibration amplitude of an arbitrary number of structural modes at the end of a rotational maneuver have been presented in the literature [7].

An alternative technique is to smooth the torque profile applied to the payload. This technique for reducing vibrations is referred to as analog pre-filtering or command shaping. The primary effect of command shaping on the requirements for the slew actuator is an increase in the peak control torque which is required for a given slew maneuver. During the survey phase of the program, a total of eight command shapes were identified and analyzed. The results of the analysis are presented in Section 2.3.

2.2.3 Baseline Payload

Reference 8 describes the forward body of a typical high energy laser (HEL). The payload was intended as a strawman to be used for the development of a Space Active Vibration Isolator

(SAVI) and will be referred to in this report as the SAVI payload. The inertial properties for the SAVI payload, which is shown schematically in Figure 3, and the torque requirement for the isolator are given in Table III below.

Table III. SAVI Properties

<u>Inertial Properties</u>	
Forward-body Mass	6000 kg
Forward-body Inertia	100 $kNms^2$
<u>Other Properties</u>	
Control Torque	27 kNm

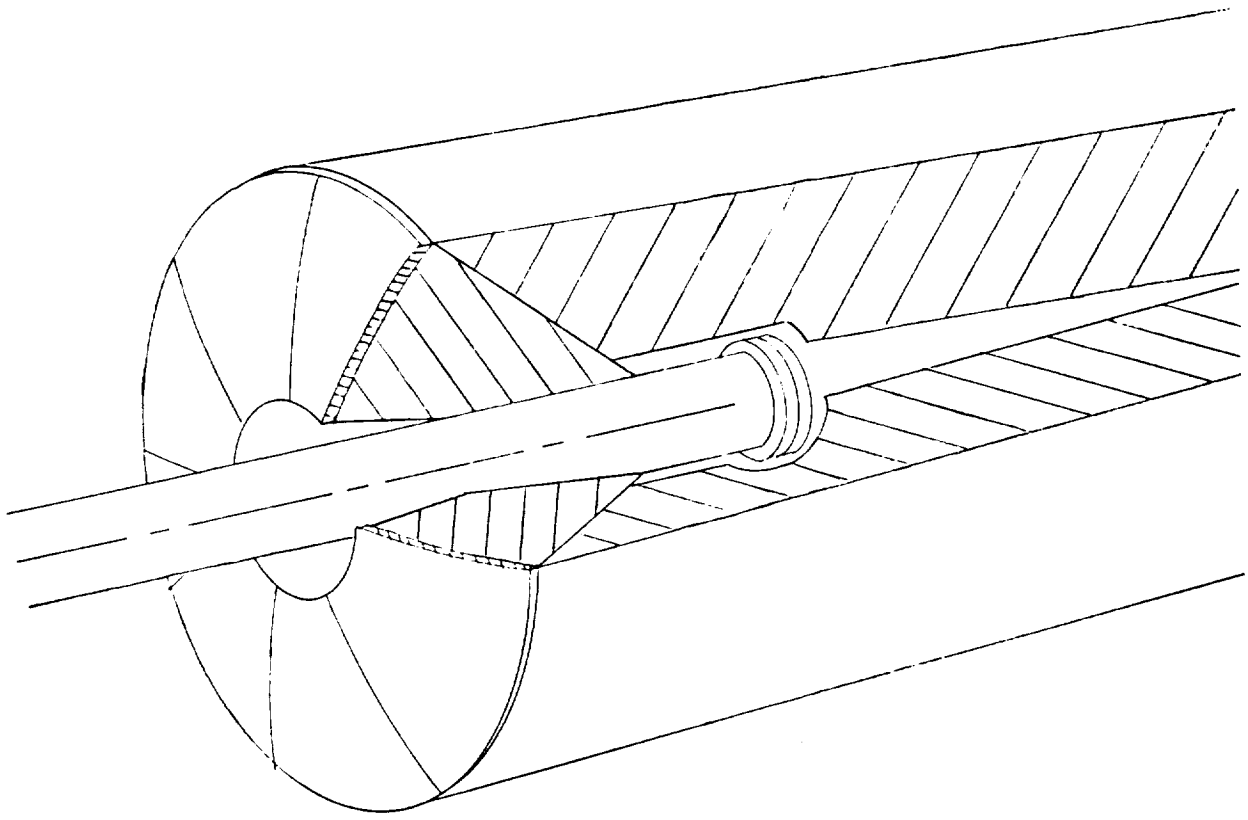

Figure 3. SAVI Payload

2.3 Slew Maneuver Analysis

Section A.1 of Appendix A presents a sample calculation for the motion of a rigid payload during a slew maneuver. It is assumed that a constant torque accelerates the inertia (I_s) of the payload for half of the slew period. During this acceleration period, the spacecraft will gain angular momentum. An equal but opposite torque is then applied in order to decelerate the spacecraft. This is referred to as a "bang-bang" command shape. The final result of the first section of the appendix is a set of equations which relate the maximum torque (τ_{cm}), angular momentum (H_m), and mechanical power (P_m) to the slew angle (θ_s) and time (T_s). These equations are summarized below.

$$\theta_s,\ T_s = \text{Given} \tag{2.1a}$$

$$\tau_{cm} = \frac{4I_s\theta_s}{T_s^2} \tag{2.1b}$$

$$H_m = \frac{2I_s\theta_s}{T_s} \tag{2.1c}$$

$$P_m = \frac{8I_s\theta_s^2}{T_s^3} \tag{2.1d}$$

Angle, angular momentum and torque trajectories for the bang-bang slew profile are shown in Figure 4. Equations 2.1 are readily normalized with respect to the slew maneuver parameters.

$$\tau_{cn} = \frac{\tau_{cm}T_s^2}{I_s\theta_s} \tag{2.2a}$$

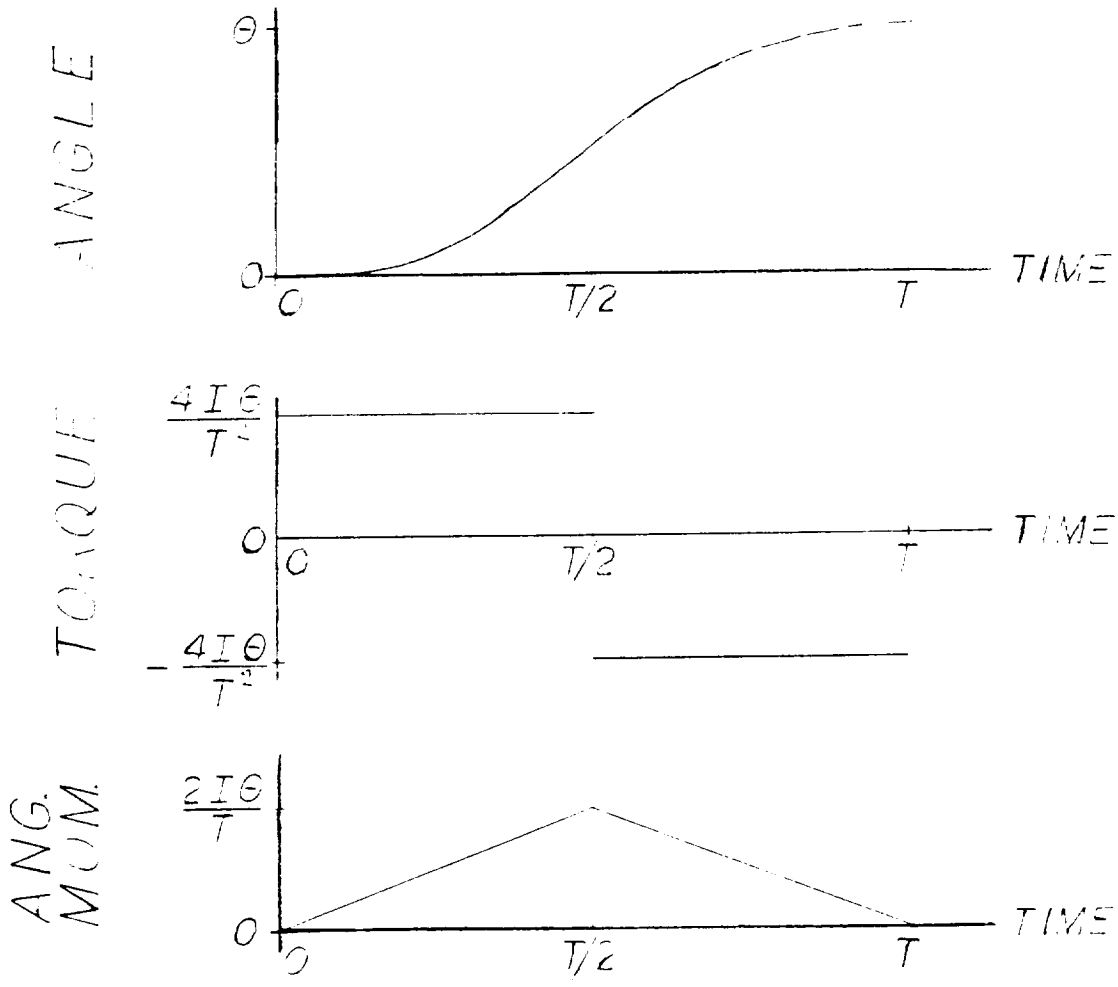

ORIGINAL PAGE IS
OF POOR QUALITY

Figure 4. Bang-bang Slew Profile

$$H_n = \frac{H_m T_s}{I_s \theta_s} \qquad (2.2b)$$

$$P_n = \frac{P_m T_s^3}{I_s \theta_s^2} \qquad (2.2c)$$

A smoother command shape is typically employed to reduce vibrations. The command shapes may be discontinuous, trigonometric, or polynomial in form. An identical analysis to that presented in Section A.1 was performed for each of the other command shapes. Typical command shapes were suggested by Dr. Keto Soosar, Dr. James Turner, and Ms. Laura Larkin of Photon Research Associates, Inc. and are discussed in the paragraphs which follow.

2.3.1 Discontinuous Command Shapes

In addition to the bang-bang profile, there is one other common discontinuous command shape. A constant torque accelerates the payload for the first third of the maneuver period. The payload then coasts at constant angular momentum for the middle third of the maneuver. Finally, the payload is decelerated to rest in the last third of the maneuver period. This profile is referred to as a "bang-rest-bang" command shape. Figures 5(a), 5(b), 5(c), and 5(d) present the normalized angle, angular momentum, torque, and power trajectories for the two command shapes. The bang-rest-bang command shape requires additional torque but reduced angular momentum and power.

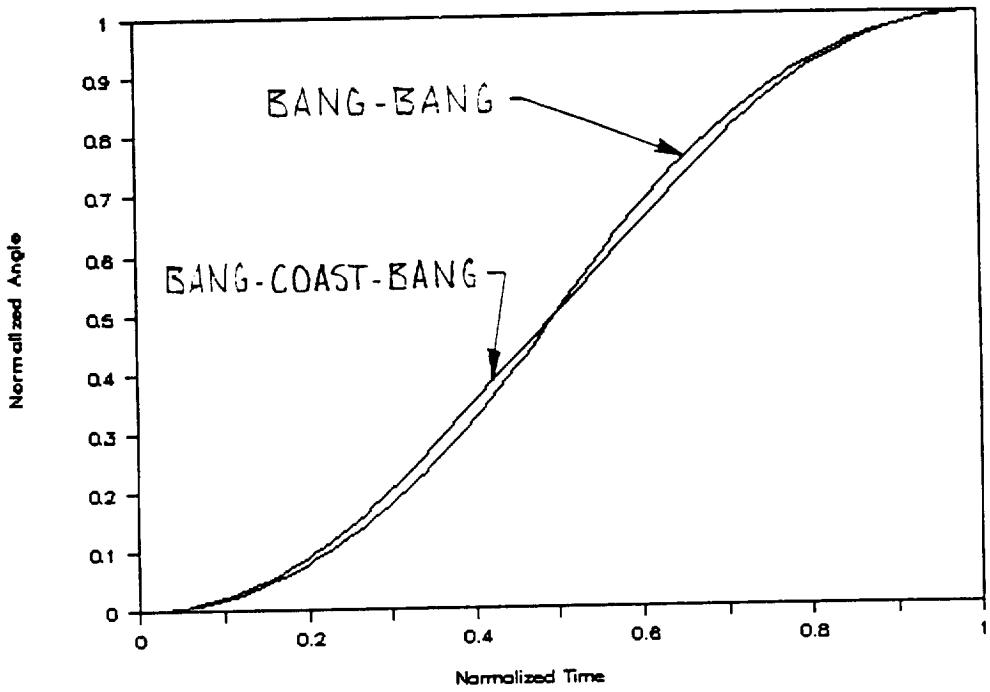

a) Angle

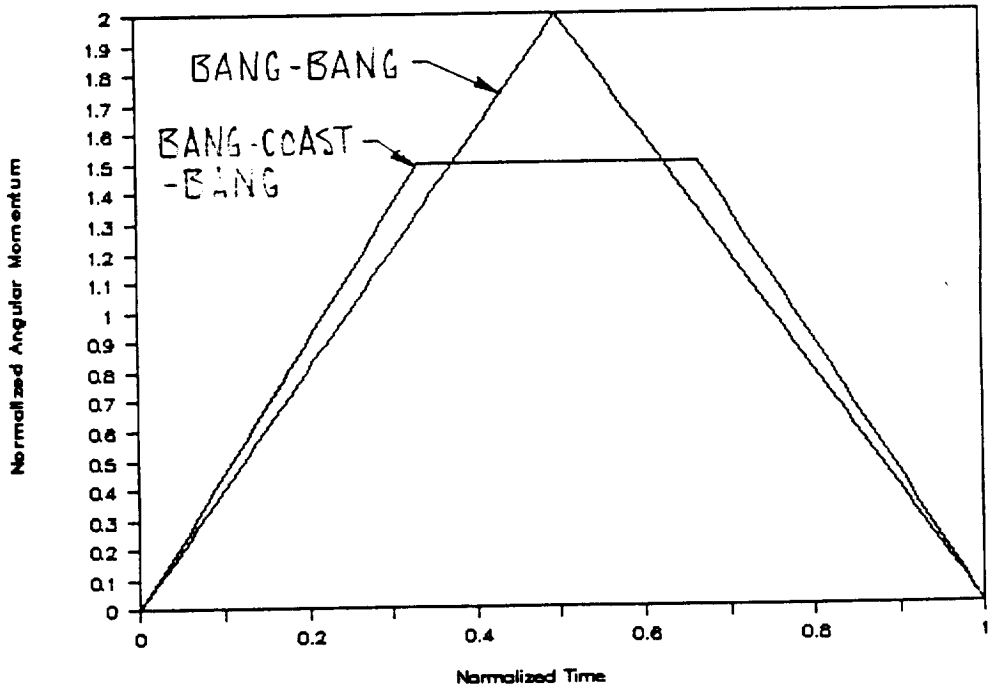

b) Angular Momentum

Figure 5. Normalized Discontinuous Command Shapes

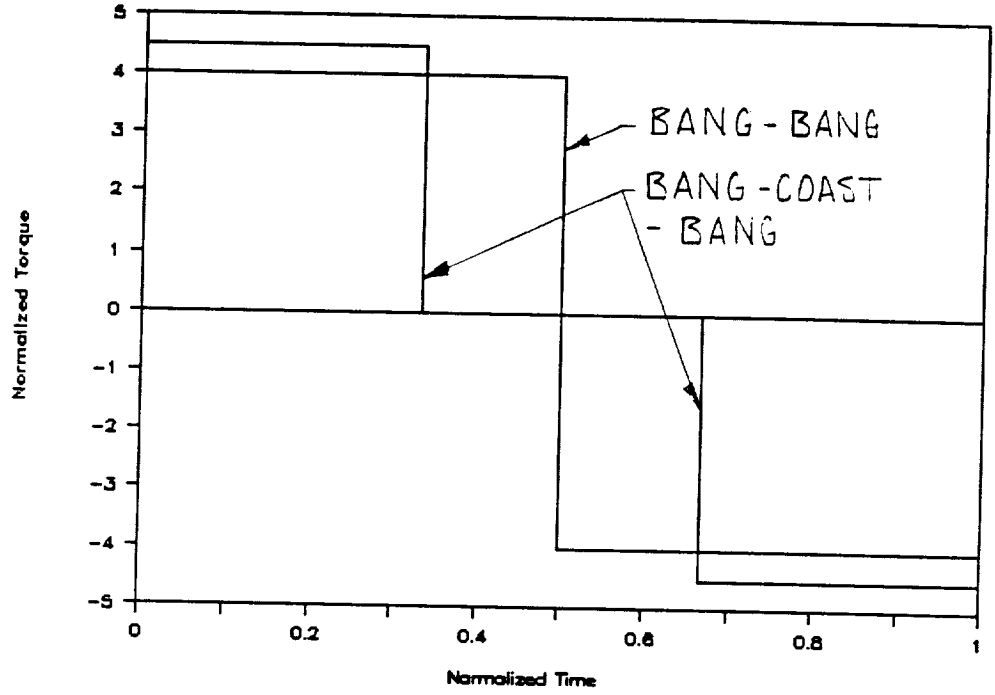

c) Torque

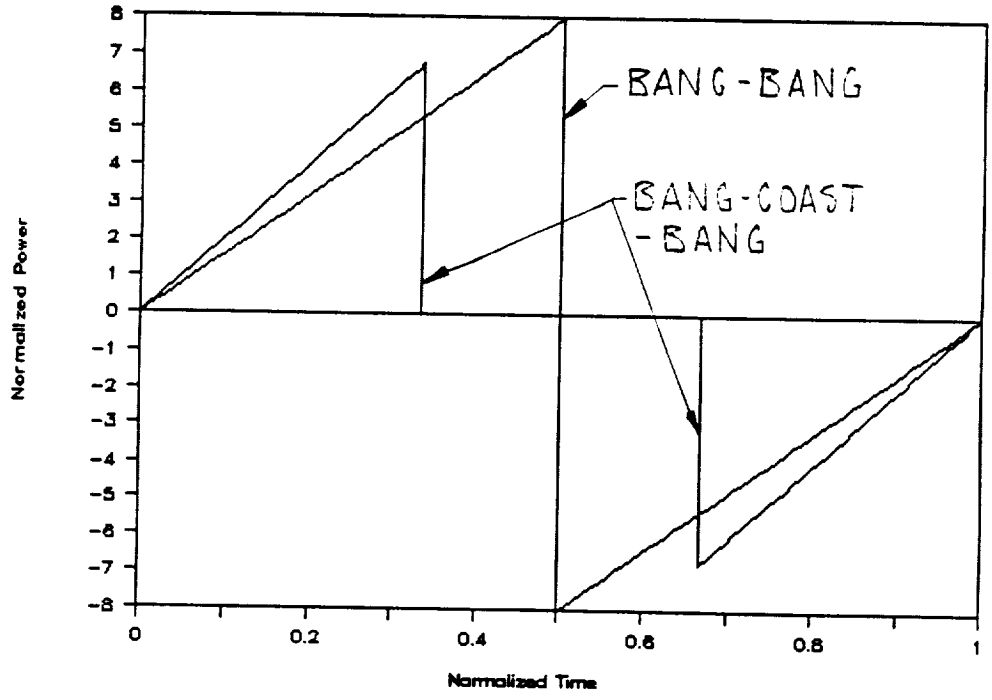

d) Mechanical Power

Figure 5. Normalized Discontinuous Command Shapes (Cont'd)

ORIGINAL PAGE IS
OF POOR QUALITY

2.3.2 Trigonometric Command Shapes

The torque applied to the payload may also take the shape of a trigonometric function such as a sine-wave or a double versine (1 - cosine). Figures 6(a), 6(b), 6(c), and 6(d) present the normalized angle, angular momentum, torque, and power trajectories for the two trigonometric command shapes. The double versine command shape requires the greater torque and mechanical power. Both of the trigonometric command shapes require identical angular momentum storage capacity.

2.3.3 Polynomial Command Shapes

One particularly simple command shape is a polynomial. Two polynomials, fifth and seventh order were considered. The coefficients of the terms in the polynomials are determined by kinematic constraints. The angular position of the payload is set to zero at the beginning of the maneuver and to the slew angle (θ_S) at the end. The initial and final velocities and accelerations of the payload were also set to zero. The additional two constraints available for the seventh-order polynomial are provided by setting the initial and final rate of change of acceleration (angular jerk) to zero. Figures 7(a), 7(b), 7(c), and 7(d) present the normalized angle, angular momentum, torque, and power trajectories for the two polynomial command shapes. The requirements for the polynomial command shapes are intermediate between those of the discontinuous and trigonometric command shapes.

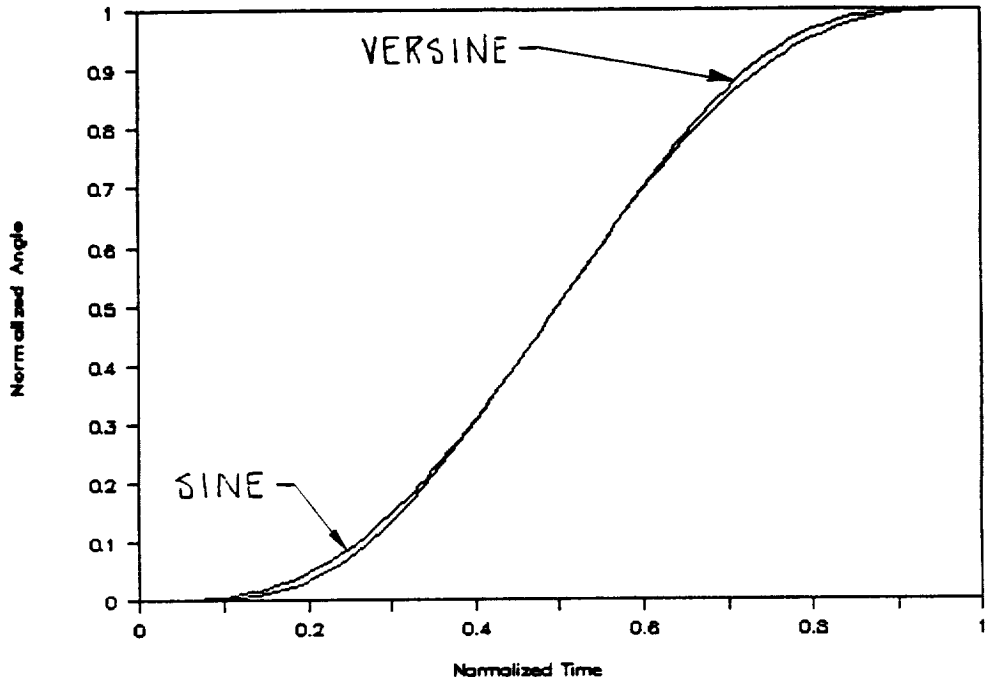

a) Angle

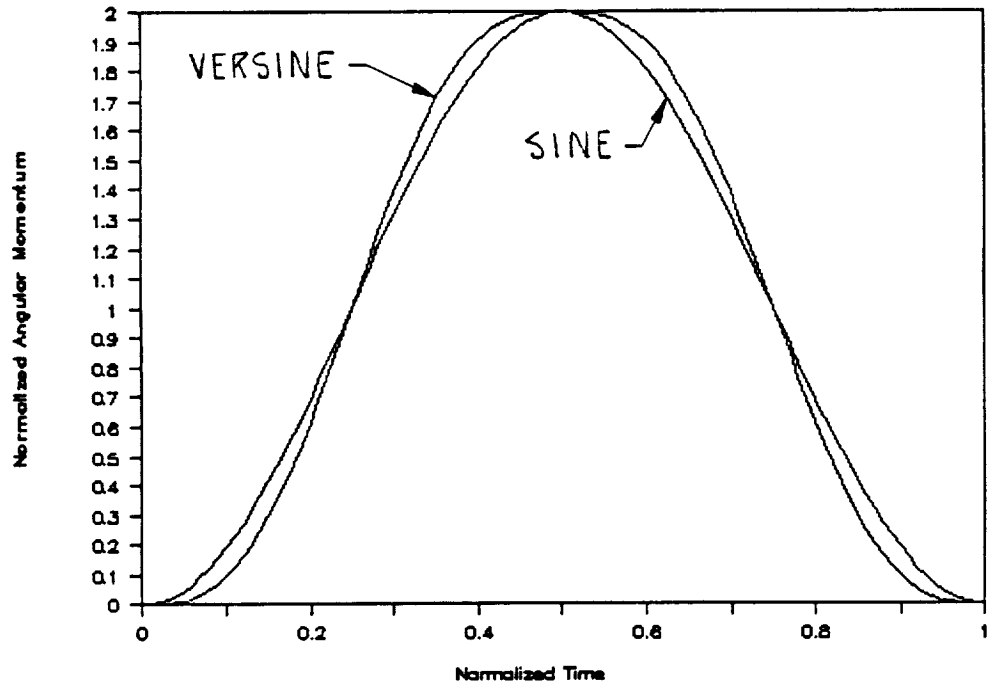

b) Angular Momentum

Figure 6. Normalized Trigonometric Command Shapes

ORIGINAL PAGE IS
OF POOR QUALITY

ORIGINAL PAGE IS
OF POOR QUALITY

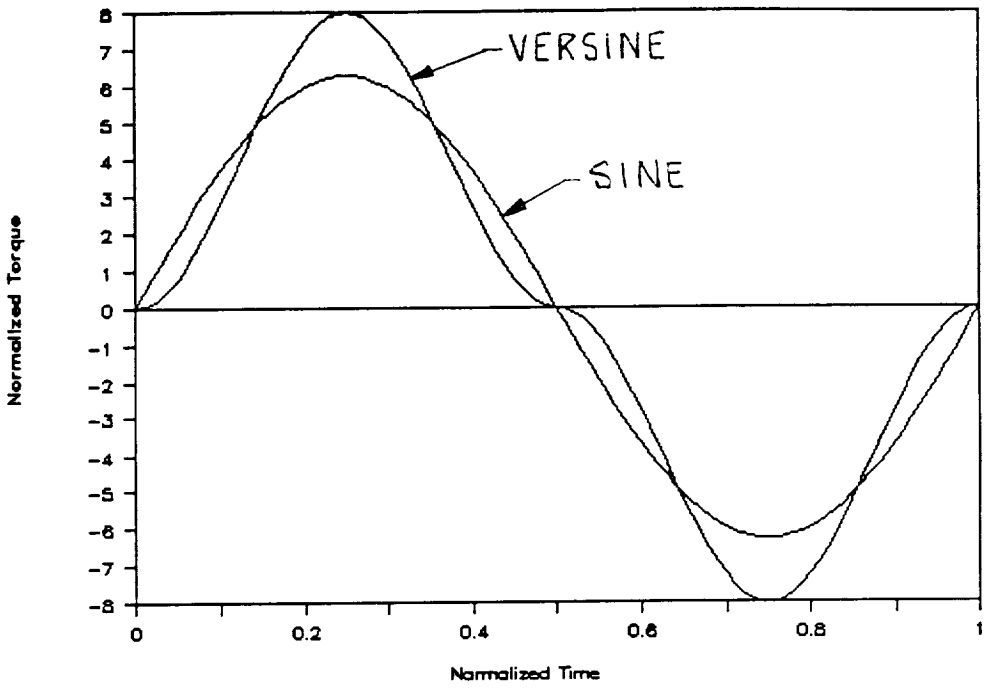

c) Torque

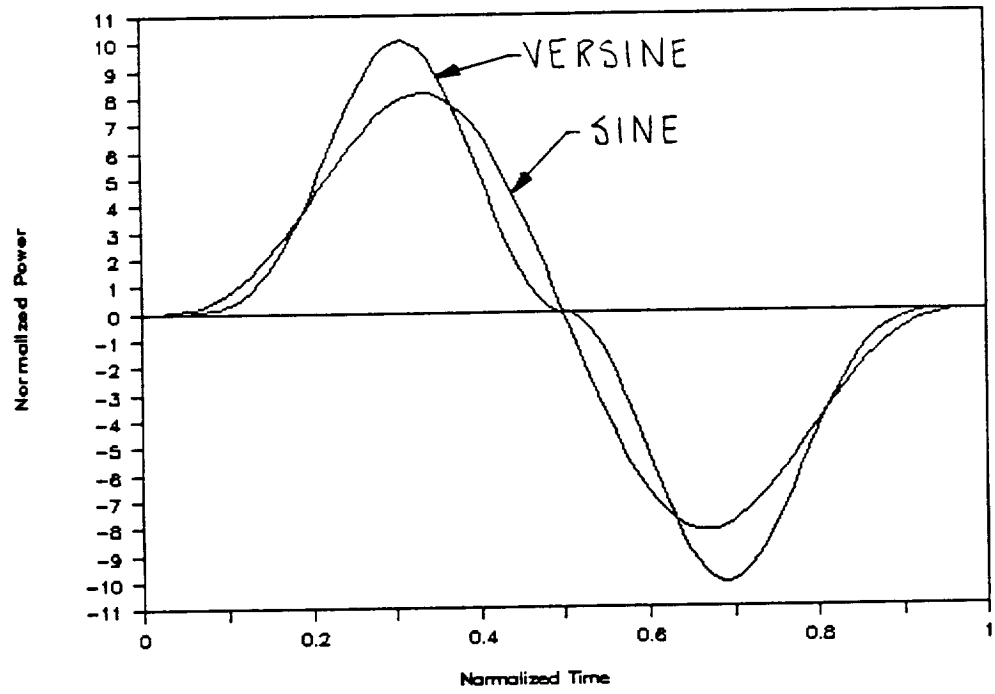

d) Mechanical Power

Figure 6. Normalized Trigonometric Command Shapes (Cont'd)

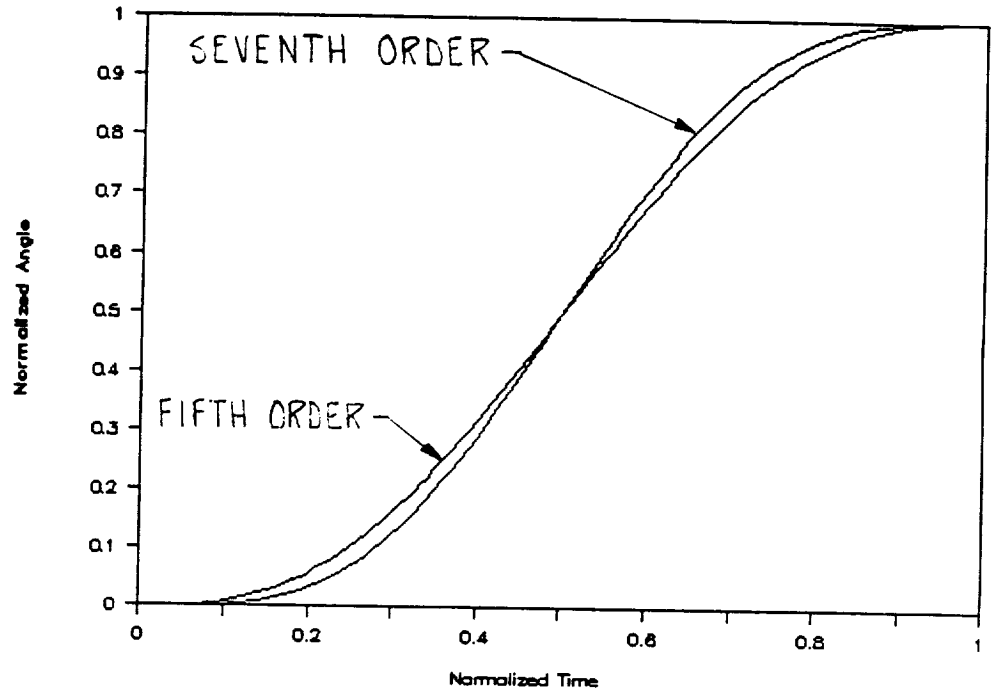

a) Angle

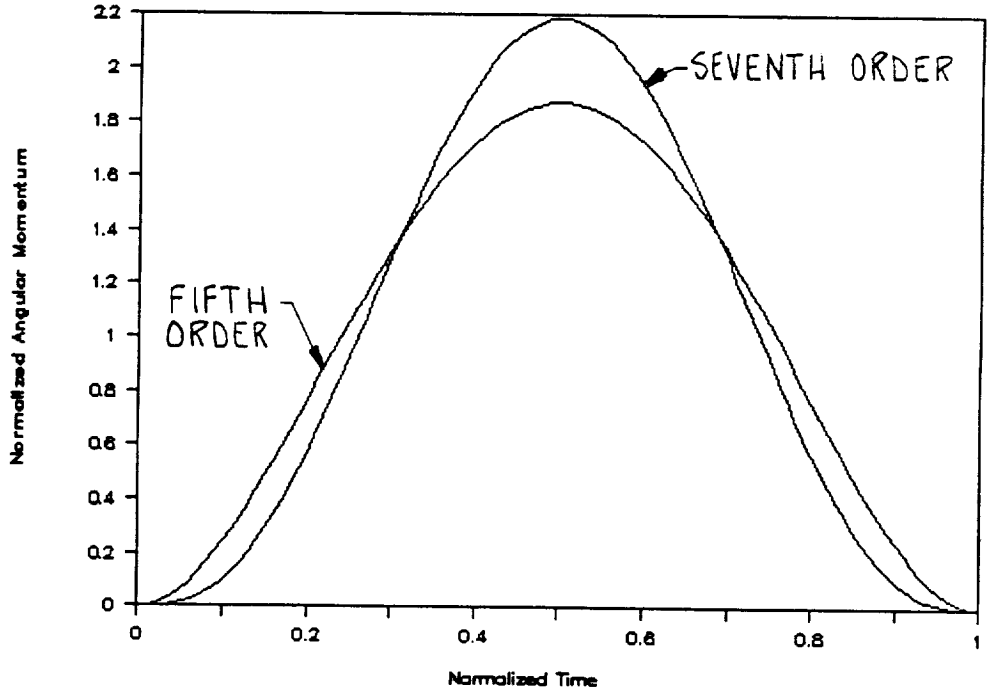

b) Angular Momentum

Figure 7. Normalized Polynomial Command Shapes

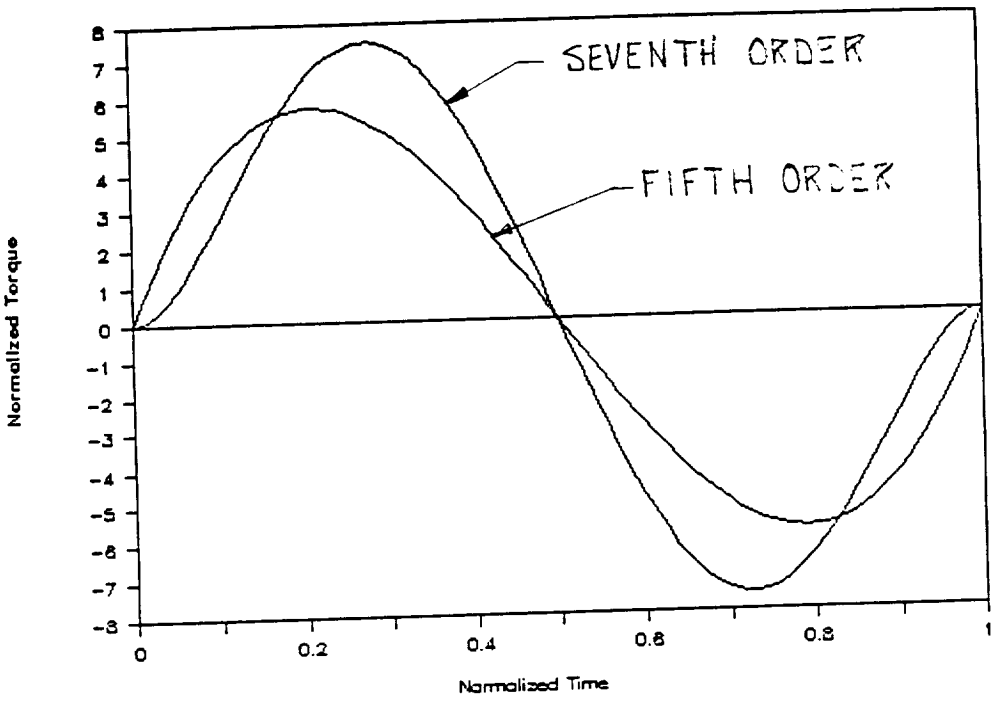

c) Torque

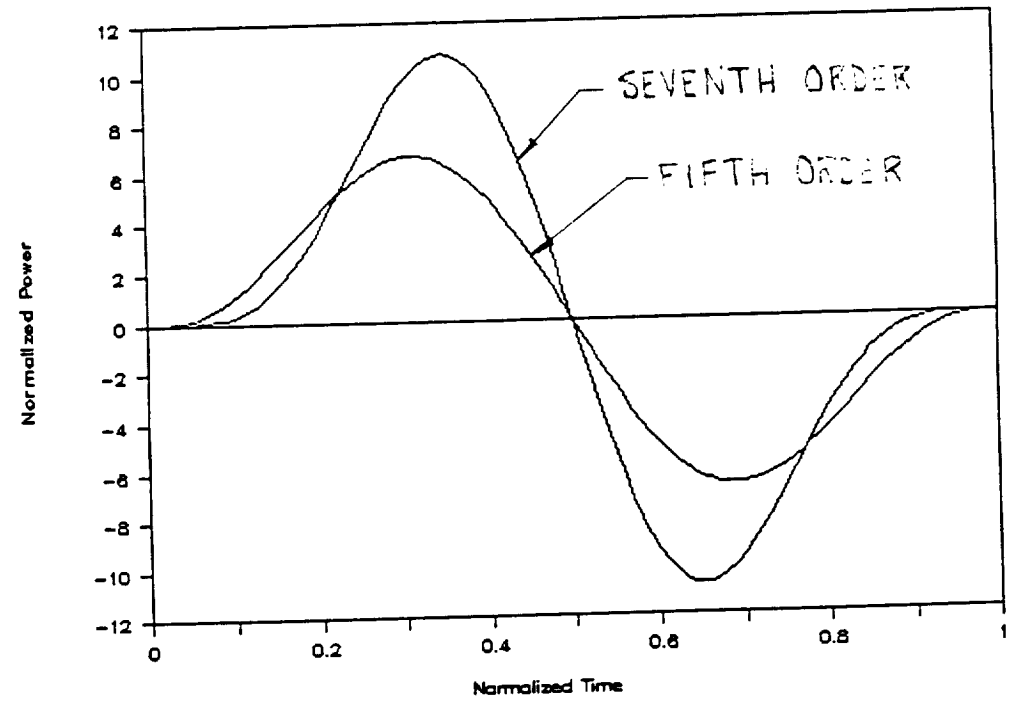

d) Mechanical Power

Figure 7. Normalized Polynomial Command Shapes (Cont'd)

2.3.4 Command Shape Parameters

Table IV presents the maximum normalized torque, angular momentum, and mechanical power for the various command shapes. Of these, the versine profile is the most demanding in terms of torque. This command shape was used to define a nominal set of slew trajectory parameters.

Table IV. Normalized Slew Requirements

	Torque	Momentum	Power
Discontinuous Shapes			
Bang-bang	4.000	2.000	8.000
Bang-rest-bang	4.500	1.500	6.750
Trigonometric Shapes			
Sine	6.283	2.000	8.162
Versine	8.000	2.000	10.085
Polynomial Shapes			
Fifth-order	5.770	1.875	6.694
Seventh-order	7.513	2.188	10.750

A set of slew trajectory parameters (angle and time) can be calculated from a torque requirement, an angular momentum storage capacity requirement, the normalized characteristics of a command shape, and a payload inertia.

$$T_s = \left(\frac{H_m}{H_n}\right) \cdot \left(\frac{\tau_{cn}}{\tau_{cm}}\right) \tag{2.3}$$

$$\theta_s = \left(\frac{H_m^2}{I_s \tau_{cm}}\right) \cdot \left(\frac{\tau_{cn}}{H_n^2}\right) \tag{2.4}$$

When the requirements from Reference 6 (50 kNm and 50 kNms) are combined with the normalized characteristics of the versine slew profile and the SAVI inertia (100 $kNms^2$), a baseline slew

trajectory of 1 radian in 4 seconds results. The peak mechanical power delivered to the payload is 15,760 Watts.

2.4 Finalized Actuator Specifications

Several modifications were made to the requirements defined in the preceding paragraph. First, a new type of command shape, missed in the preliminary survey, was discovered. Second, the torque specification of the actuator was reduced to be consistant with other efforts.

2.4.1 Pulsed Bang-bang Torque Profile

The pulsed bang-bang profile is the result of an effort to reduce the torque requirements of conventional command shaping techniques and still retain their primary advantage, not exciting flexible modes of the structure. The details of this torque shape are considered proprietary by Martin Marietta, but Gary Skidmore of Martin was willing to provide the required non-dimensional quantities for this study. Table V contains the non-dimensional parameters for this command shape.

Table V. Pulsed Bang-Bang Command Shape

	Minimum	Maximum
Torque	4.000	5.333
Angular Momentum	1.333	2.000
Power	6.750	8.000

Keeping the slew trajectory parameters which were calculated in Section 2.3.4, the use of the pulsed bang-bang torque profile

reduces the torque requirement to 33.3 kNm and the mechanical power handling capability to 12.5 kW. The angular momentum storage capacity remained unchanged at 50 kNms.

2.4.2 Consistancy With SAVI Program

Given that the baseline payload is that of the SAVI program, it was proposed at the mid-term program review to reduce the torque requirement to be consistant with this project. Since the difference was less than 20%, this change was not expected to modify the findings of the study. Given the reduced torque capacity, the slew time, angular momentum storage capacity, and mechanical power handling requirement were revised to the values listed in Table II.

3. CONFIGURATION ANALYSIS AND SELECTION

This chapter discusses the results of analyses which were directed toward identifying a promising angular momentum exchange type of slew actuator. Scissored pairs of advanced-technology control moment gyros were selected as the baseline configuration. The flywheels used in the array may also be used to provide the mechanical power required for the slew maneuver (a "constant-energy" array). The scissored-pair configuration is also particularly adaptable to the use of limited-angle "magnetic gimbals" as will be discussed in Chapter 5.

3.1 Angular Momentum Exchange Actuators

One approach for controlling the attitude of a spacecraft or other payload is to apply equal and opposite torques to the payload and a flywheel. The net angular momentum of the flywheel and the payload will remain constant. This type of device is referred to as an angular momentum exchange actuator since any angular momentum which is gained (lost) by the payload is lost (gained) by the flywheel. The use of momentum exchange actuators began in the early days of the space program [8] and has steadily progressed to a state of relative maturity [9].

Angular momentum may be exchanged between a flywheel and a payload in two ways. Either the spin rate (of a fixed orientation flywheel) or the orientation (of a fixed spin rate flywheel) may be varied. Each of these approaches is considered here.

3.1.1 Variable Spin Rate Actuators

Reaction and momentum wheels exchange angular momentum by varying the speed of a flywheel whose orientation is fixed with respect to the payload. Reaction wheels are designed to spin in either direction and are nominally non-spinning [9]. Momentum wheels vary spin in only one direction about a nominal, or bias, speed. Torque is applied to the payload through a motor.

Power transfer also accompanies torque delivery. The power (P) is the product of the control torque (τ) and the spin rate (ω) of the wheel relative to the payload

$$P = \tau\omega \tag{3.1}$$

Figure 8 shows the amount of power transfer which will accompany the delivery of the maximum control torque (27 kNm). The power level is several orders of magnitude higher than that which must be delivered to the payload. For this reason, variable spin rate actuators typically have very low torque capability. In addition, a reaction or momentum wheel provides only a single axis of torque capability.

3.1.2 Variable Orientation Actuators

A control moment gyro (CMG) exchanges angular momentum by varying the angular orientation of a constant-speed flywheel through the use of either a single- or a two-degree-of-freedom gimbal system [10]. Figure 9 describes this process in terms of applying a torque to a spacecraft over a fixed period of time. The torque is applied through a torquer mounted to the azimuth-

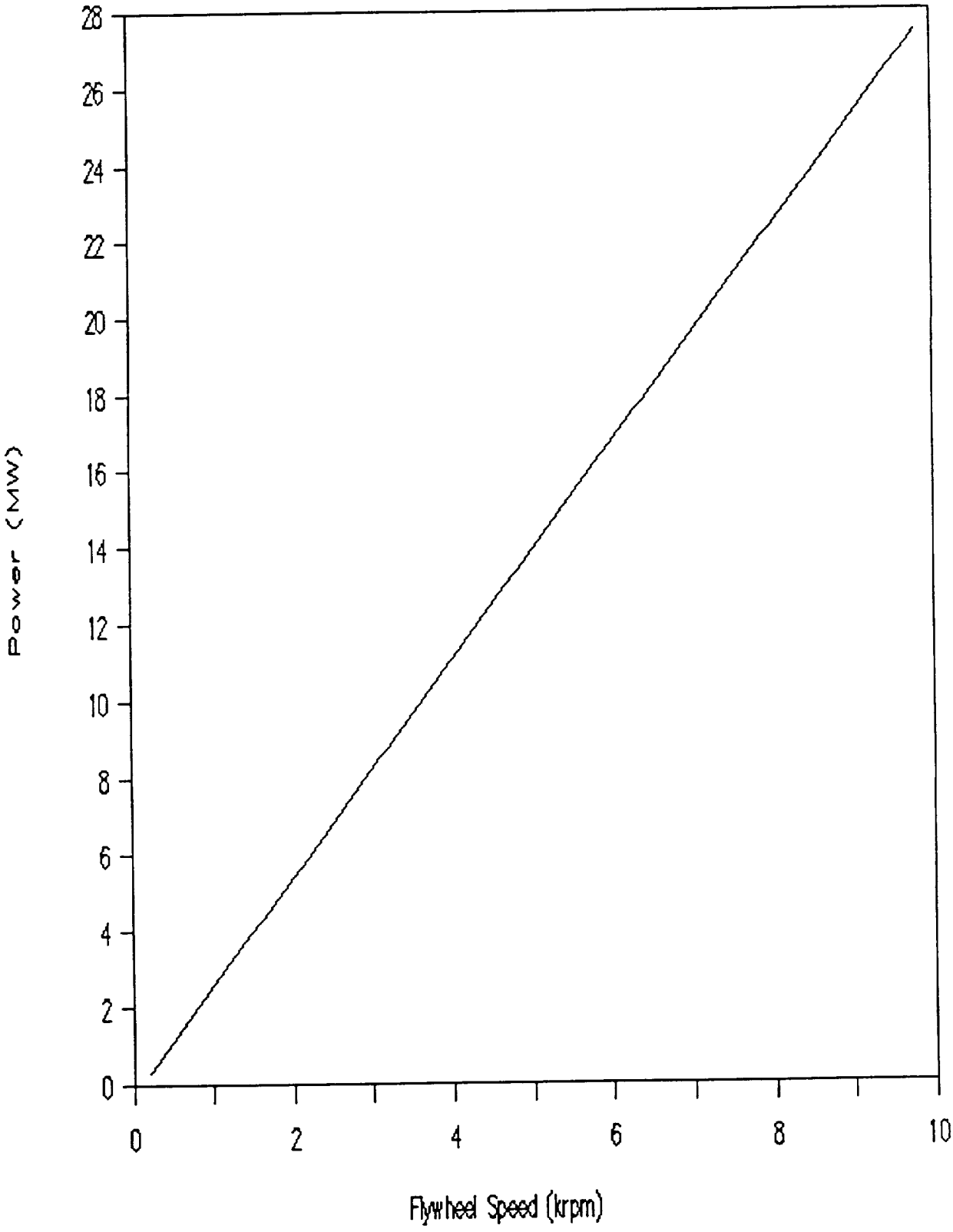

Figure 8. Reaction Wheel Power Transfer Requirement

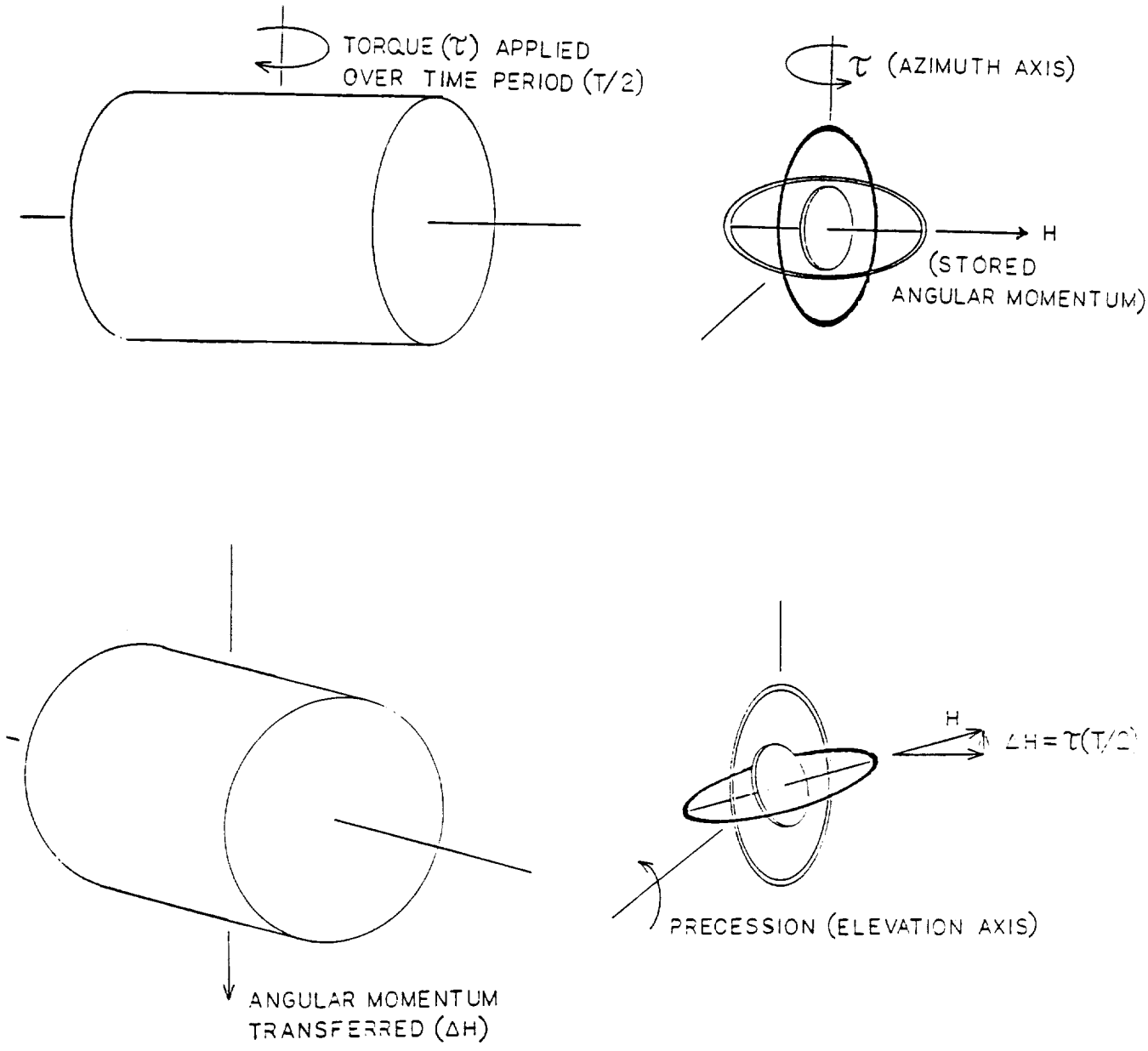

Figure 9. Operation of a CMG

axis gimbal. The flywheel precesses about the elevation axis to conserve the net angular momentum of the flywheel and the payload.

If a single CMG is to be used as a slew actuator, the amount of angular freedom of the gimbal system (the maximum gimbal angle, δ_{max}) must be at least equal to the maximum slew angle (θ_s).

Because of the disadvantages associated with reaction and momentum wheels and the two-degree-of-freedom actuation capabilities of CMGs, this study focused on CMG type actuator designs.

3.2 Conventional Technology CMGs

Table VI shows an attempt at employing several commercially available CMGs in the slew actuator application. The table shows the number of CMGs which would have to be used to provide for slewing in two axes. Double gimballed CMGs (DGCMGs) are typically limited by the capacity of the gimbal torquers, while the single-gimballed CMGs (SGCMGs) are limited by angular momentum storage capacity. The mass and power consumption of the CMGs were obtained from a manufacturers' data sheets [2].

Table VI. Conventional Technology CMGs

Model No.	Type	Torque (Nm)	Momentum (Nms)	Number Required	Mass (kg)	Power (W)
M4500	DGCMG	270	6,100	200	59,000	25,000
M2400	SGCMG	6,500	3,250	42	2,400	4,150

The number of units, mass, and power consumption are sufficiently large that commercially available approaches were eliminated from consideration.

3.3 Advanced-concept CMGs

In addition to parts count, the use of conventional-technology CMGs is limited by the mass and power consumption of these devices. This section discusses an alternative design approach which reduces the mass of double-gimballed CMGs. Further mass and power consumption reduction is discussed in the chapters which describe advanced component technologies.

One particularly large component of the mass of a double-gimballed CMG is that of the gimbal system. An early study of the power system for a space station concluded that the mass of the gimbal system of a CMG was typically as large as that of the rotor [11]. Later studies showed that, if a limited gimballing could be used (less than about 20 degrees), this mass penalty could be significantly reduced [5, 12].

3.3.1 Scissored-pair CMGs

An alternative to the use of a single CMG is a pair of counter-rotating CMGs. This is referred to as a scissored pair. Figure 10 shows this configuration schematically. The primary advantage of employing a scissored pair of CMGs in the slew actuator is that the requirement for a large-angle (at least equal to the maximum slew angle) is eliminated. This CMG

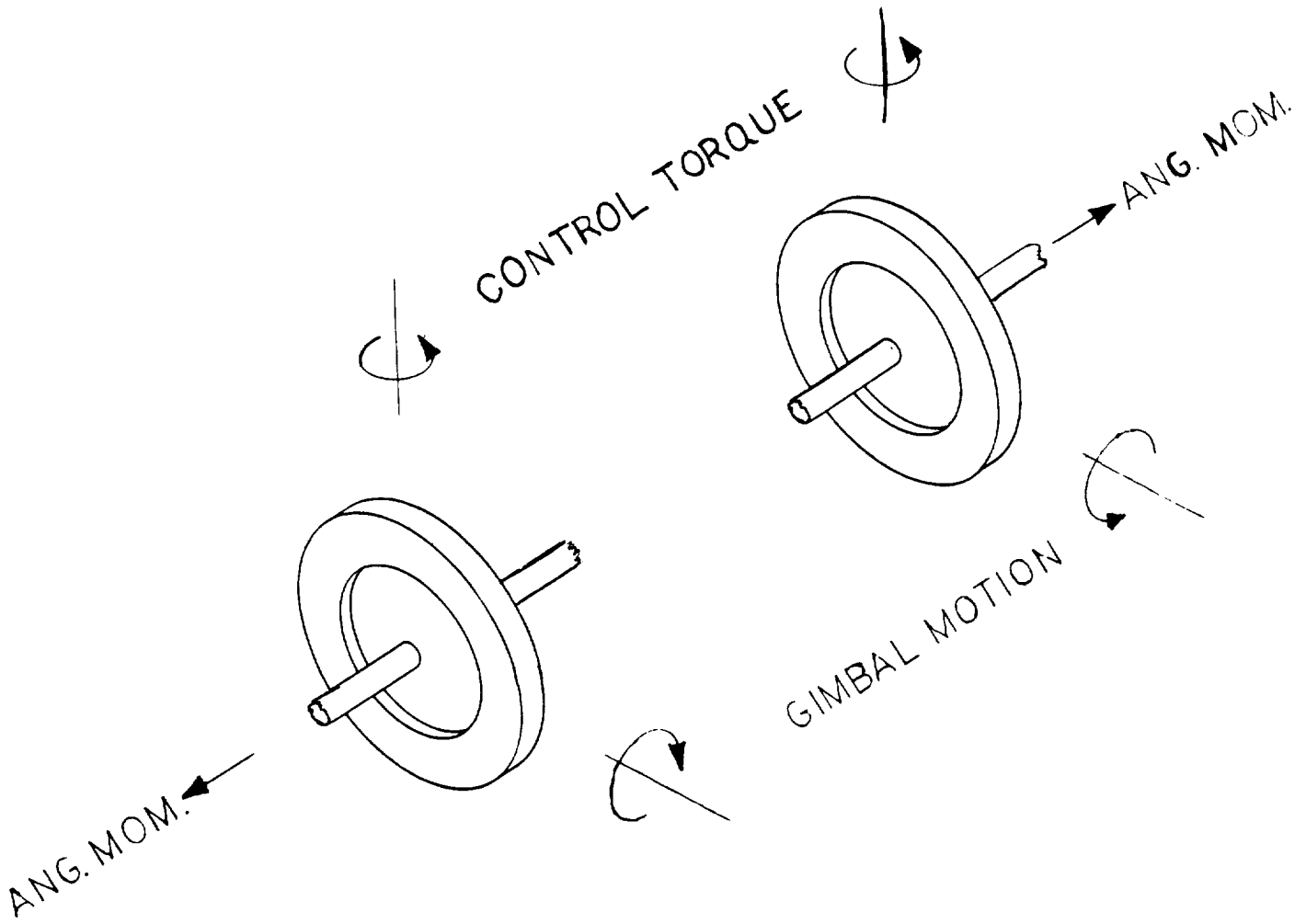

Figure 10. Scissored Pair of CMGs

configuration will be considered the baseline for the slew actuator.

3.3.2 Magnetic Gimballing

The technique which will be employed for reducing gimbal mass is to consolidate the functions of the gimbal and bearing systems [12]. Magnetic bearings are particularly adaptable to this task. When used in this capacity, the magnetic bearing is referred to as a large-angle magnetic suspension (LAMS) system. Conventional and advanced-concept designs for LAMS systems are presented in Chapters 5 and 6.

3.3.3 Angular Momentum Storage Requirement

The disadvantage to the use of a limited-angle gimbal system is that the angular momentum storage capacity of the flywheels increases. The angular momentum storage requirement (h_f) of each of the flywheels is a function of the angular momentum storage requirement of the slew maneuver and the maximum angular freedom.

$$2h_f \sin(\delta_{max}) = H_m \tag{3.2}$$

$$h_f = \frac{H_m}{2 \sin(\delta_{max})} \tag{3.3}$$

Figure 11 shows the angular momentum storage capacity of each flywheel as a function of the angular freedom of the gimbal system.

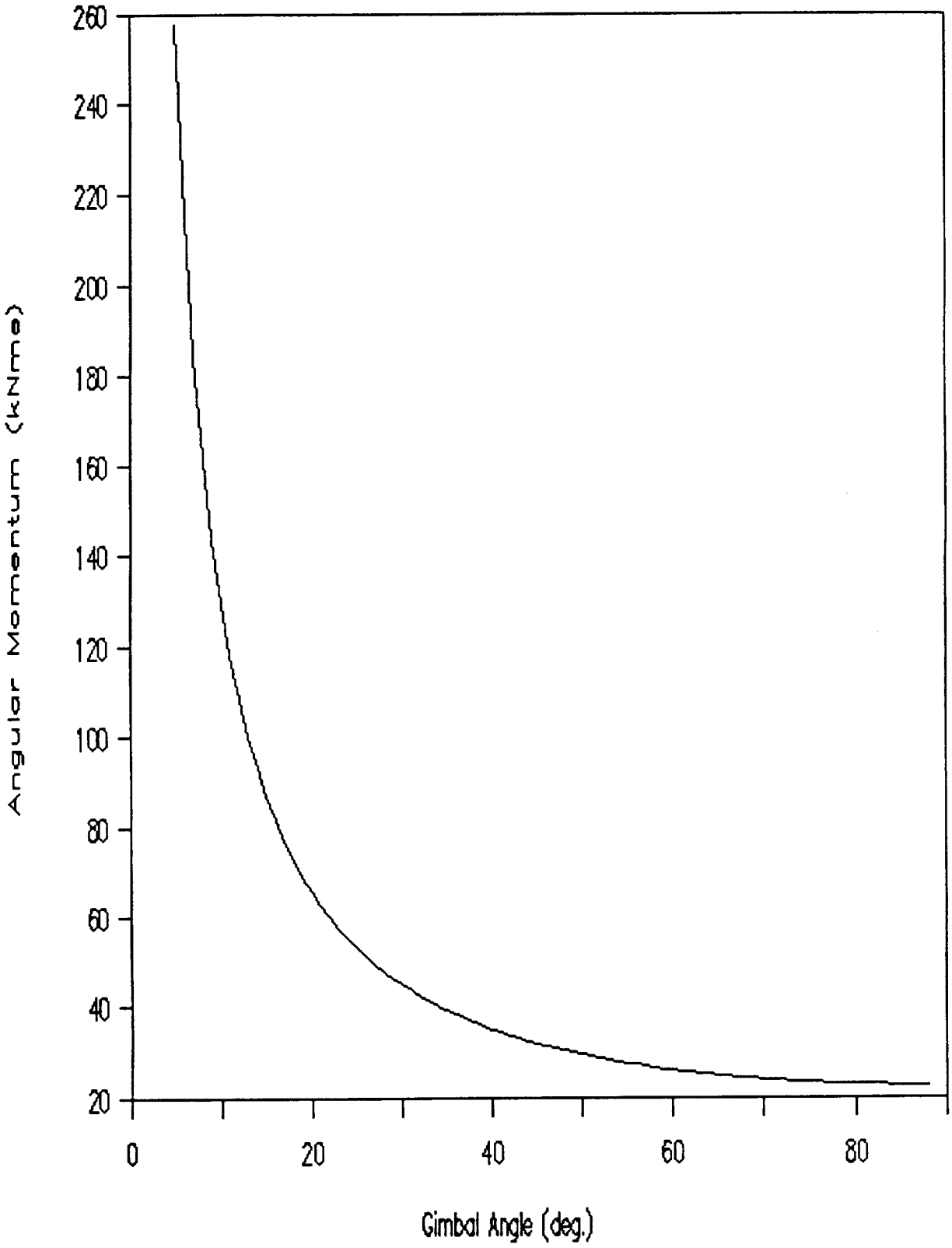

Figure 11. Angular Momentum Storage Capacity of a CMG

3.3.4 Precession Torque Requirement

Equal and opposite torques will be applied to each of the flywheels shown in Figure 10 in order that their spin axes follow the slew maneuver. These torques would be applied through a torque motor fixed on the elevation axis of the gimbal system. The magnitude of this precession torque (τ_p) is calculated from the angular momentum of the flywheel and the angular velocity of the payload.

$$\tau_p(t) = \Omega(t) \times h_f \qquad (3.4)$$

Section A.2 of Appendix A derives an expression for the maximum precession torque (τ_{pm}) required during a slew maneuver. Again, a bang-bang command shape is assumed. The maximum precession torque is given below as a function of the maximum control torque (τ_{cm}), the slew angle (θ_s), and the maximum gimbal angle.

$$\frac{\tau_{pm}}{\tau_{cm}} = \frac{\theta_s}{2 \sin^2(\delta_{max})} \qquad (3.5)$$

Figure 12(a) shows the maximum precession torque relative to the maximum control torque for the baseline slew maneuver. Note that for maximum gimbal angles less than 45 degrees, the gimbal torquers are sized by the precession rather than control torque. Figure 12(b) presents the maximum precession torque for the slew actuator for relatively large, but limited, gimbal angles. A gimbal system with 60 degrees of angular freedom requires a precession torque which is two thirds of the control torque.

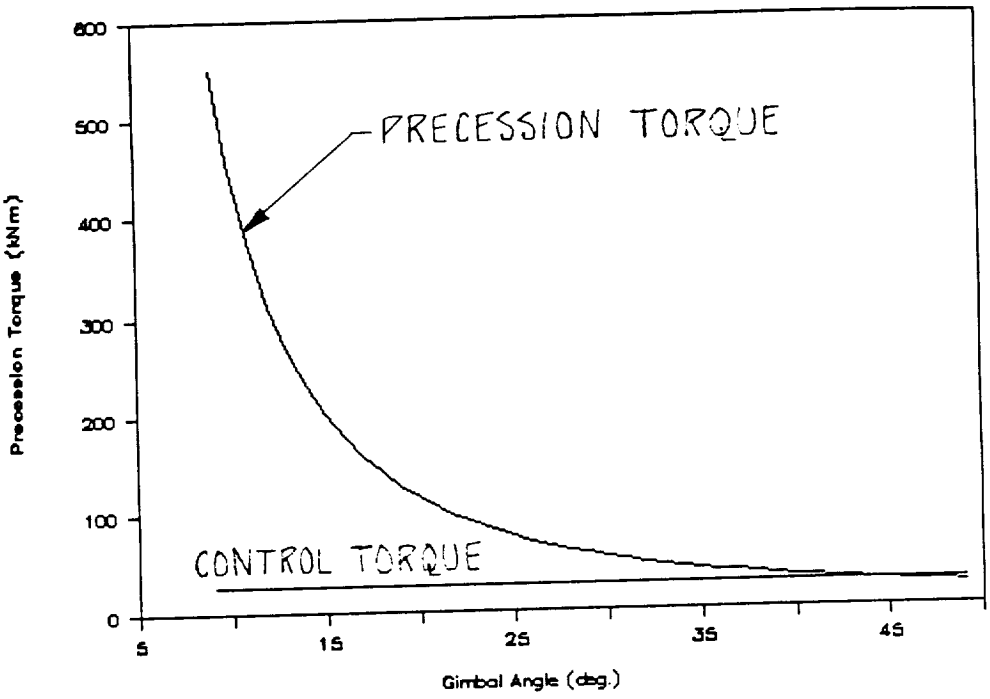

a) Small Gimbal Angles

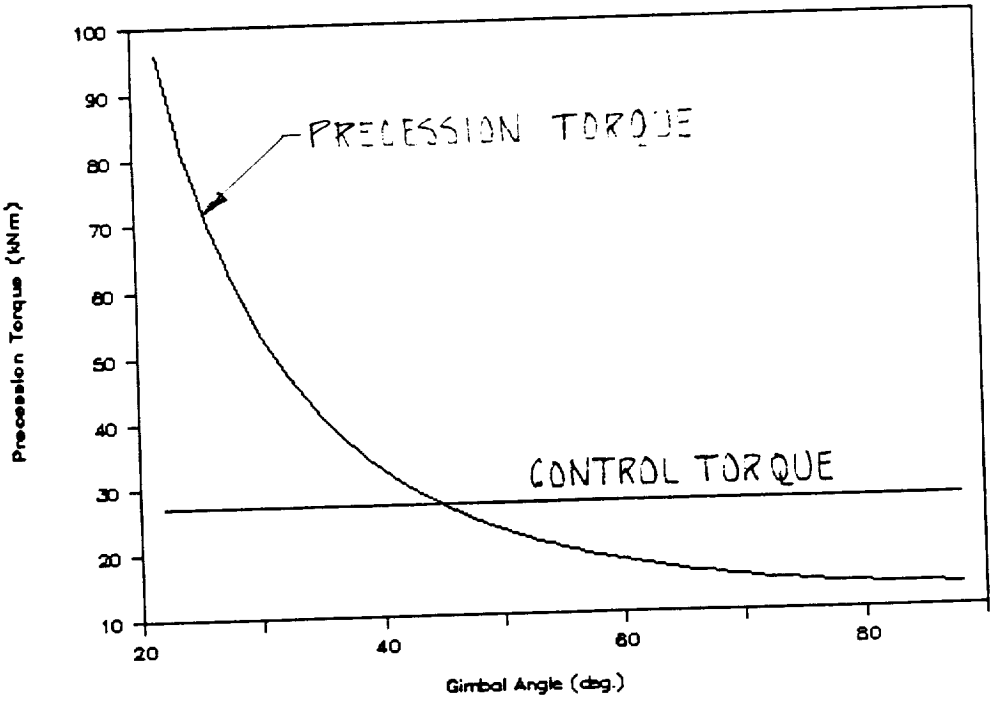

b) Larger Gimbal Angles

Figure 12. Normalized Maximum Precession Torque

3.3.5 Angular Freedom Selection

Figures 11 and 12 show that, although full gimballing is not required, angular freedom in the range of 30 to 60 degrees has advantages. Increased angular freedom decreases the amount of angular momentum which must be stored in the flywheels. An even more pronounced effect is seen for the precession torque requirement. This latter quantity is inversely proportional to the square of the sine of the angular freedom of the gimbal system.

3.4 Energy Management

A significant amount of mechanical power is delivered to the payload during the acceleration phase of the slew maneuver. The total energy which results is stored as rotational kinetic energy in the payload. This energy could be recovered during the deceleration phase.

3.4.1 Power Supply Considerations for Slewing

This section considers the rotational kinetic energy and angular momentum of the payload. The idea of a "constant-energy array" is that the energy associated with the spin-axis angular momentum of the flywheel (or flywheels) of the slew actuator may be transferred to the payload during acceleration and returned during deceleration. The kinetic energy (e_f) and angular momentum (h_f) stored in a flywheel are related to the moment of inertia (I_f) and rotational speed (ω_f) of the flywheel.

$$e_f = \frac{1}{2} I_f \cdot \omega_f^2 \tag{3.6}$$

$$h_f = I_f \cdot \omega_f \tag{3.7}$$

$$e_f = \frac{1}{2} h_f \cdot \omega_f \tag{3.8}$$

Figure 13 shows the amount of kinetic energy associated with the storage of 45 kNms of angular momentum as a function of rotational speed.

The amount of energy which must be transferred to the payload during the slew maneuver is the maximum kinetic energy (E_m) of the inertia of the payload. This quantity is related to the maximum angular momentum of the payload as follows.

$$E_m = \frac{H_m^2}{2I_s} = (P_m T_s) \frac{H_m^2}{2P_n} \tag{3.9}$$

For the baseline slew parameters, the required energy for the maneuver ranges between 4.6 and 12.4 kJ depending on the type of command shaping that is used. The average is 9.3 kJ (2.6 Wh), which is small in comparison to the energy stored in the flywheels.

When considered in terms of the amount of mechanical power (9,100 W) and energy (9,300 J) which must be transferred, a slew maneuver can easily be thought of as a small-scale pulsed power application. The typical approach for delivering power in pulses is to provide energy storage so that the prime power source

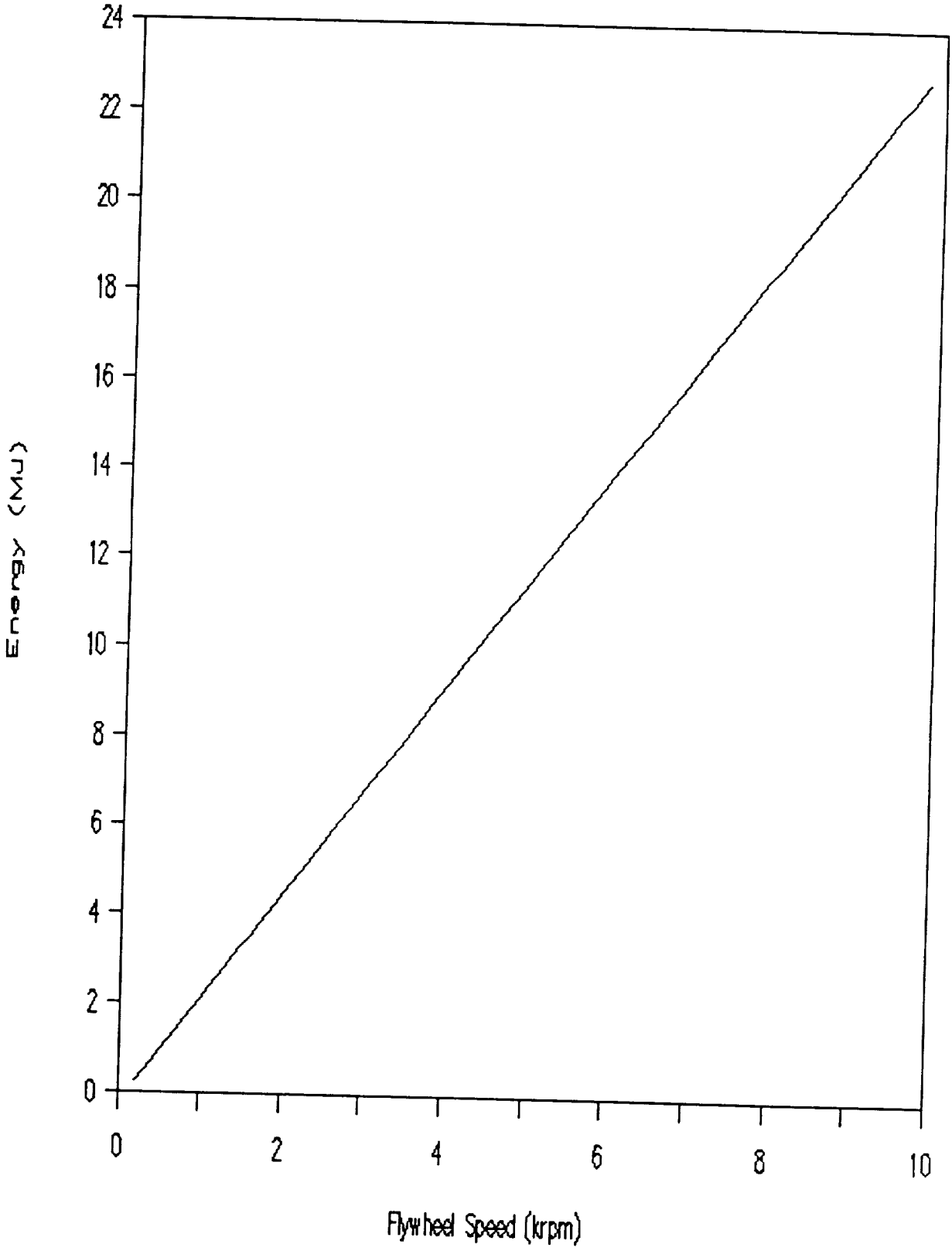

Figure 13. Kinetic Energy Stored in the Slew Actuator

(particularly on a spacecraft) may be sized for the average, rather than the peak, power handling requirement. The large amount of energy stored in the slew actuator, suggests that it be used to "load level" the power demand of the slewing maneuver.

3.4.2 Performance of a Constant Energy Array

Section A.3 of Appendix A models the slew actuator as an imperfect power conversion device with a constant conversion efficiency (η_C). The purpose of the analysis is to assess the value of energy storage for the slew maneuver. Figures 14(a) and 14(b) show two models for the slew actuator, one with and one without energy storage capability.

Without energy storage, the prime power supply will have to source and sink a peak power (P_{pk}) which is the sum of maximum power requirement for the maneuver (P_m) and the peak power dissipated in the actuator.

$$P_{pk} = \frac{P_m}{\eta_C} \tag{3.10}$$

The average power (P_{avg}) transferred by the prime power source to the actuator is much lower. The following equation relates the average power to the peak mechanical power requirement for the bang-bang command shape.

$$P_{avg} = P_m \frac{1 + \eta_C^2}{4\eta_C} \tag{3.11}$$

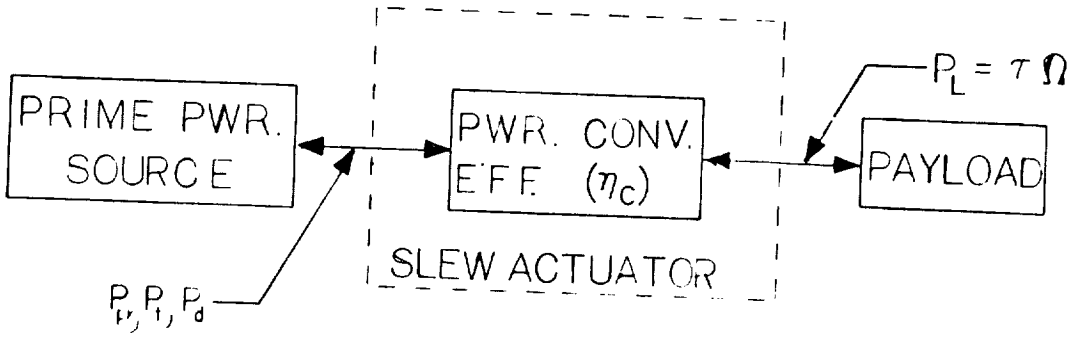

a) No Energy Storage

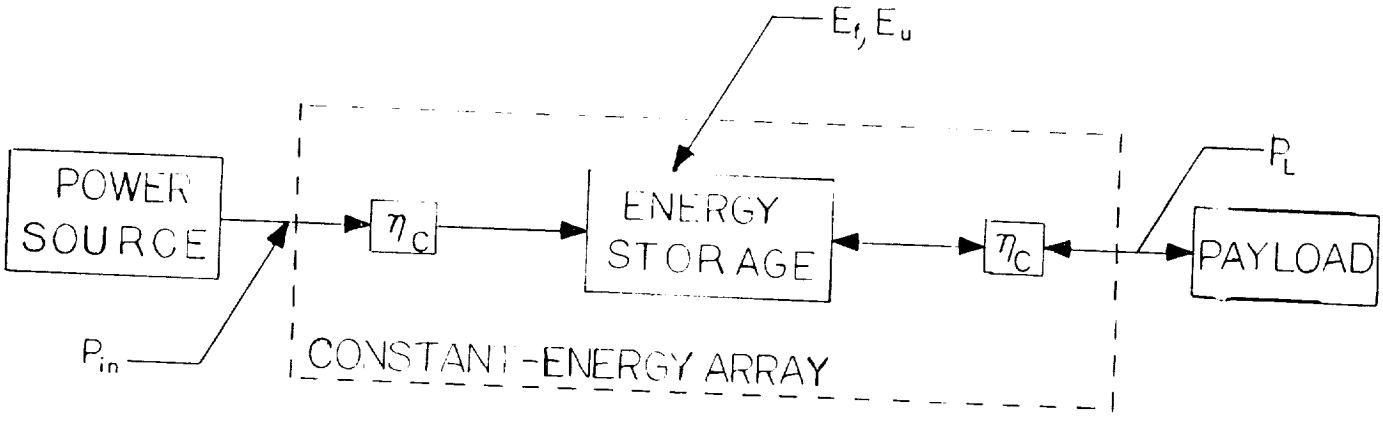

b) With Energy Storage

Figure 14. Models for the Slew Actuator

The peak and average power requirements from the prime source are shown in Figures 15(a) and 15(b) as a function of the efficiency of the slew actuator. The average power is always less than the peak power for a given conversion efficiency. For conversion efficiency greater than 27%, the average power is less than the peak power for a perfect ($\eta_C = 1$) actuator.

The continuous power input for a slew actuator with energy storage is also derived in the appendix under the assumption of bang-bang command shape. The continuous power input (P_C) is related to the peak mechanical power requirement as follows.

$$P_C = P_m \frac{1 - \eta_C^2}{4\ \eta_C^2}$$

$$= P_{pk} \frac{1 - \eta_C^2}{4\eta_C} \qquad (3.12)$$

$$= P_{avg} \frac{1 - \eta_C^2}{\eta_C\ (1 + \eta_C^2)}$$

Figures 16(a), 16(b), and 16(c) show the continuous power input for the constant energy array as a function of conversion efficiency and compare this to the power supply requirements for a slew actuator without energy storage. The continuous power input for a slew actuator with energy storage will be less than the peak power requirement for a slew actuator without energy storage if the conversion efficiency is greater than about 24%. If the conversion efficiency is greater than 45%, the continuous

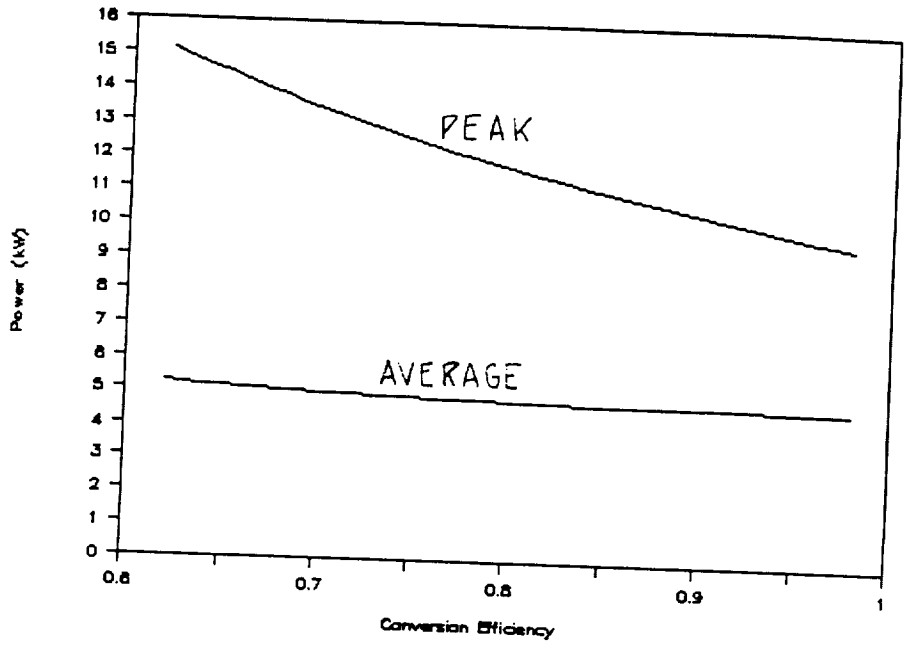

a) Average and Peak Power

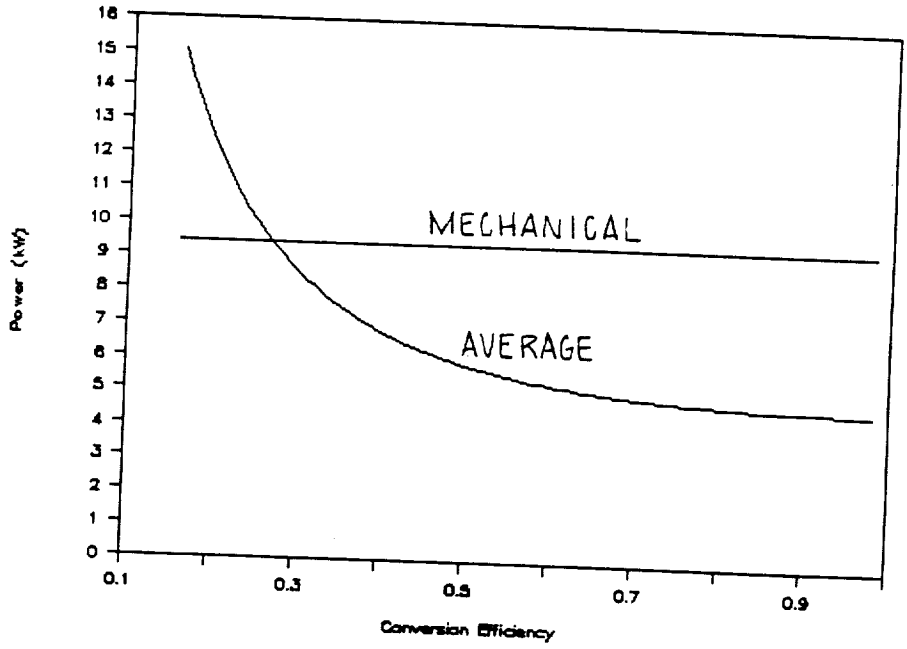

b) Average and Mechanical Power

Figure 15. Power Supply Requirements for a Slew Actuator

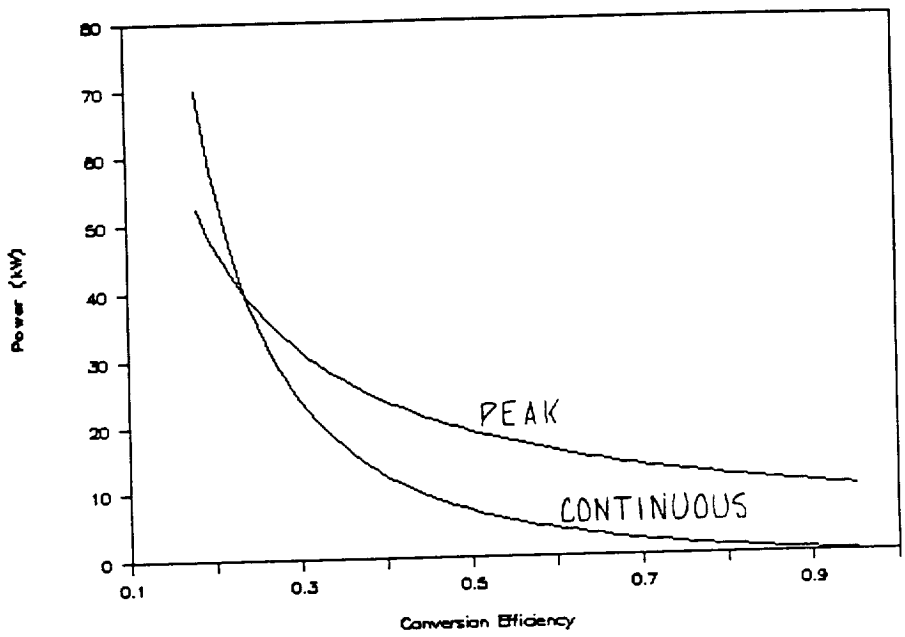

a) Continuous and Peak Power

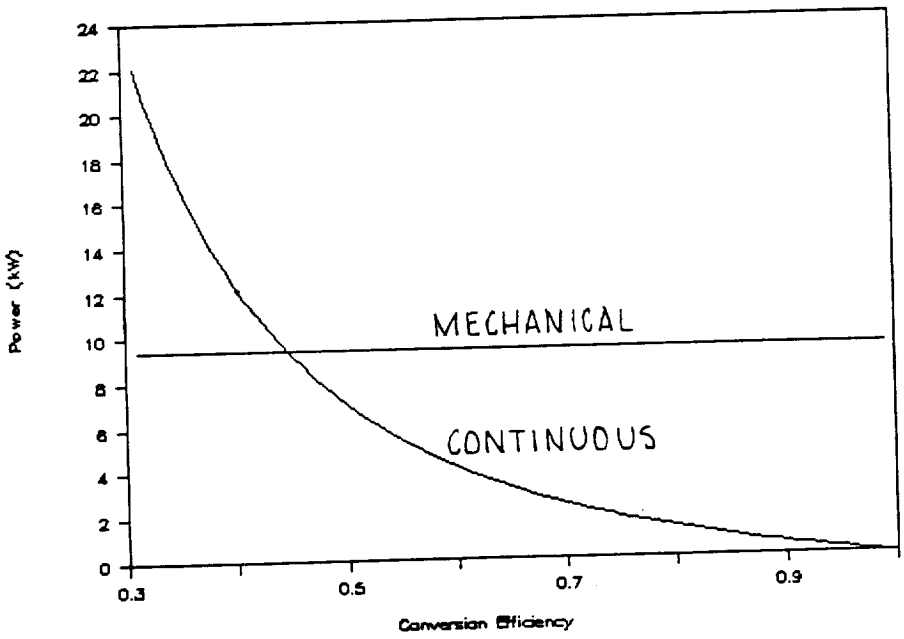

b) Continuous and Mechanical Power

Figure 16. Power Requirement for a Constant Energy Array

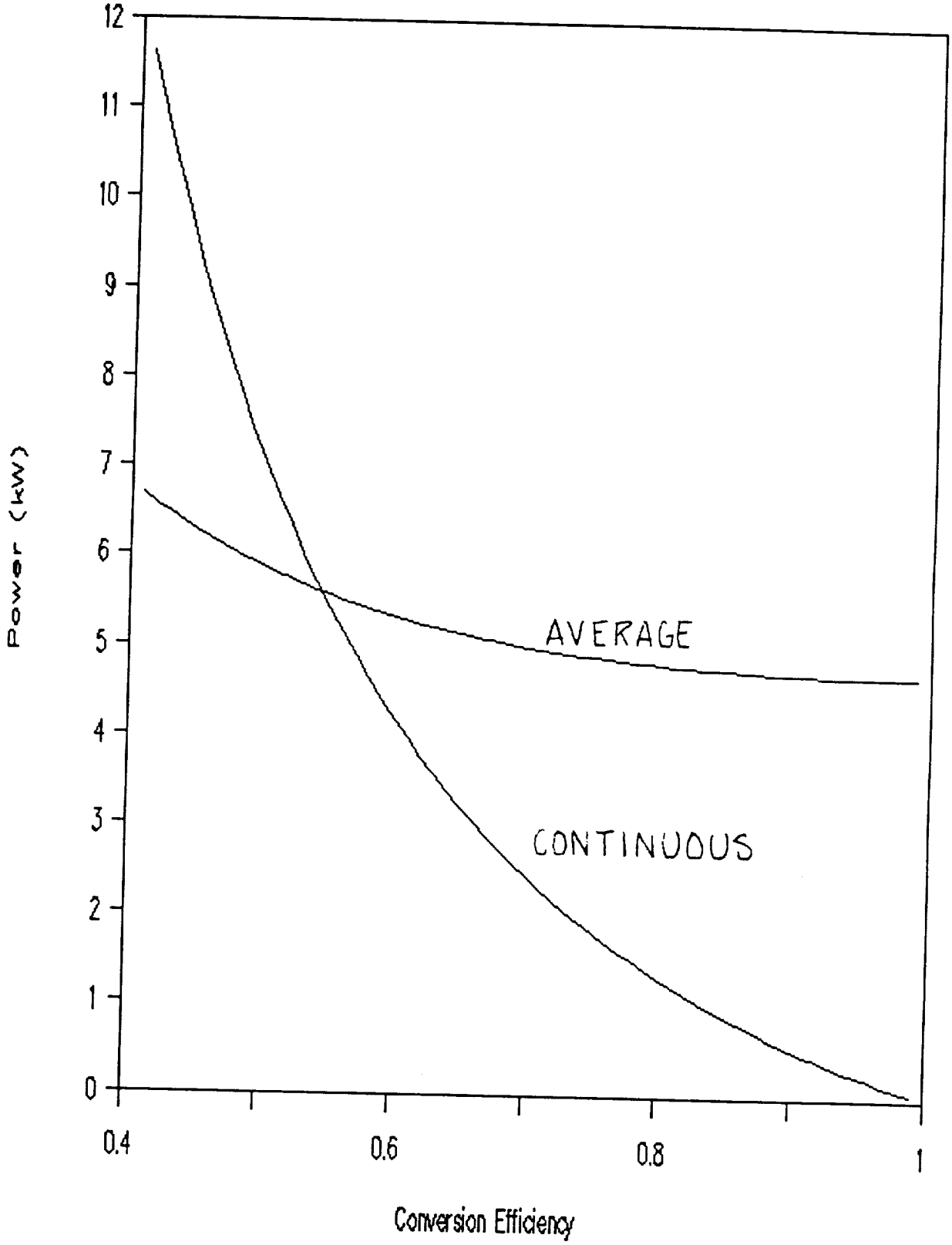

c) Continuous and Average Power

Figure 16. Power Requirement for a Constant Energy Array (Cont'd)

power input will be less than the mechanical power requirement. A realistic goal for the efficiency of the slew actuator is to reduce the continuous power requirement to the average power requirement. This can be achieved if the conversion efficiency is greater than about 54%.

The useful energy storage capacity (E_u) required to accomplish the slew maneuver is also determined in Appendix A for the bang-bang command shape.

$$E_u = (P_m T_s) \frac{1 + \eta_c^2}{8\eta_c} = E_m \frac{1 + \eta_c^2}{2\eta_c} \tag{3.13}$$

The fraction of the total energy storage capacity (E_s) which is useful is typically referred to as the depth of discharge (η_{dod}). The required total energy storage capacity is then specified as a function of the mechanical energy requirement, the actuator efficiency, and the depth of discharge.

$$E_u = \eta_{dod} \cdot E_s \tag{3.14}$$

$$E_s = \frac{E_u}{\eta_{dod}} = E_m \frac{1 + \eta_c^2}{2\eta_c \eta_{dod}} \tag{3.15}$$

Figures 17(a) and 17(b) show the useful and total energy storage capacities. The useful capacity is shown as a function of conversion efficiency, while the total capacity is shown as a function of conversion efficiency and depth of discharge. Even for relatively low efficiency and depth of discharge, the total energy stored in the flywheels of the slew actuator (Figure 13)

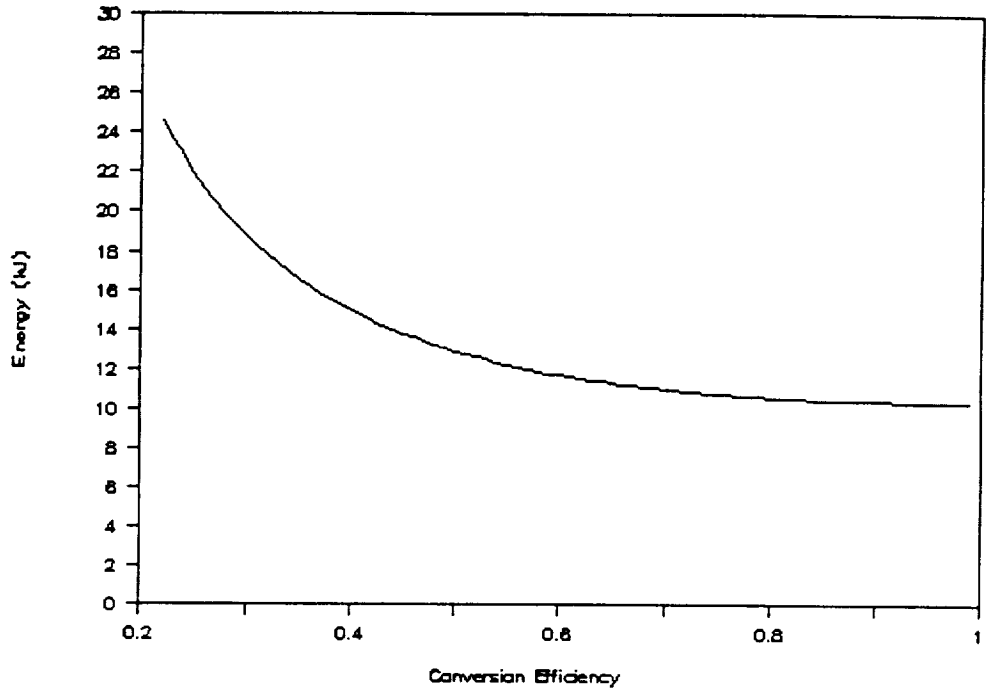

a) Useful

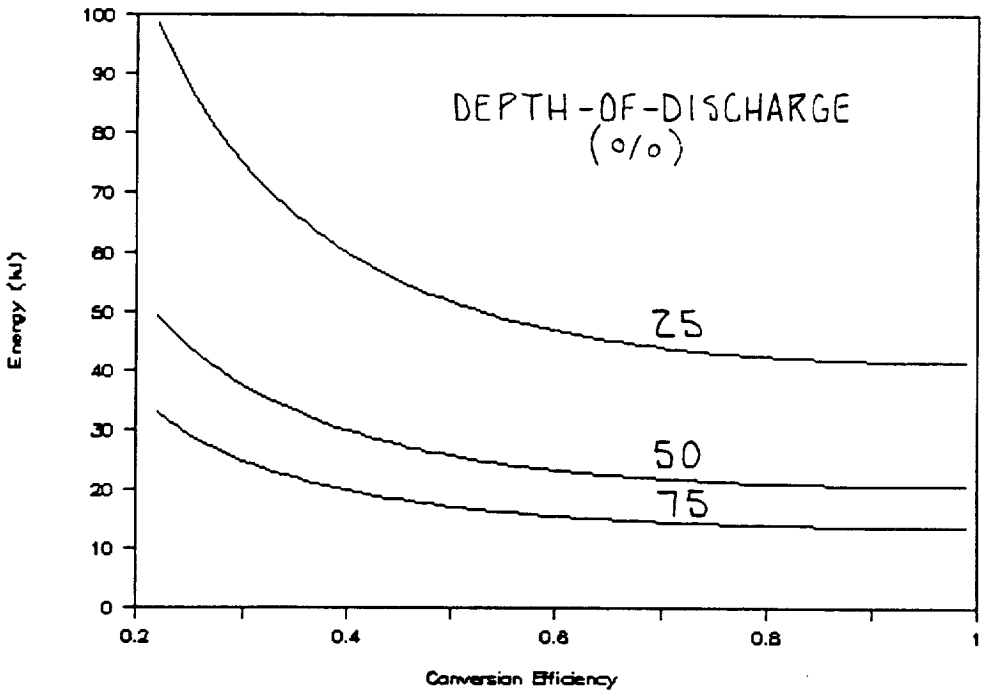

b) Total

Figure 17. Energy Storage Requirements for a Constant Energy Array

is large in comparison to the requirements for the slew maneuver. This implies that a relatively conservative (low) depth of discharge may be used.

The constant energy array is particularly useful when the actuators are configured as scissored pairs of CMGs since the changes in angular momentum as the flywheels are decelerated and then accelerated will cancel.

3.5 Configuration Summary

Based on the results presented in this chapter, a baseline configuration for the slew actuator was established. Two scissored pairs of magnetically double-gimballed CMGs will be used to provide torques and angular momentum storage for the three axes of the payload. The kinetic energy stored in the angular momentum of one of the pairs of CMGs is delivered to the other pair of CMGs to meet the mechanical energy needs of the slew maneuver. Power from a prime source is used to replace the energy lost to dissipative mechanisms.

4. COMPOSITE FLYWHEEL ASSESSMENT

This chapter discusses the use of advanced composite-material flywheels in the slew actuator. Based on recent research in this field, alternative materials are considered and a baseline (high-strength graphite fibers in an epoxy matrix) is selected. The results of sizing studies for the flywheel of the slew actuator are presented. A stress analysis of a composite flywheel rotor is presented in Appendix B.

4.1 Approach

The approach to determining the baseline rotor material was to evaluate a fundamental shape (the annulus which is shown in Figure 18), and apply these results to achieve realistic rotor designs. The "best" flywheel design is that which stores the greatest angular momentum per unit of mass (momentum density, ρ_h). Flywheels, however, are more typically employed to store energy, and are therefore described by the amount of stored kinetic energy per unit of mass (energy density, ρ_e). The two quantities are related by the maximum angular velocity of the flywheel (ω).

$$\rho_h = \frac{2\rho_e}{\omega} \tag{4.1}$$

A high angular momentum flywheel design is, therefore, one which possesses a high energy density and which is designed to operate at a low speed. Figure 19 shows the angular momentum density of

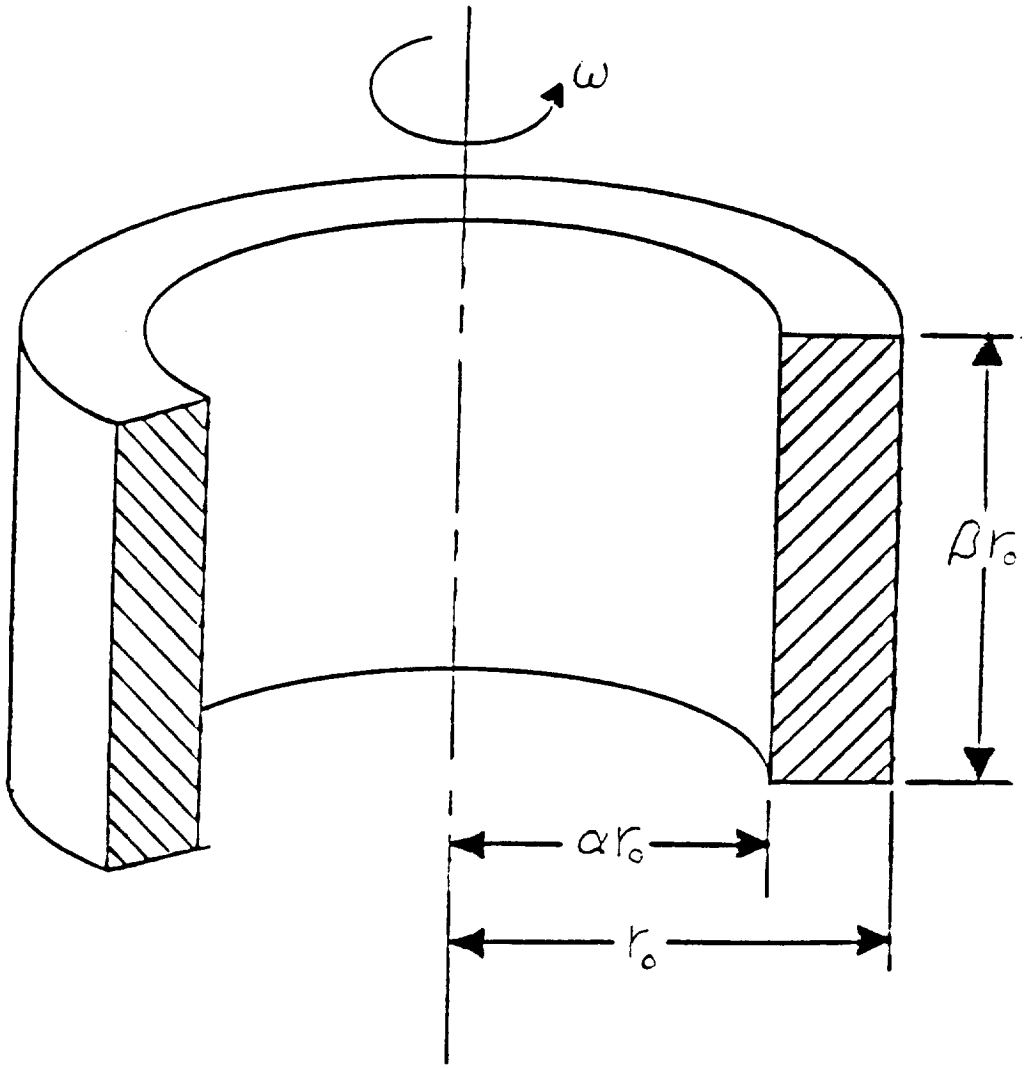

Figure 18. Annular Flywheel

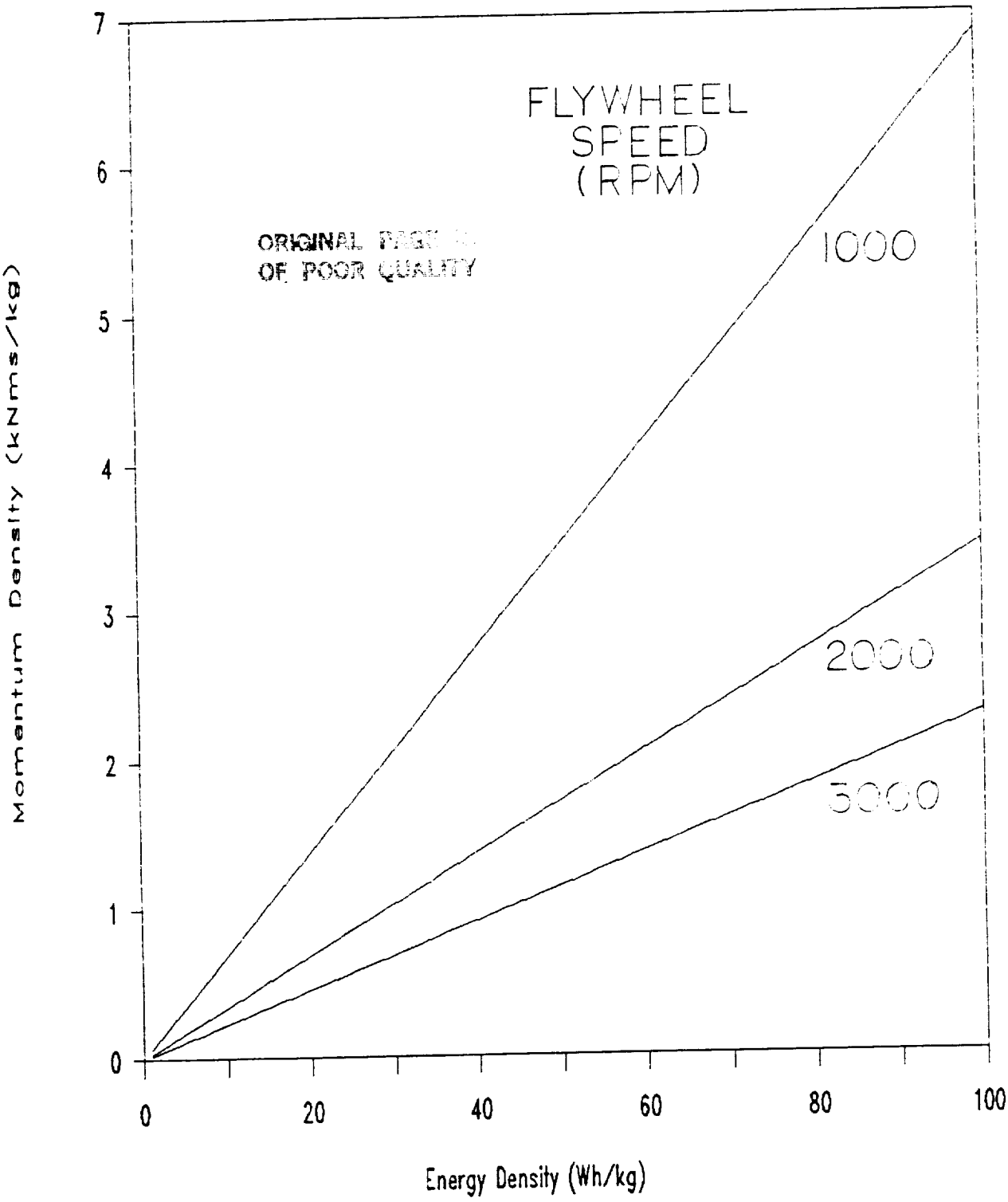

ORIGINAL PAGE IS
OF POOR QUALITY

Figure 19. Momentum Density for Flywheels

flywheels as a function of the energy density and rotational speed of the flywheel.

4.2 Background

Over the last ten years, the government has funded the design and development of a large number of composite flywheel rotors [13, 14]. This research, which received early support from NSF, has recently been funded almost exclusively by DOE and its predecessor, ERDA. This program has resulted in the development and test of ten composite rotor systems [15]. This research was directed toward the development of fixed-base (utility) and moving-base (vehicle) applications on Earth.

In addition, NASA has funded workshops [16, 17] and research [12] concerning the use of flywheels in space-based applications. The results of this later research, summarized in Reference 16, show that a number of promising composite systems exist that DOE ruled out for consideration based on either high cost or unavailability. These systems include metal matrices, such as boron/aluminum or silicon carbide/aluminum, and more conventional composites, such as boron/epoxy. The most recent study of space-based flywheel energy storage systems [12] recommended four flywheel materials for further consideration. These materials are listed in Table VII.

Recently, significant new research was conducted at Oak Ridge National Laboratory [18]. A small flywheel rim was constructed of carbon composites and dynamically tested in a spin

Table VII. Composite Flywheel Materials

GRAPHITE/EPOXY (Gr/Ep)
BORON/EPOXY (B/Ep)
BORON/ALUMINUM (B/Al)
SILICON-CARBIDE/ALUMINUM (SiC/Al)

test chamber at the Oak Ridge Gaseous Diffusion Plant. The configuration of the unit is shown in Figure 20. The design of this unit is similar to the planned construction for the outer portion for larger flywheel rims. The success of this early demonstration unit provides a confirmation of the ability to fabricate, assemble, and test thick-walled composite sections. Both the specific energy (89 Wh/kg) and the total energy (7.687 MJ) of the flywheel tested exceeds any reported performance from the DOE flywheel development program. The fact that the specific energy of 500 kJ/kg is an operational rather than an ultimate (at failure) value is especially impressive.

Since this early test, a number of additional rims have been fabricated and tested. The characteristics of these test rims are given in Table VIII while the test results for these rims are given in Table IX. Each of these flywheels has the diameters and composition shown in Figure 20. Figure 21 shows the performance of these flywheels represents in comparison to previous rotors.

Table VIII. Characteristics of Test Rims

DEMO UNIT	AXIAL LENGTH mm (in)	RADIAL THICKNESS mm (in)	RIM MASS (kg)
1A	101.6 (4.0)	38 (1.5)	12.5
1B	48.3 (1.9)	38 (1.5)	5.8
1C	48.3 (1.9)	38 (1.5)	5.8

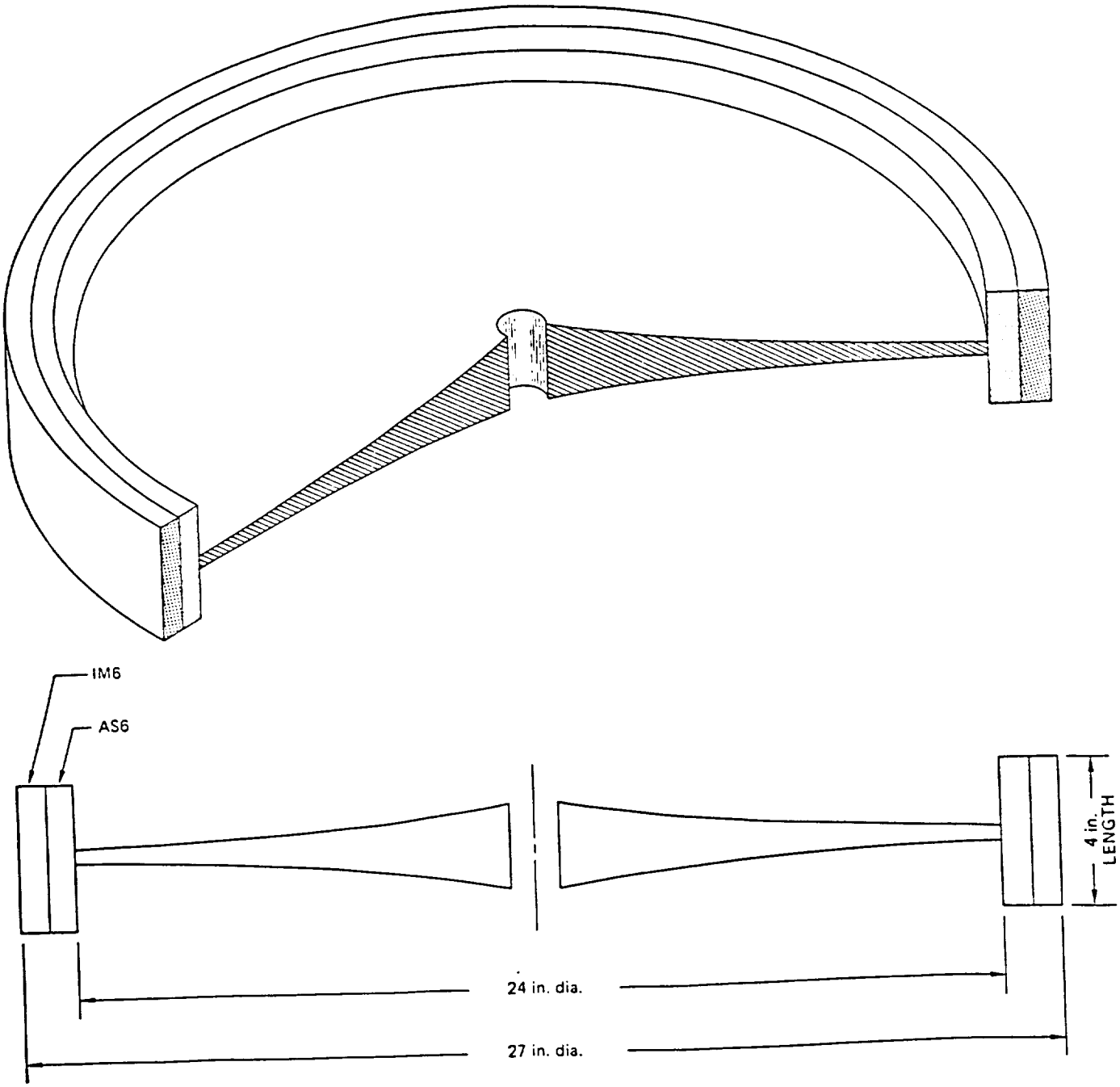

Figure 20. Flywheel Energy Storage Demonstration

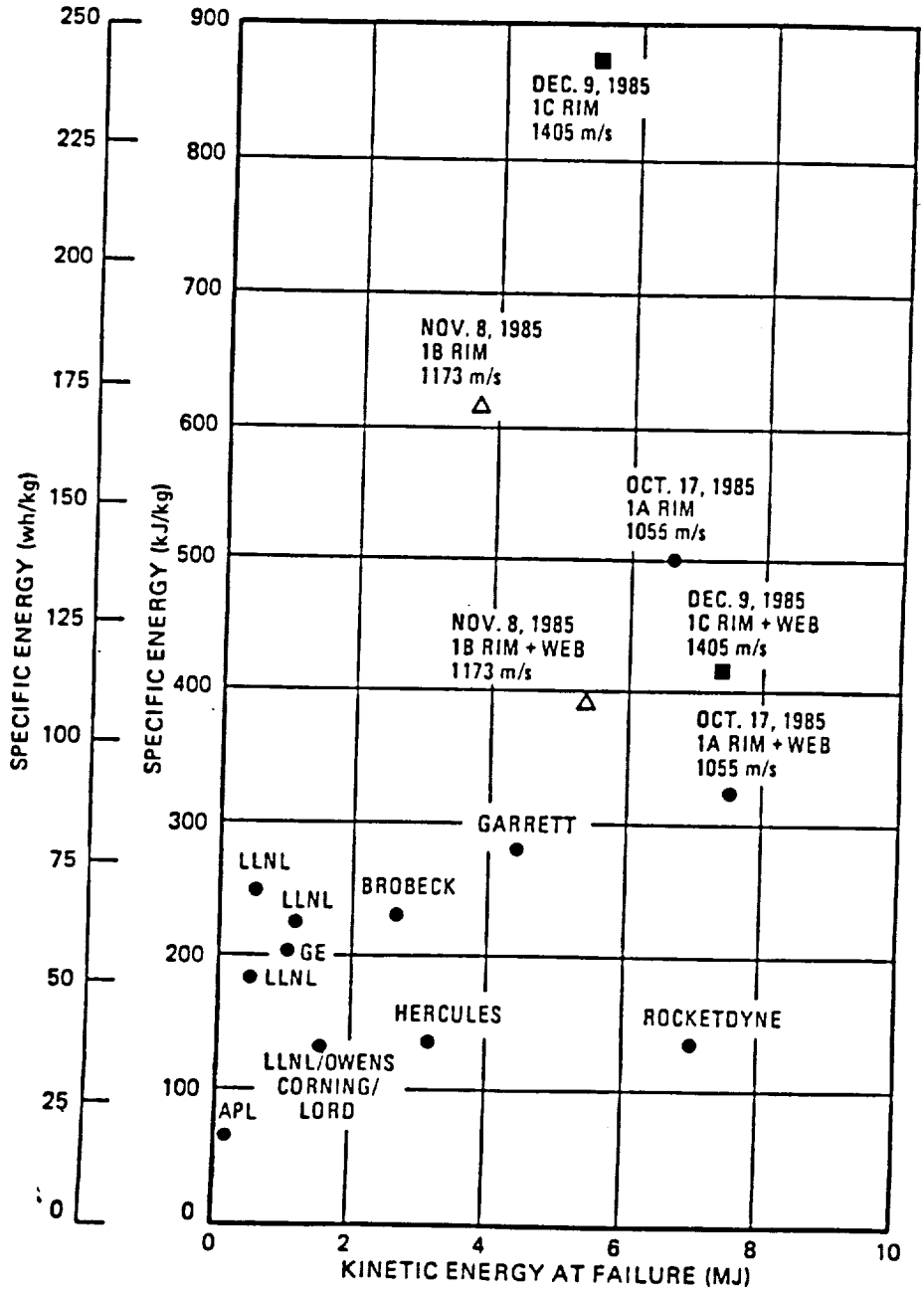

Figure 21. Comparison of Flywheel Rotor Performance

Table IX. Flywheel Demonstration Test Results

1985 DATE	DEMO UNIT	VELOCITY (m/s)	SPECIFIC ENERGY kJ/kg (Wh/kg)	RESULT
Oct. 17	1A	1055.	495 (138)	WEB FAILURE, SMALL CRACK. NO RIM DAMAGE.
Nov. 8	1B	1173.	605 (168)	STOPPED FOR INSPECTION. NO DAMAGE.
Nov. 12	1C	1221	663 (184)	STOPPED FOR INSPECTION. NO DAMAGE.
Dec. 9	1C	1405	878 (244)	INTENTIONAL FAILURE TEST.

4.3 Material Selection

The properties which are required to determine the performance of a composite flywheel are material density, working fiber strength, and working matrix strength. Table X lists these properties for the four composite materials which were identified in Reference 16. The properties of graphite/epoxy represent recent improvements in high-strength graphite as presented in Reference 22.

Table X. Composite Material Properties

	Gr/Ep	B/Ep	B/Al	SiC/Al
DENSITY (kg/m^3)	1700	2020	2630	2910
MATRIX STRENGTH (MPA)	146	69	139	110
FILAMENT STRENGTH (MPA)	1978	1324	1413	1517

The momentum density of annular flywheels constructed from these materials is readily calculated from the theory of

elasticity [19] with the maximum radial stress set less than or equal to the matrix strength and the maximum tangential stress set less than or equal to the filament strength. Figure 22 presents the momentum density for 1000 rpm annular flywheels constructed from each of these materials as a function of the radial aspect ratio (α) of the flywheel (inner to outer diameter ratio). For thick-walled flywheels (small α), the design is limited by radial stresses. For thin-walled flywheels (α approaching unity), the design is limited by tangential stresses. Of the candidate materials, graphite/epoxy has the highest momentum density.

4.4 Sizing Analysis

The flywheel for the slew actuator must store sufficient angular momentum along its spin axis (h_f) to meet the required amount of angular momentum storage (H_m). For CMGs with a limited gimbal angle (δ_{max}), the total spin-axis angular momentum is calculated as follows.

$$2 \cdot h_f \cdot \sin(\delta_{max}) = H_m \tag{4.2}$$

The total mass of the flywheels (M_f) is determined from the spin-axis angular momentum and the momentum density.

$$M_f = \frac{h_f}{\rho_h} = \frac{H_m}{2\rho_h \sin(\delta_{max})} \tag{4.3}$$

ORIGINAL PAGE IS
OF POOR QUALITY

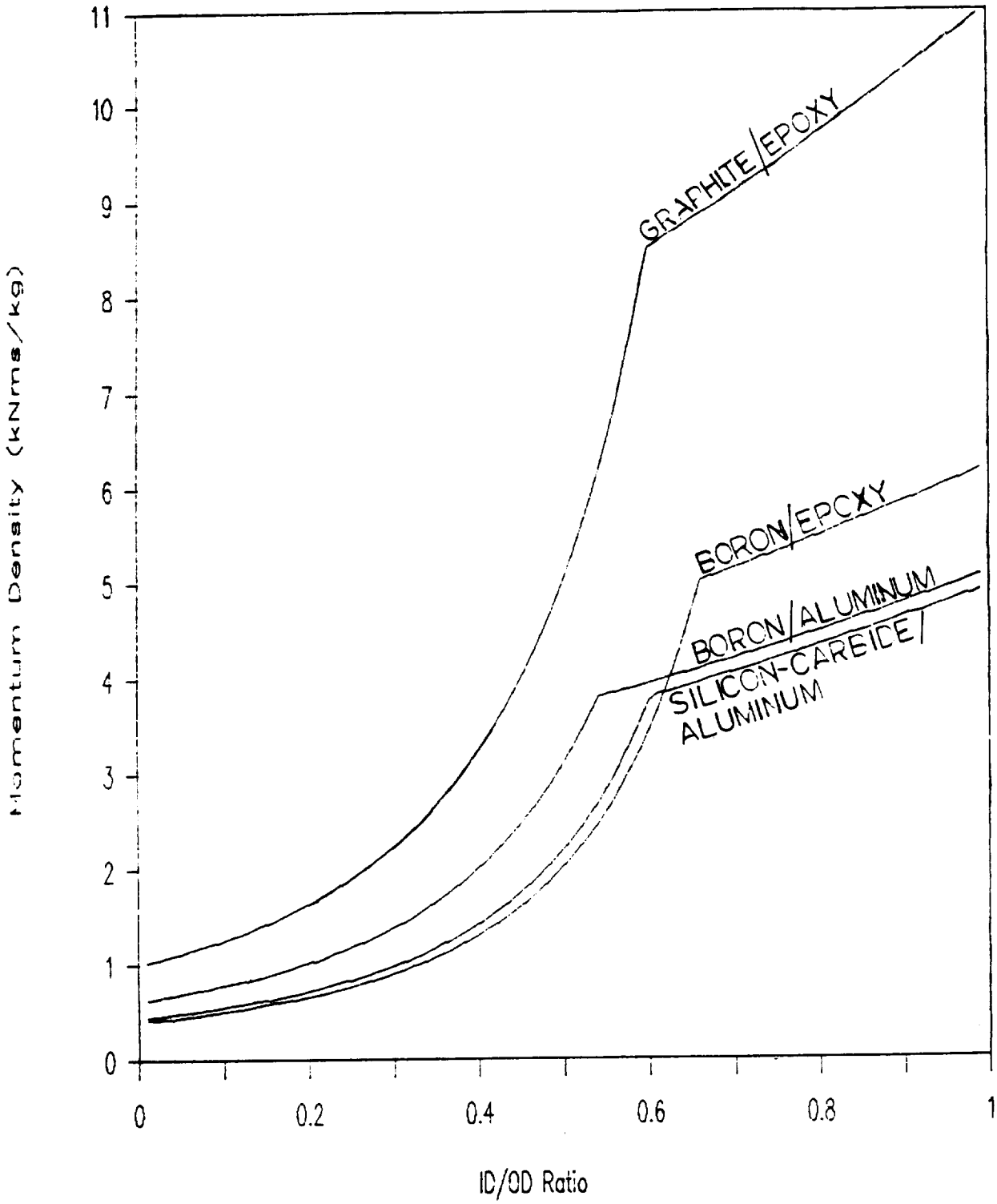

Figure 22. Comparison of Candidate Flywheel Materials

Figure 23(a) shows the mass of graphite/epoxy flywheels which are required for the slew actuator as a function of the gimbal angle. A radial aspect ratio of 0.6 and a speed of 1000 rpm are assumed. Figure 23(b) shows the flywheel mass as a function of rotational speed. The radial aspect ratio is 0.6 which is consistant with the flywheel designs presented in Reference 22. These flywheel mass numbers are substantial improvements over those of more conventional CMG rotors. Table XI compares the angular momentum storage density for a graphite/epoxy composite annulus and a typical CMG rotor for a fixed rotational speed (that of the CMG) [1].

Table XI. Flywheel Rotor Comparison

	Momentum Density (Nms/kg)
Graphite/epoxy Annulus	1,320
Steel CMG Rotor	78

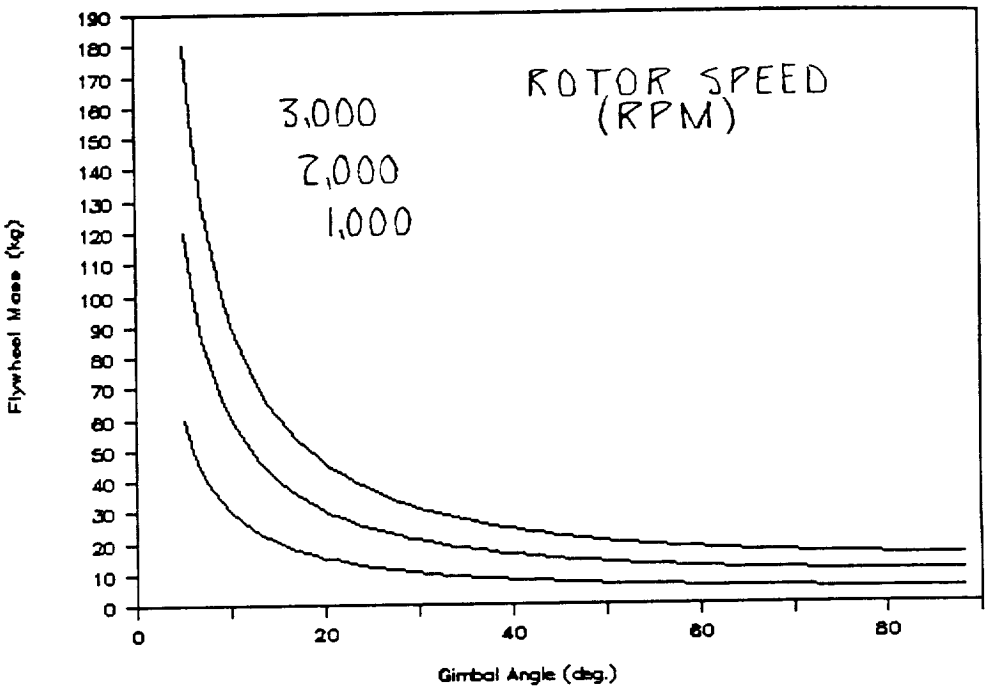

a) Affect of Gimbal Angle

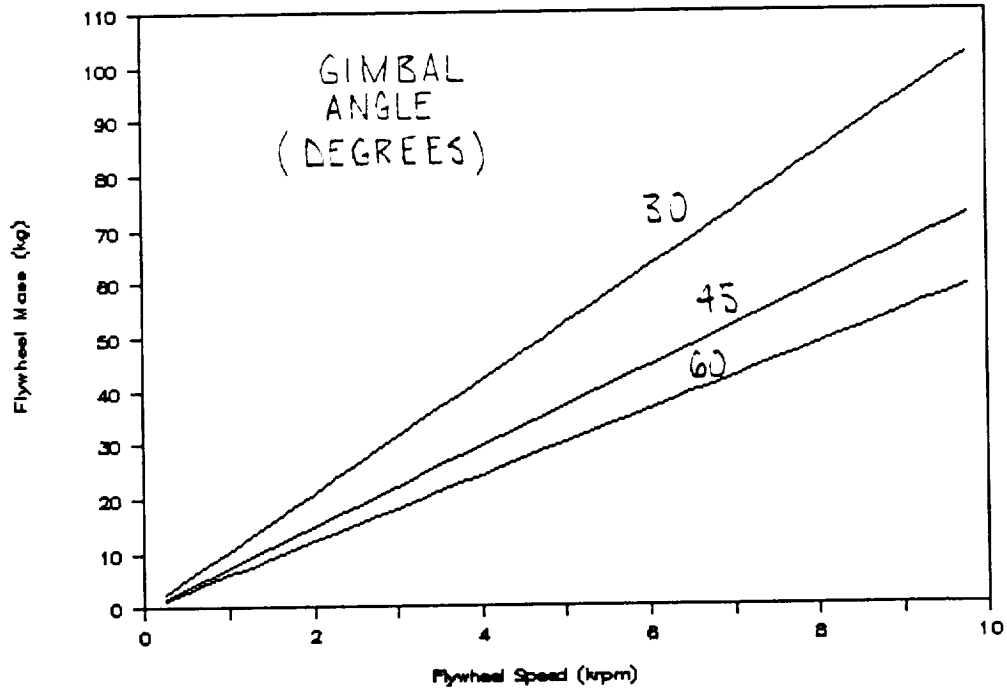

b) Affect of Rotational Speed

Figure 23. Mass of Graphite/epoxy Flywheels

5. CONVENTIONAL TECHNOLOGY LAMS ASSESSMENT

This chapter qualitatively describes large-angle, magnetic suspension (LAMS) design requirements and philosophy, discusses similarities with (and differences from) conventional magnetic bearings, and identifies a baseline concept which employs conventional technologies (wound soft-iron cores and permanent magnets). First-order electromechanical coupling equations are derived in order to describe the operation of the device. The emphasis is on fundamentals rather than analytical detail.

The LAMS concept was originally considered for a more lightly loaded application. Beginning with the original baseline design, a scaling analysis is employed to predict the performance of the LAMS in the advanced slew actuator.

5.1 Magnetic Gimballing

Several magnetically-gimballed flywheel designs have been reported in the United States [20, 21], West Germany [22], and Japan [23]. These flywheels were designed to be used in active stabilization of the attitude of small satellites. Gimbal angles up to about 2 degrees have been reported. Among these designs, several [20, 22, 24] employ thin-walled, large-diameter flywheels. One such design is the Annular Momentum Control Device (AMCD) [20]. These devices demonstrate the design freedom that results from employing magnetic bearings [26]. The AMCD, for example, is a thin hoop that is nearly six feet in diameter. Supporting this rotor by more conventional means would be

difficult, if not impossible. Other designers have developed alternative magnetic bearing systems in order to support and gimbal large, thin annuli [22, 24, 25, 27]. The former three designs are of the attraction-force type (radially-passive and axially-passive, respectively) while the latter is of the Lorentz-force type.

The calculations from Chapter 3 show that the use of small gimbal angles in the slew actuator may increase the torque requirement. The gimbal angle limits on a conventional magnetic bearing are illustrated in Figures 24(a) and 24(b). The maximum gimbal angle (δ_{max}) is determined by the ratio of the air-gap length to some other system dimension.

$$\sin(\delta_{max}) = \frac{G}{r_o} \qquad \text{(axial air gap)}$$

$$\sin(\delta_{max}) = \frac{G}{z_o} \qquad \text{(radial air gap)} \tag{5.1}$$

For a flywheel that has a 15 degree gimballing requirement, the air-gap length would have to be greater than 26% of some other system dimension. Such a large air-gap suggests a high-leakage, high-power-consumption device.

5.2 Nomenclature

The remainder of this chapter considers an alternate design approach for flywheel magnetic bearings that must be sized to gimbal a rotor through angles that are large in comparison to the

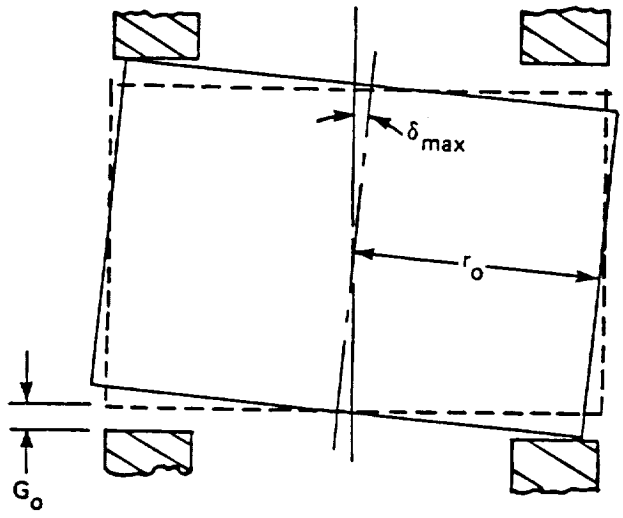

a) Axial-air-gap Designs

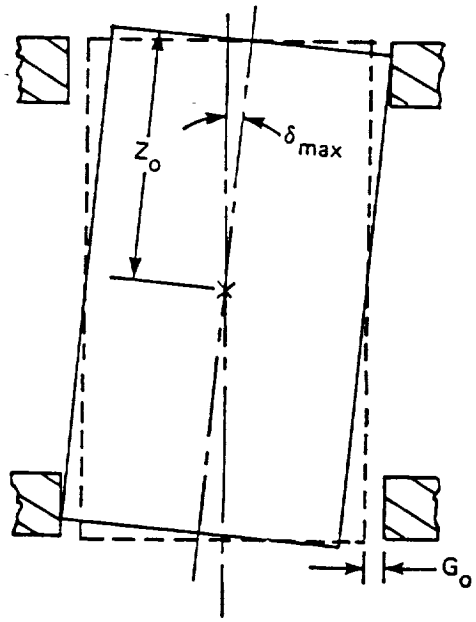

b) Radial-air-gap Designs

Figure 24. Gimballing Limits of Conventional Magnetic Bearings

ratios on the right-hand sides of Equation 5.1 [12]. Such a device will be referred to as a large-angle magnetic suspension (LAMS), although several other authors have used the title large-angle magnetic bearing (LAMB) when referencing this research [28, 29]. The word "LAMS" is used to describe the actuator of an actively controlled "LAMS system". This situation is described in Figure 25. The LAMS (actuator) applies forces and torques in response to measurements of three translational and two angular positions of the flywheel in order to regulate the translational position (center the flywheel) and servo-control the angular position (gimbal the flywheel).

5.3 LAMS Design Requirements

As a first step toward the analysis of a LAMS, this section presents a discussion of the loading, geometric symmetry, and actuation requirements that are imposed on the LAMS. These specifications are compared to those typically required of a conventional magnetic bearing.

5.3.1 Loading Requirements

The loads on a LAMS, or any other rotor bearing system, are adequately analyzed in terms of lateral, thrust, and torsional components as shown in Figure 26. Thrust and lateral loads are forces which act parallel and perpendicular to the spin axis of the rotor, while torsional loads are torques about the lateral axes of the rotor. The net force (F_L) and torque (τ_L) vectors acting on a LAMS are easily written in terms of these components.

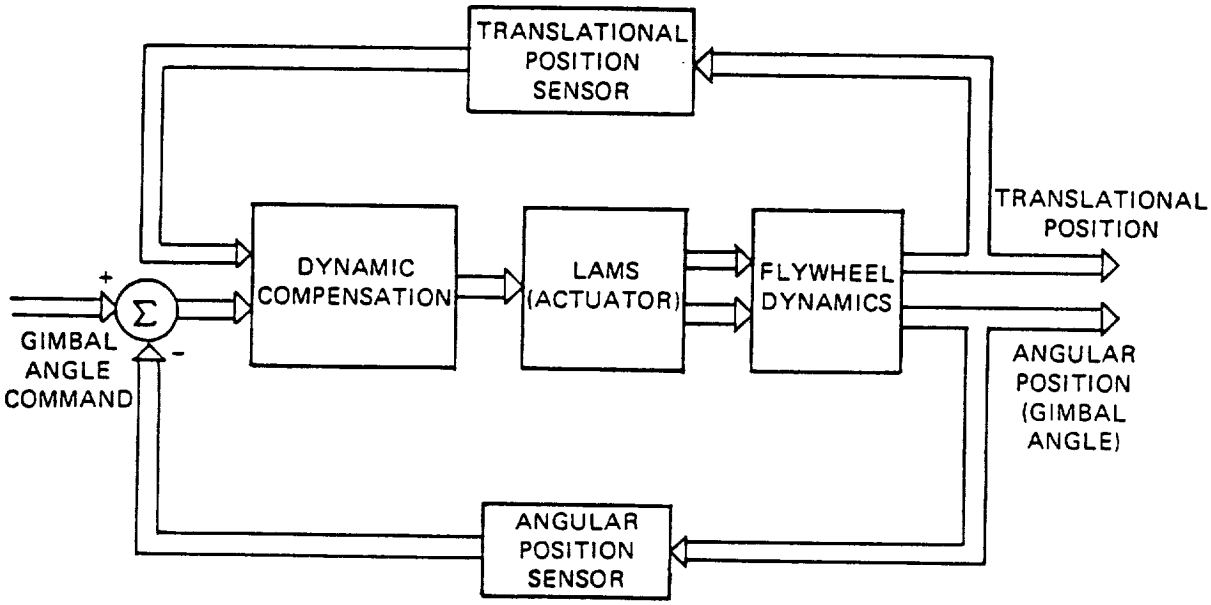

Figure 25. Large-angle Magnetic Suspension System

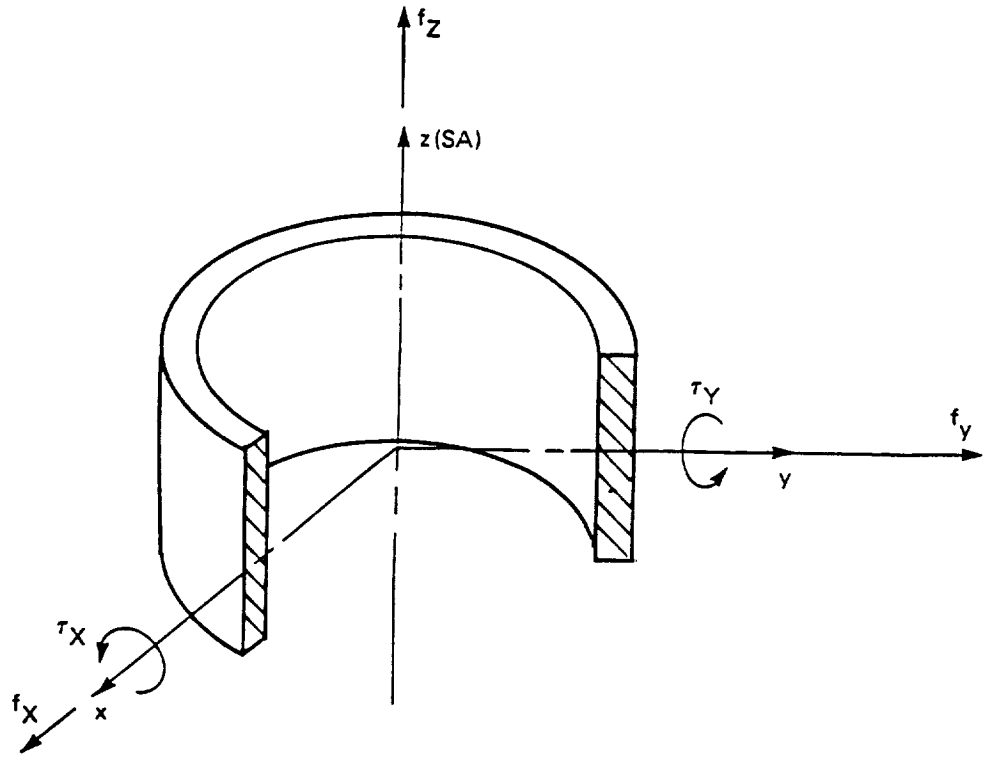

Figure 26. Rotor Bearing Loads

$$\vec{f}_L = f_X\vec{u}_X + f_Y\vec{u}_Y + f_Z\vec{u}_Z \tag{5.2}$$

$$\vec{\tau}_L = \tau_X\vec{u}_X + \tau_Y\vec{u}_Y \tag{5.3}$$

5.3.2 Geometric Symmetry Requirements

In addition to free rotation about the spin axis, a LAMS must provide controlled (but limited) angular motion about each of the orthogonal lateral axes. The existence of three axes of symmetry suggests that actuation efforts be applied in a pattern of spherical symmetry. A reference frame based on the spherical coordinates shown in Figure 27(a) is employed for analysis.

5.3.3 Actuation Requirements

Application of control effort in a pattern of spherical symmetry implies that a LAMS be analyzed in terms of forces that are spherically radial (f_R), azimuthal (f_α), elevational (f_β), or some combination of these, as is shown in Figure 27(b). At the k^{th} point of force application, which is located at position (R_k, α_k, β_k), the net force and torque resolved in orthogonal coordinates are readily written in terms of the spherical force components as follows.

$$\begin{aligned}\vec{f}_k = {} & [(f_{Rk}\cos\beta_k - f_{\beta k}\sin\beta_k)\cos\alpha_k - f_{\alpha k}\sin\alpha_k]\,\vec{u}_X \\ & + [(f_{Rk}\cos\beta_k - f_{\beta k}\sin\beta_k)\sin\alpha_k - f_{\alpha k}\cos\alpha_k]\,\vec{u}_Y \\ & + (f_{Rk}\sin\beta_k - f_{\beta k}\cos\beta_k)\,\vec{u}_Z\end{aligned} \tag{5.4}$$

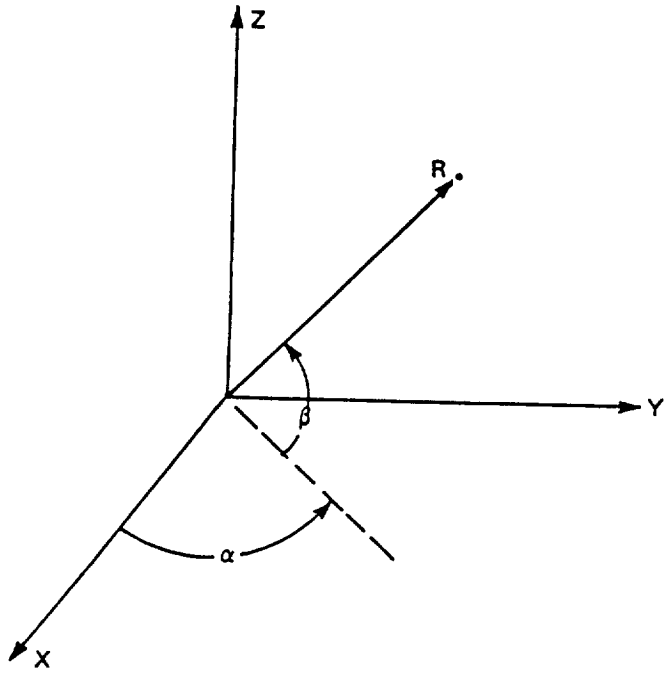

a) Spherical Coordinate System

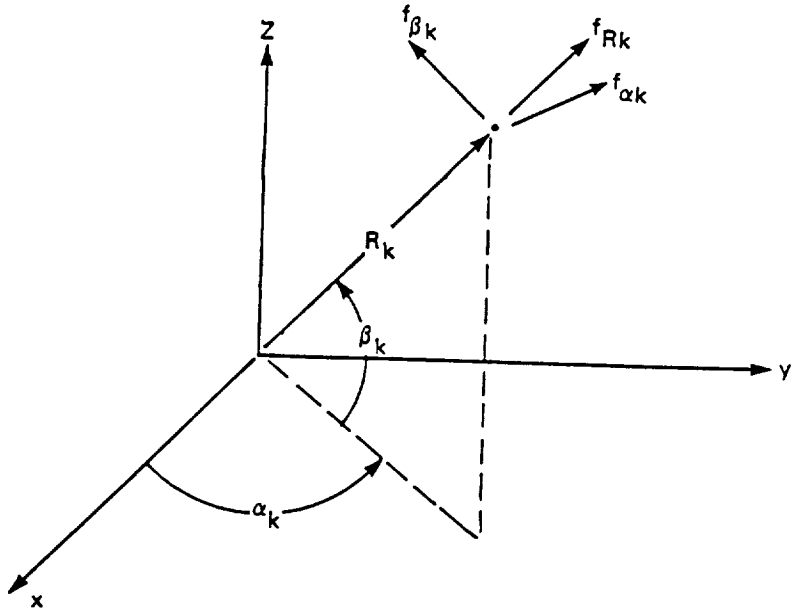

b) LAMS Force Components

Figure 27. Geometric Symmetry Considerations for a LAMS

$$\vec{\tau}_k = R_k(-f_{\alpha k}\cos\alpha_k\sin\beta_k + f_{\beta k}\sin\alpha_k)\,\vec{u}_X - R_k(f_{\alpha k}\sin\alpha_k\sin\beta_k + f_{\beta k}\cos\alpha_k)\,\vec{u}_Y + R_k f_{\alpha k}\cos\beta_k\,\vec{u}_Z \quad (5.5)$$

To meet the load requirements, the forces at each of N_1 points must satisfy the following.

$$f_X = \sum_{k=1}^{N_1} [(f_{Rk}\cos\beta_k - f_{\beta k}\sin\beta_k)\cos\alpha_k - f_{\alpha k}\sin\alpha_k] \quad (5.6)$$

$$f_Y = \sum_{k=1}^{N_1} [(f_{Rk}\cos\beta_k - f_{\beta k}\sin\beta_k)\sin\alpha_k + f_{\alpha k}\cos\alpha_k] \quad (5.7)$$

$$f_Z = \sum_{k=1}^{N_1} f_{Rk}\sin\beta_k + f_{\beta k}\cos\beta_k \quad (5.8)$$

$$\tau_X = \sum_{k=1}^{N_1} R_k(-f_{\alpha k}\cos\alpha_k\sin\beta_k + f_{\beta k}\sin\alpha_k) \quad (5.9)$$

$$\tau_Y = \sum_{k=1}^{N_1} R_k(f_{\alpha k}\sin\alpha_k\sin\beta_k + f_{\beta k}\cos\alpha_k) \quad (5.10)$$

$$0 = \sum_{k=1}^{N_1} R_k f_{\alpha k}\cos\beta_k \quad (5.11)$$

Equation 5.11 precludes first-order interaction between the LAMS and the drive.

5.4 Baseline LAMS Design

Examination of Equations 5.6-5.11 provides some insights into possible ways to design a LAMS. The simplest way to satisfy Equation 5.11 is to not employ forces that act in the azimuthal direction ($f_{\alpha k} = 0$, for all k). With this constraint satisfied, it becomes clear that employing either a combination of spherically radial and elevational forces or elevational forces alone will be a satisfactory configuration.

As with conventional magnetic bearings, LAMS forces may be exerted through ferromagnetic-attraction or Lorentz forces. The LAMS system will operate in an all-axes-actively-controlled mode since gimballing is required. Three LAMS design options (two attraction-force and one Lorentz-force) have been identified and are discussed in detail in References 5 and 16. A detailed mass vs. power consumption trade-off analysis is presented in Chapter 7 of Reference 5. The preferred approach is the Lorentz-force design which is discussed in the following paragraphs.

5.4.1 Description of the LAMS

The Lorentz-force LAMS design shown in Figure 28(a) consists of two identical actuators, each containing a rotor and a stator. Each rotor contains an axially oriented permanent magnet and sufficient core material to yield a magnetic field in the air gap which is approximately spherically radial in the region near the air gap.

$$\vec{B} = B_g \vec{u}_R \qquad (5.12)$$

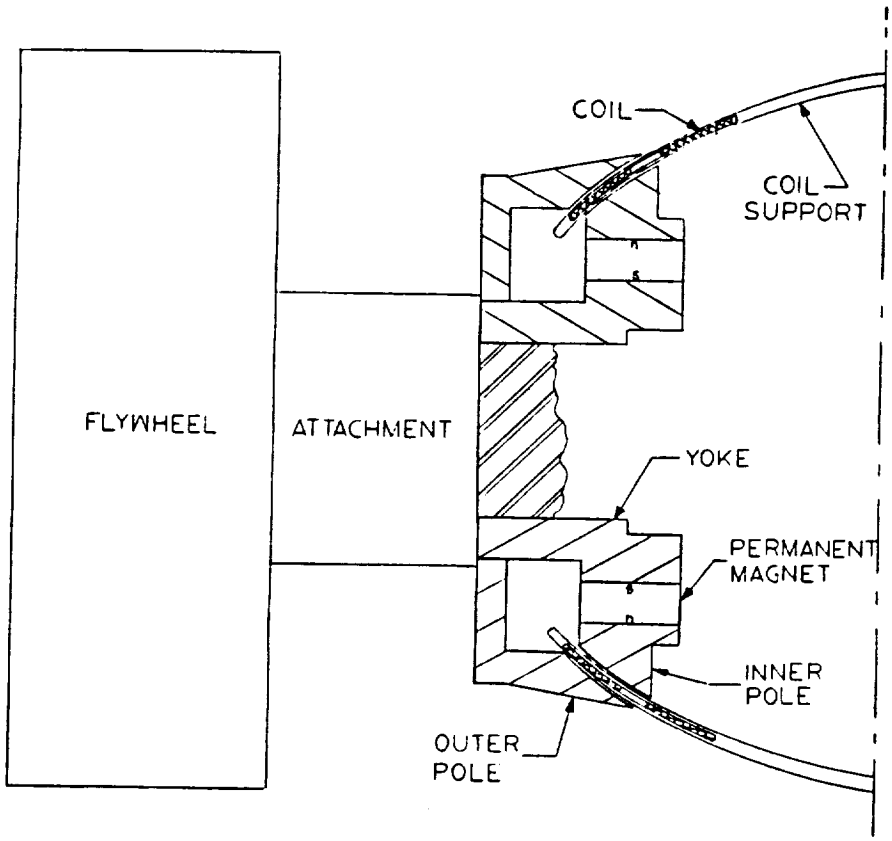

a) Section View

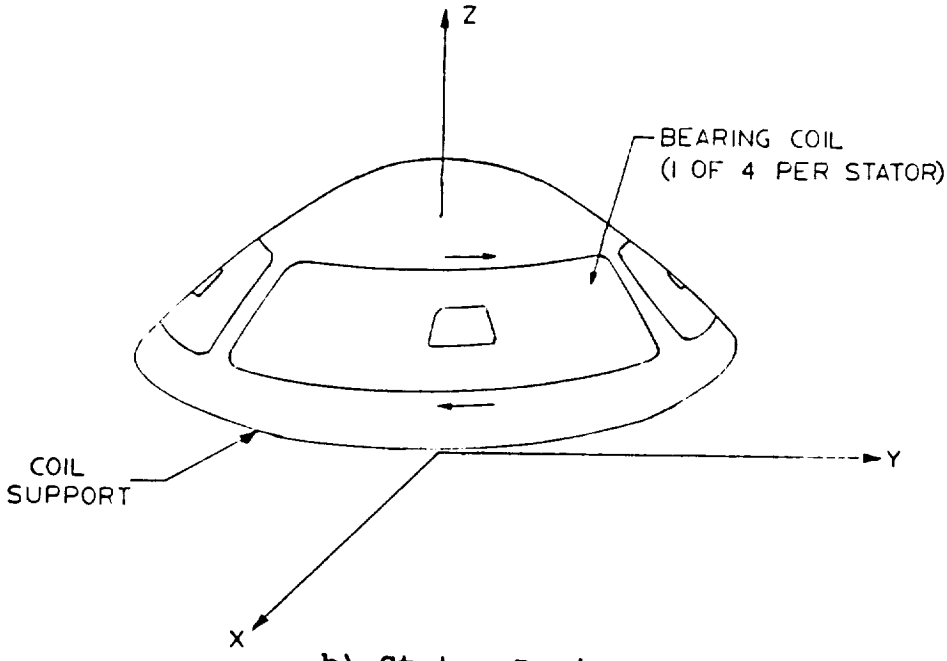

b) Stator Design

Figure 28. Design of the LAMS

Each stator consists of a thin shell containing four control coils as is shown in Figure 28(b). The figure also shows the direction for positive current. Figures 29(a) and 29(b) show the active region (V_1) of a stator coil and define the necessary parameters.

Figure 30 shows the coil numbering system that is employed for analysis of the PM-field Lorentz-force LAMS (coils 2 and 6 are hidden). The figure also shows the positive direction of current flow for a top (No. 4) and a bottom (No. 8) coil. Positive current produces a positive azimuthal current density ($J_{\alpha k}$) vector in the active region.

$$\vec{J}_k = J_{\alpha k}\vec{u}_\alpha \tag{5.13}$$

5.4.2 LAMS Loading

The force density vector at a point (R_k, α_k, β_k) within the k^{th} coil is the cross product of the current and flux density vectors.

$$\vec{\rho}_{fk} = \vec{J}_k \times \vec{B}$$

$$= B_g J_{\alpha k}\vec{u}_\beta \tag{5.14}$$

$$= B_g J_{\alpha k}[(\sin\beta_k\cos\alpha_k)\vec{u}_x + (\sin\beta_k\sin\alpha_k)\vec{u}_y - \cos\beta_k\vec{u}_z]$$

The net force (f_k) exerted on the rotor by the k^{th} coil is found by integrating the negative of the force density over the fraction of the active region which contains wire. The fill factor (η_w) is the fraction of the volume that contains wires.

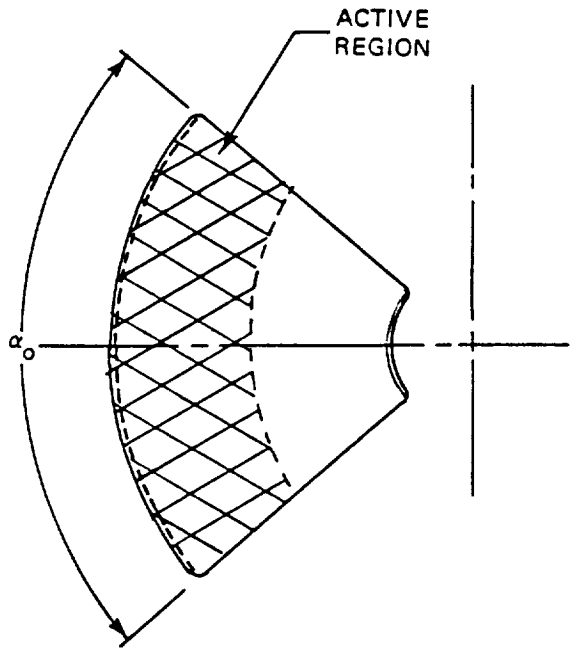

a) Plan View

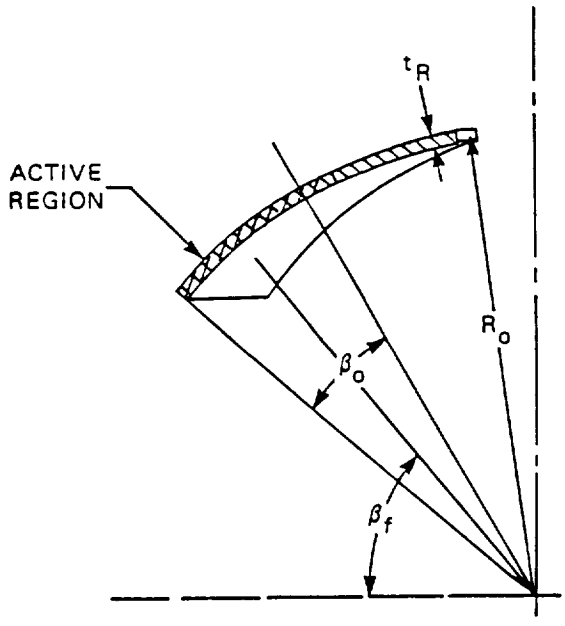

b) Section View

Figure 29. Active Region of the LAMS

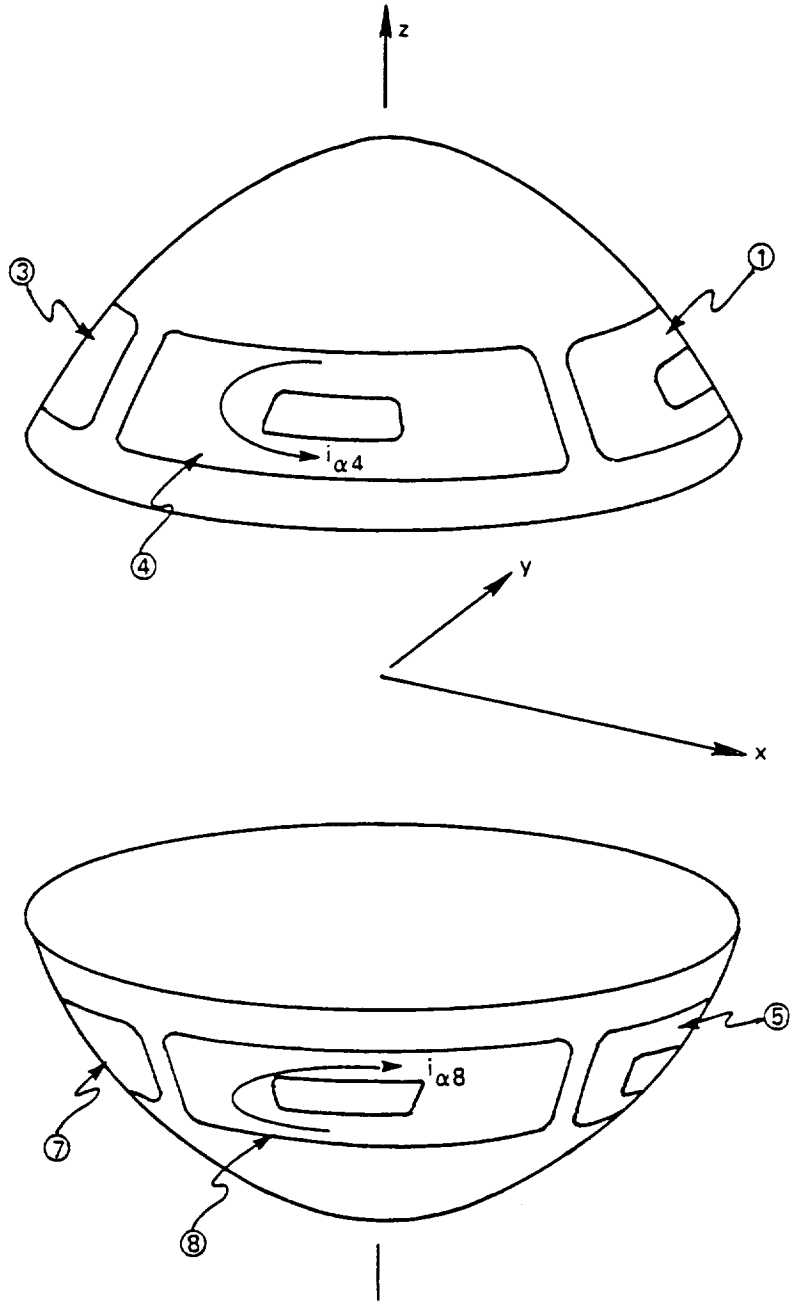

Figure 30. Stator Numbering System for the LAMS

$$\vec{f}_k = -\eta_w \iiint_{V_1} \vec{\rho}_{fk}\, dV$$

$$= -\iiint_{V_1} \vec{\rho}_{fk}\, R_k^2 \cos\beta_k\, dR_k d\beta_k d\alpha_k \qquad (5.15)$$

The limits of integration for the active region are printed below.

$$R_o - \frac{1}{2} t_R < R_k < R_o + \frac{1}{2} t_R$$

$$\frac{\pi}{2}(k-1) - \frac{1}{2}\alpha_o < \alpha_k < \frac{\pi}{2}(k-1) + \frac{1}{2}\alpha_o \qquad (5.16)$$

$$\beta_f - \frac{1}{2}\beta_o < \beta_k < \beta_f + \frac{1}{2}\beta_o$$

The net force vector components (f_{Xk}, f_{Yk}, f_{Zk}) expressed in Cartesian coordinates are found by substituting Equation 5.14 into Equation 5.15 and evaluating the triple integral over the region specified by the inequalities of Equation 5.16. The results are as follows.

$$f_{Xk} = -\eta_w B_g t_R R_o^2 \left(1 + \frac{t_R^2}{12 R_o^2}\right) \sin\left(\frac{\alpha_o}{2}\right) \sin\beta_o \sin(2\beta_f) \cos\left[\frac{\pi}{2}(k-1)\right] J_{\alpha k}$$

$$= -\eta_w c_{1r} \cos\left[\frac{\pi}{2}(k-1)\right] J_{\alpha k} \qquad (5.17)$$

$$f_{Yk} = -\eta_w c_{1r} \sin\left[\frac{\pi}{2}(k-1)\right] J_{\alpha k} \tag{5.18}$$

$$f_{Zk} = \frac{1}{2}\eta_w B_g t_R R_o^2 \left(1 + \frac{t_R^2}{12R_o^2}\right)\alpha_o[\beta_o + \cos(2\beta_f)\sin\beta_o] J_{\alpha k}$$

$$= \eta_w c_{1z} J_{\alpha k} \tag{5.19}$$

The net torque vector (τ_k) and its Cartesian components (τ_{Xk}, τ_{Yk}) are found by integrating the moment of the force density over the active region.

$$R_k \vec{u}_R \times \vec{\rho}_{fk} = B_g J_{\alpha k}(-\sin\alpha_k \vec{u}_x + \cos\alpha_k \vec{u}_y) \tag{5.20}$$

$$\tau_{Xk} = \eta_w B_g t_R R_o^3 \left[4 + \left(\frac{t_R}{R_o}\right)^2\right]\sin\left(\frac{\alpha_o}{2}\right)\sin\left(\frac{\beta_o}{2}\right)\cos\beta_f \sin\left[\frac{\pi}{2}(k-1)\right] J_{\alpha k}$$

$$= \eta_w R_o c_{1t} \sin\left[\frac{\pi}{2}(k-1)\right] J_{\alpha k} \tag{5.21}$$

$$\tau_{Yk} = -\eta_w c_{1t} \cos\left[\frac{\pi}{2}(k-1)\right] J_{\alpha k} \tag{5.22}$$

Figure 31 is a vector diagram that shows the excitation that is required to produce a lateral force (f_X) in the positive x-direction. The coils that produce forces in the x-z plane are excited such that the axial components of the forces cancel.

$$-J_{\alpha 1} = J_{\alpha 3} = J_{\alpha 5} = -J_{\alpha 7} = J_X \tag{5.23}$$

$$f_X = \eta_w \sum_{k=1}^{8} c_{1r} \cos\left[(k-1)\frac{\pi}{2}\right] J_{\alpha k} = 4\eta_w c_{1r} J_X \tag{5.24}$$

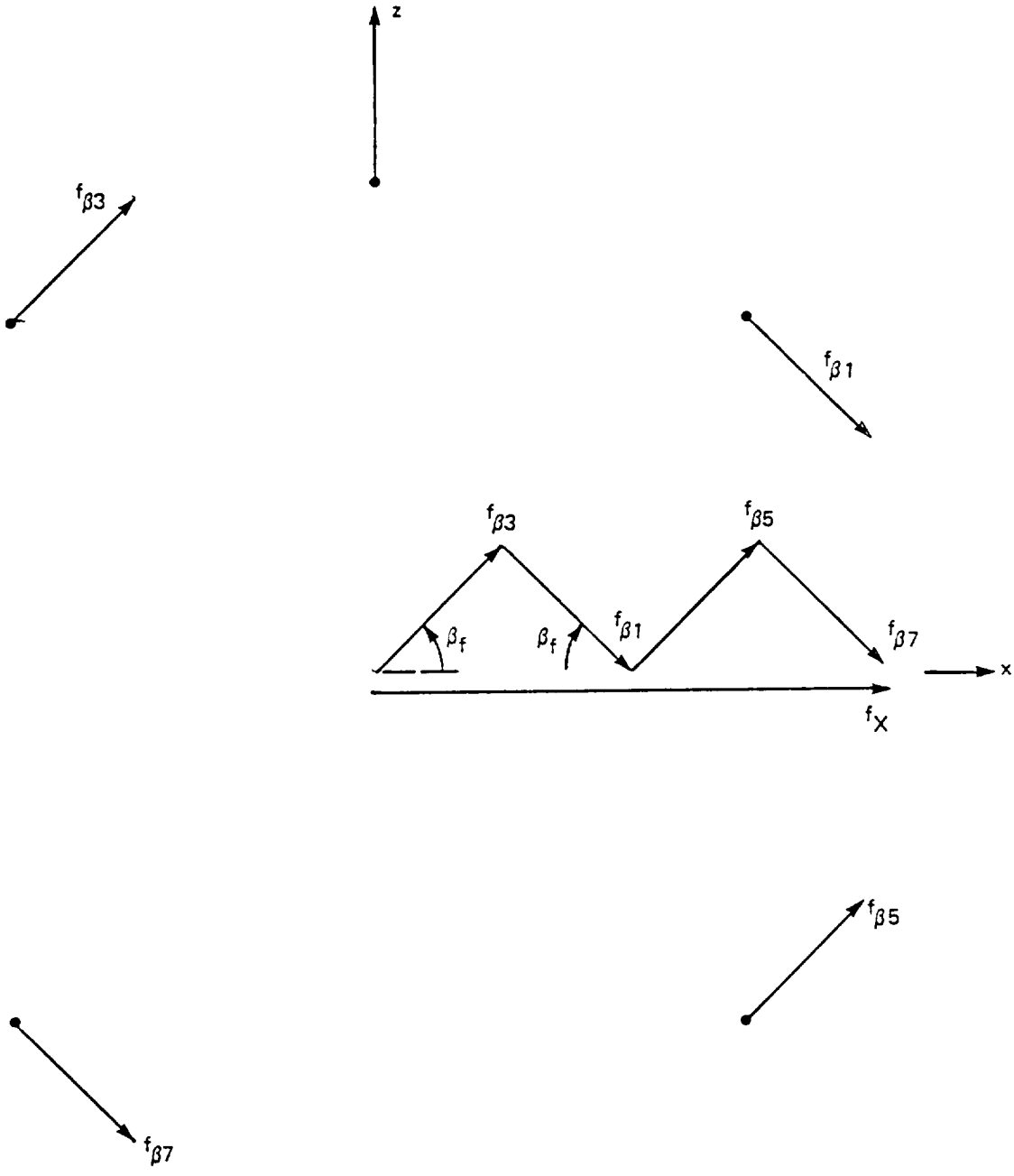

Figure 31. Lateral-force Excitation for the LAMS

Figures 32(a) and 32(b) are vector diagrams (in the x-z and y-z planes, respectively) that show the excitation that is required to produce a thrust force (f_Z). All of the coils are excited to produce positive elevational forces.

$$J_{\alpha k} = J_z \qquad \text{(for all k)} \tag{5.25}$$

$$f_Z = \eta_w \sum_{k=1}^{8} c_{1z} J_{\alpha k} = 8\eta_w c_{1z} J_z \tag{5.26}$$

Figure 33 shows the elevational force vectors that combine to produce a torque about the positive y-axis (τ_Y). Spherically opposed pairs of coils (Nos. 1, 7 and 3, 5) are excited in opposition to produce a pure torque.

$$-J_{\alpha 1} = J_{\alpha 3} = -J_{\alpha 5} = J_{\alpha 7} = J_t \tag{5.27}$$

$$\tau_Y = \eta_w \sum_{k=1}^{8} R_o c_{1t} \cos\left[(k-1)\frac{\pi}{2}\right] J_{\alpha i} = 4\eta_w R_o c_{1t} J_t \tag{5.28}$$

5.4.3 Performance of the Baseline LAMS

Reference 16 provides details concerning the design of two LAMS systems for an application where both the kinetic energy and angular momentum of a flywheel were used in a spacecraft. Systems which use flywheels for both attitude control and energy storage have been given a number of names including integrated power and attitude control systems (IPACS) [28, 30] and combined attitude reference and energy storage systems (CARES) [5, 21]. Two designs are identified in Reference 5.

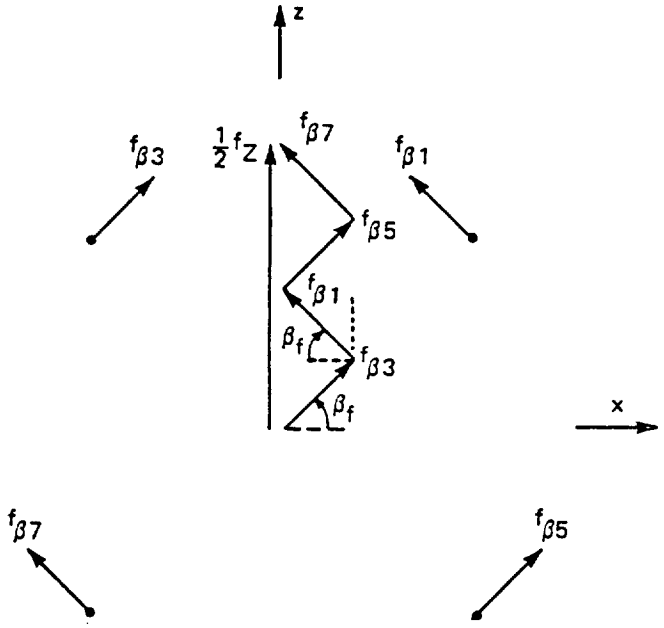

a) x-z Plane

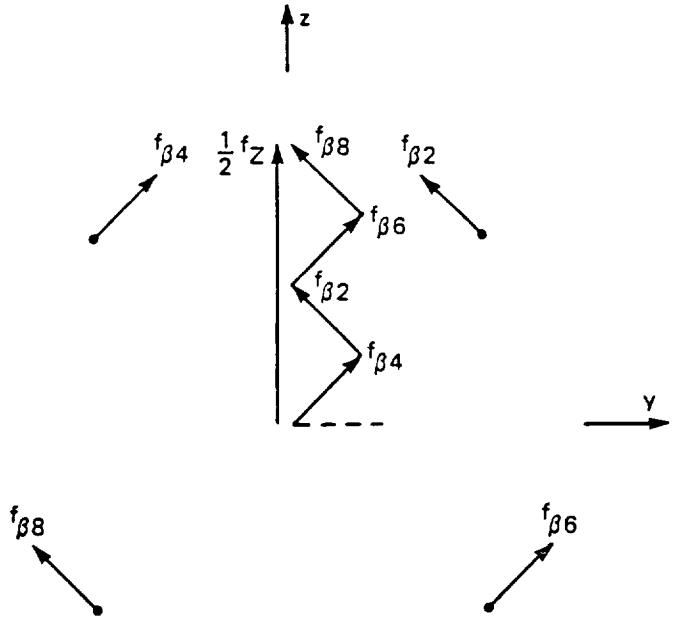

b) y-z Plane

Figure 32. Thrust-force Excitation for the LAMS

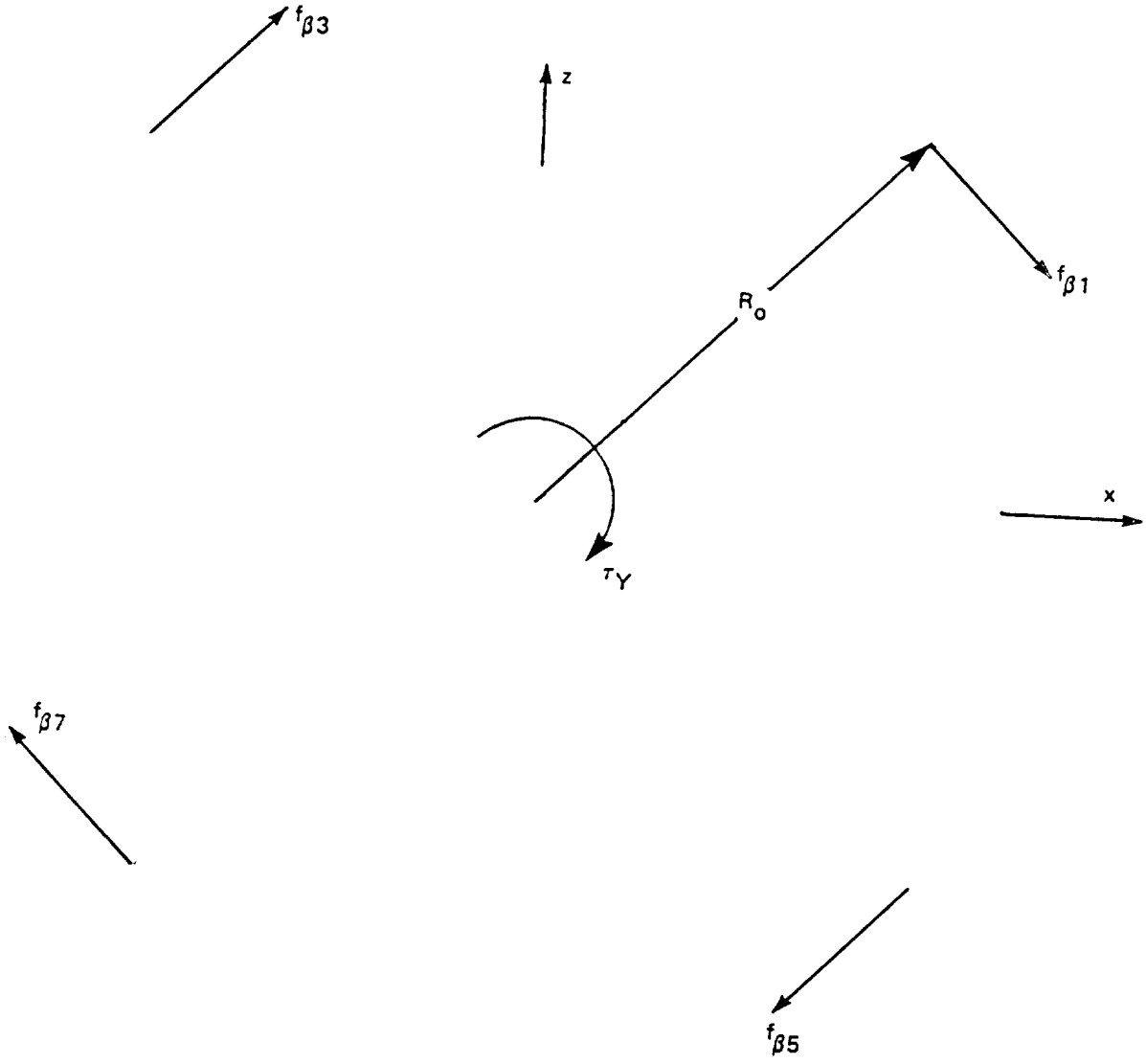

Figure 33. Torquing Excitation for the LAMS

These designs differ from each other in terms of the amount of angular freedom (maximum gimbal angle). These designs represent refinements of the two baseline designs presented in Reference 16. Table XII contains a breakdown, by component, of the mass of each LAMS system and the power consumed in applying maximum torque (300 Nm).

Table XII. Baseline LAMS Systems

Torque (Nm)	300	300
Angular Freedom (deg.)	9	15
Spherical Radius (cm)	26.8	24.3
Mass Components (kg)		
Rotor Iron	69	140
PM	13	18
Rotor Total	82	158
Conductor	14	20
Coil Support	4	2
Stator Total	18	22
Total LAMS Mass	100	180
Power Consumption (W)	400	400

5.5 LAMS Scaling

The geometry of the LAMS is sufficiently complicated that it does not lend itself to simple closed-form expressions for mass and power consumption. An alternate method for estimating these quantities is to apply basic scaling laws for electromechanical devices.

5.5.1 Fixed Quantities

A typical initial assumption is that the relative magnitudes of all dimensions of the device remain fixed (constant relative geometry). This implies that any dimension of the device (χ) will scale linearly with some "typical" dimension for the device. The nominal air-gap spherical radius (R) is a reasonable choice.

$$\chi \propto R \tag{5.29}$$

5.5.2 Mass

Assuming that the materials remain the same, the mass of the i^{th} component part of the device (m_i) is proportional to its volume (V_i) and therefore to the cube of its typical dimension.

$$m_i \propto V_i \propto R^3 \tag{5.30}$$

If a different material is substituted for the j^{th} component, its mass (m_j) will also be proportional to the material density (ρ_j) of that material.

$$m_j \propto \rho_j V_j \propto \rho_j R^3 \tag{5.31}$$

5.5.3 Electric and Magnetic Quantities

The magnetic flux density (B_g) and current density (J_c) in the active region will dictate the magnitude of the Lorentz force interaction. This section considers scaling laws for these quantities.

5.5.3.1 Flux Density. To first order the magnetic field in the air gap (B_g) is related to the energy product (B_dH_d) of the magnet as well as the volumes of the air gap (V_g) and the

permanent magnet (V_m) and the permeability of free space (μ_o) [31].

$$\frac{B_g^2 V_g}{\mu_o} = (B_d H_d)\, V_m \tag{5.32}$$

Under the assumption of fixed relative geometry, the ratio of the volumes of the air gap and permanent magnet will remain fixed. Assuming the same permanent magnet material, Equation 5.32 implies that the air-gap flux density of geometrically similar permanent-magnet structures are equal.

$$B_g^2 \propto \frac{V_m}{V_g} \propto \frac{R^3}{R^3} \tag{5.33}$$

$$B_g = \text{const.}$$

5.5.3.2 Current Density. The current density in uncooled conductors is limited by the adiabatic temperature rise (ΔT) in the conductors due to ohmic heating. Heat ($\dot{q}$) is dissipated in the conductor volume (V_c) due to the current density (J_c) and finite conductivity (σ).

$$\dot{q} = \frac{J_c^2 V_c}{\sigma} \tag{5.34}$$

The temperature rise (ΔT) during the slew period (T_s) is calculated under the assumption that all of the heat dissipation is stored in the heat capacity (C_p) of the conductor mass (m_c).

$$\dot{q} T_s = m_c C_p \Delta T$$

$$\frac{J_c^2 V_c T_s}{\sigma} = \rho_c V_c C_p (\Delta T) \tag{5.35}$$

$$\Delta T = \frac{J_c^2 T_s}{\sigma \rho_c C_p} \tag{5.36}$$

Assuming that an electromagnetic device is sized for a specified temperature rise per unit time implies that current density will scale as the square root of the product of material properties

$$J_c \propto \sqrt{\sigma \rho_c C_p} \tag{5.37}$$

For a fixed conductor material, of course, the current density is constant.

5.5.4 Torque

The torque applied by the LAMS is determined from the integral of the force density integrated over the active volume.

$$\tau = \iiint r \times (J \times B)\, dV$$

$$\propto J_c B_g R^4 \tag{5.38}$$

$$\propto J_c R^4$$

For a fixed conductor material, the nominal radius is therefore proportional to the fourth root of the torque.

$$R \propto \tau^{1/4} \tag{5.39}$$

When a different conductor material is used, the nominal radius is proportional to the fourth root of the quotient of the torque and current density.

$$R \propto \left(\frac{\tau}{J_c} \right)^{1/4} \tag{5.40}$$

5.5.5 Power Dissipation

The power (P) dissipated by the LAMS is the ohmic dissipation in the conductors.

$$P = \frac{J_c^2 V_c}{\sigma} \propto \frac{J_c^2}{\sigma} R^3 \tag{5.41}$$

For a fixed conductor material, the power consumption is proportional to the nominal radius cubed.

$$P \propto R^3 \tag{5.42}$$

For a different conductor material, the expression for the current density is substituted.

$$\begin{aligned} P &= \frac{J_c^2 V_c}{\sigma} \\ &\propto \rho C_p R^3 \end{aligned} \tag{5.43}$$

5.5.6 Scaling Results

The performance of the LAMS can be scaled from the designs that are presented in Table XII to a size which is consistent

with the slew actuator by the use of Equations 5.28 to 5.43.

Both copper and aluminum conductors were considered. Table XIII presents the relative properties and current density of these two materials.

Table XIII. Relative Conductor Properties

	Copper	Aluminum
Mass Density (relative)	1.00	0.30
Conductivity (relative)	1.60	1.00
Specific Heat (relative)	1.00	2.30
Current Density (relative)	1.26	0.83

Table XIV shows the results of the scaling analysis. The torque levels represent the required precession torques for the limited gimbal angles of these two designs. As discussed in Chapter 3, these levels are quite large in comparison to the required control torque because the flywheels must follow the motion of the spacecraft.

The use of aluminum conductors reduces that component of the system mass. Total system mass, however, increases due to the increased size of the device. The power consumed by the LAMS with aluminum conductors is somewhat lower than the one with copper conductors.

5.6 LAMS Summary

A scaled-up version of a conventional technology LAMS cannot be considered as a viable option for use in the slew actuator. Both the mass and power consumption of the device are excessive for a space-based application.

Table XIV. LAMS Scaling Results

	Copper Conductors		Aluminum Conductors	
Torque (Nm)	33,000	33,000	33,000	33,000
Angular Freedom (deg.)	9	15	9	15
Spherical Radius (cm)	86.8	78.7	96.4	87.4
Mass Components (kg)				
Rotor Iron	2,344	4,755	3,213	6,519
PM	442	611	605	838
Rotor Total	2,785	5,367	3,818	7,357
Conductor	476	679	196	279
Coil Support	136	68	186	93
Stator Total	611	747	382	372
Total LAMS Mass	3,397	6,114	4,200	7,729
Power Consumption (W)	13,586	13,586	12,851	12,851

Conventional magnetic materials and conductors limit the performance of electromechanical devices in which they are used. The rotating magnetic circuit of the LAMS clearly dominates the mass of the device. This is due to the limited saturation induction of the soft iron and the limited flux density of the permanent magnets [5].

The capabilities of the permanent magnet also limit the magnetic field in the air gap which, in turn, limits the torque per unit current density. The elevated current density then leads to high ohmic losses in the conductor. The following chapter discusses the use of a superconducting coil to replace the permanent magnet and soft iron magnetic circuit in the LAMS in order to eliminate these limitations.

6. SUPERCONDUCTING LAMS

This chapter describes a LAMS design which employs a superconducting magnet rather than a permanent magnet or wound core as a primary flux source. This is an alternative design for a magnetic bearing which may be used in a CMG to deliver large torques to a spacecraft without the need for an excessively massive magnetic core or the consumption of a large amount of power. The superconducting LAMS, as its name suggests, employs a superconducting coil for the elimination of all conventional magnetic structures in order to produce an energy-efficient, light-weight design. The following sections describe the construction and operation of an advanced-concept CMG which employs a superconducting LAMS.

6.1 Advanced-concept CMG

Figure 34 is a partially cut-away view which shows the rotating components (superconducting coil and flywheel) and cryogenic housing of a two-degree-of-freedom CMG which employs a superconducting LAMS. The housing contains normal (non-superconducting) coils which interact with the field produced by the superconducting coil in order to apply forces and torques to the rotor. The rotor of the CMG can be completely gimballed within the housing.

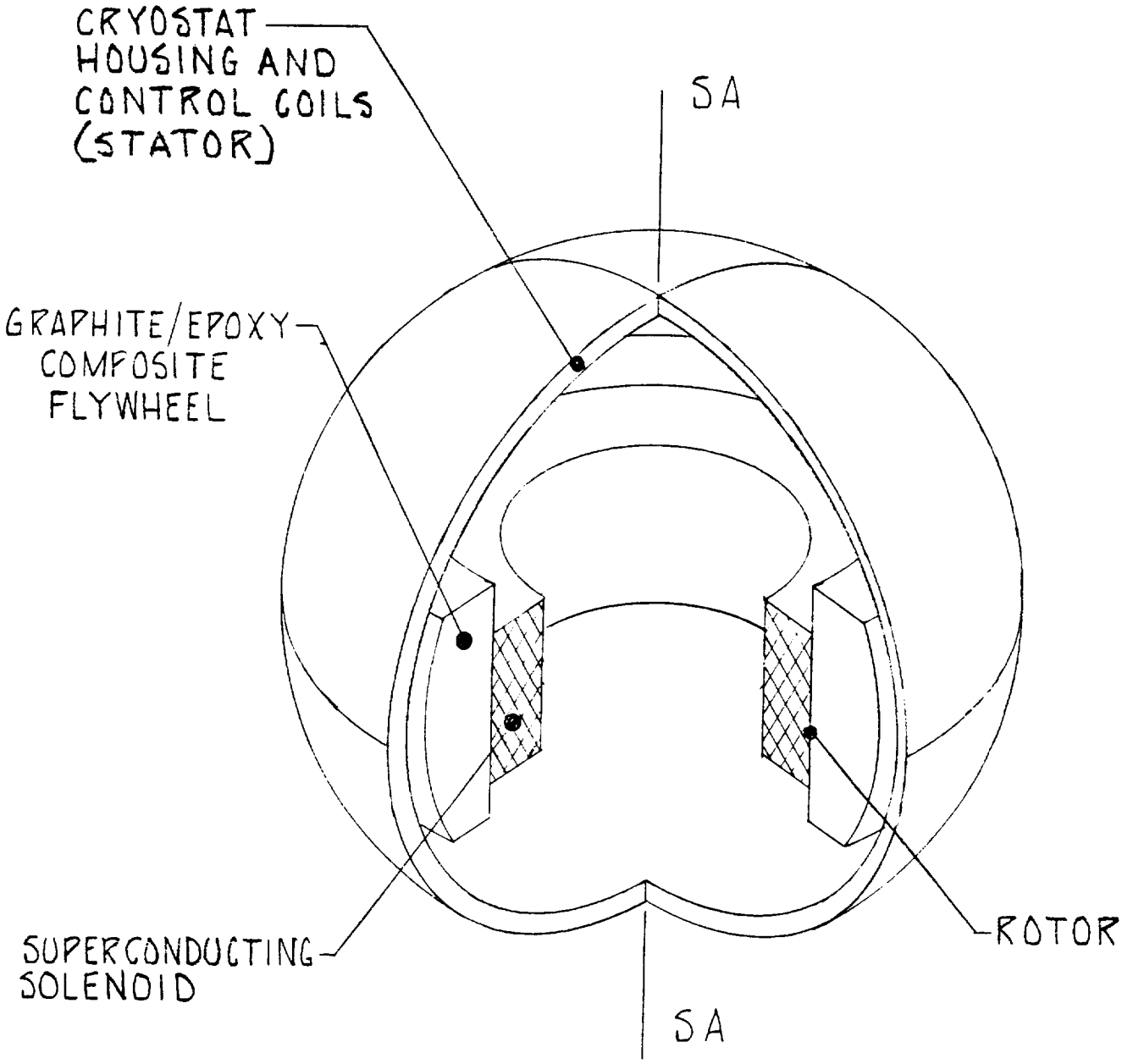

Figure 34. CMG with Superconducting LAMS

6.1.1 Rotating Components

The rotor of the CMG consists of the superconducting coil, a flywheel, and the rotor of a spin motor. The superconducting coil is the rotor of the LAMS. The spin motor is discussed in Chapter 7.

6.1.1.1 Superconducting Coil. The rotating superconducting coil is a solenoid which operates in persistant-current mode (without an electrical input). The current in the solenoid persists because of the lack of resistance in the superconducting material [32]. The spherical case which surrounds the rotating components serves as the cryostat for the superconducting solenoid. The superconducting coil is maintained below its critical temperature by a bath of liquid helium which fills the cryostat.

Electromagnetic forces produced by interactions between the field of the solenoid and currents in stationary control coils center and support the rotor with respect to the housing. This configuration eliminates mechanical supports for the superconductor. The support structure, typically stainless steel wires, are a major source of heat leaks into the cryostat [32].

6.1.1.2 Flywheel. A high-strength graphite/epoxy composite flywheel of the type discussed in Chapter 4 is attached to the solenoid to provide angular momentum storage capacity. The outer diameter of the flywheel is machined to approximate a sector of a sphere. This allows the flywheel to be completely gimballed

(plus or minus 180 degrees about the lateral axes) without contact with the case. The angular freedom is not limited by the use of soft-iron magnetic circuit elements in the LAMS as the conventional-technology alternative is.

6.1.2 Stationary Components

The stationary components of the CMG are contained within a spherical annulus which surrounds the rotor. These consist of the cryostat housing, twelve control coils, and the stator of the spin motor. The control coils are the stator of the LAMS. Sensors for monitoring the position of the rotor in five degrees of freedom are also required for use as inputs for the controller of the LAMS.

6.1.2.1 Cryostat Housing. The housing of the CMG acts as a two-stage cryostat for the superconducting coil and as a refrigerated space for the normal electromagnetic components (the stators of the LAMS and spin motor.

The inner spherical shell of the cryostat surrounds the liquid helium bath in which the rotor is located. An outer spherical shell creates a spherically annular space which is filled with liquid nitrogen.

In the intermediate temperature zone (77 degrees Kelvin), the resistivity of common conductors decreases dramatically. This reduces the power consumption of the coils and also reduces the refrigeration requirement. Figure 35 shows the variation of

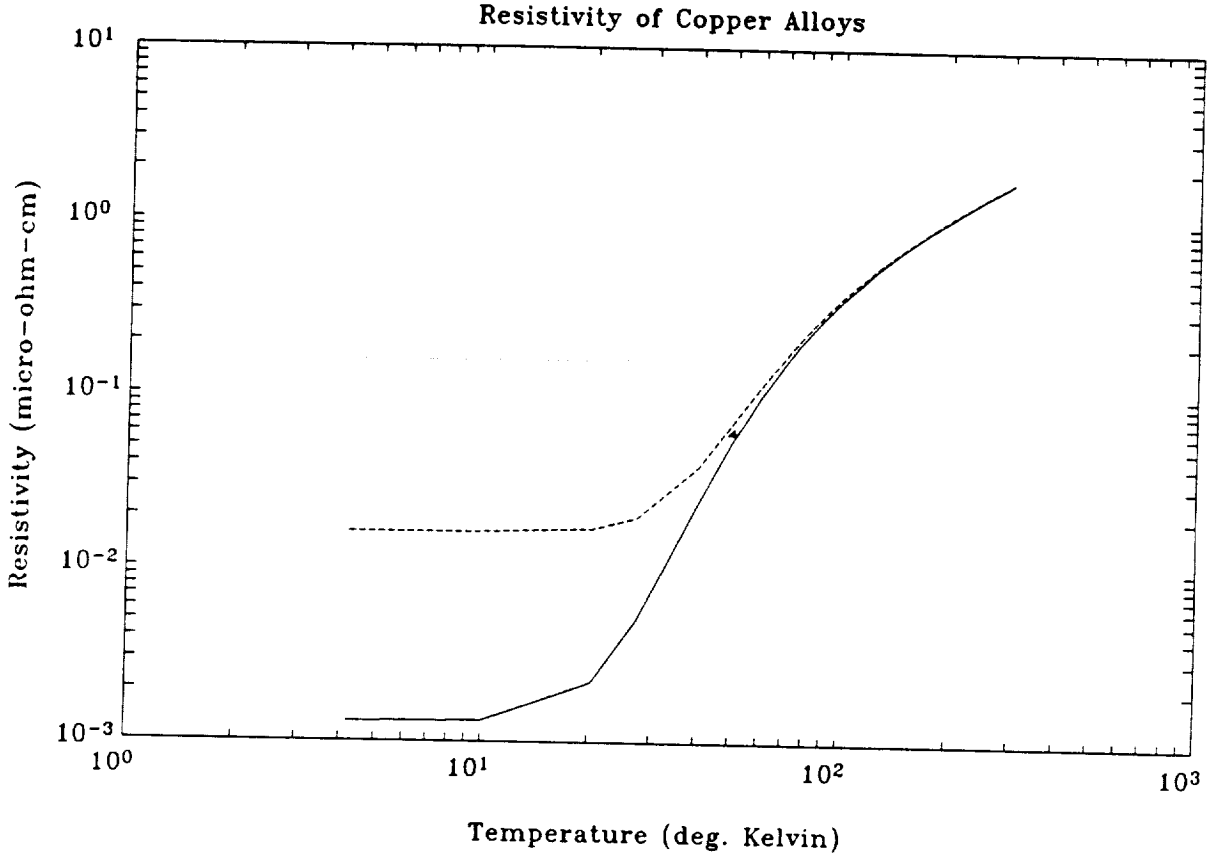

Figure 35. Resistivity of Copper

the resistivity of various grades of industrial copper with absolute temperature [37].

<u>6.1.2.2 Control Coils.</u> Figures 36(a) and 36(b) show several layers of normal coils which interact with the magnetic field produced by the superconducting solenoid. The coils shown in Figure 36(a) are used to apply forces along the lateral (diametral) axes of the rotor. Those coils shown in Figure 36(b) apply forces along the cylindrical axis of the solenoid and torques about the lateral axes. The mechanisms for the force and torque interactions are analyzed in the following section.

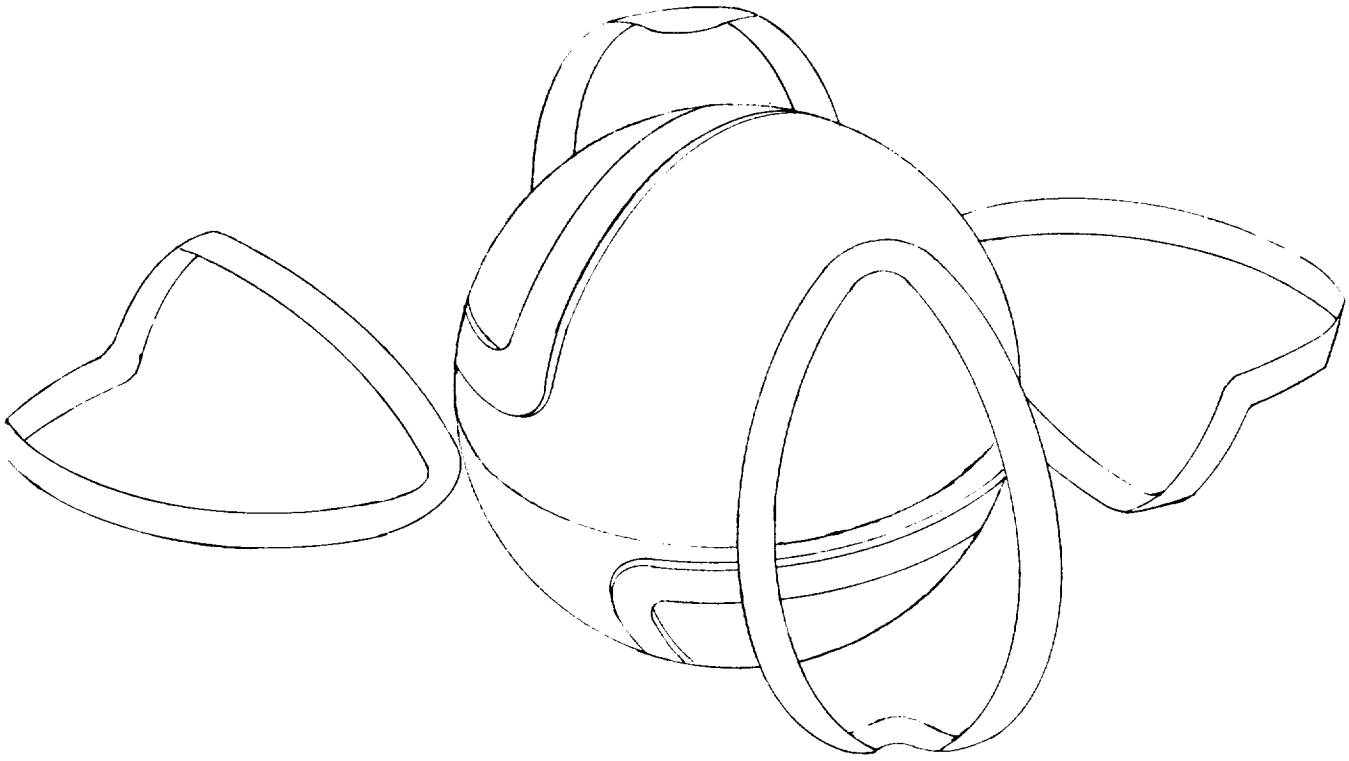

a) Lateral-force Coils

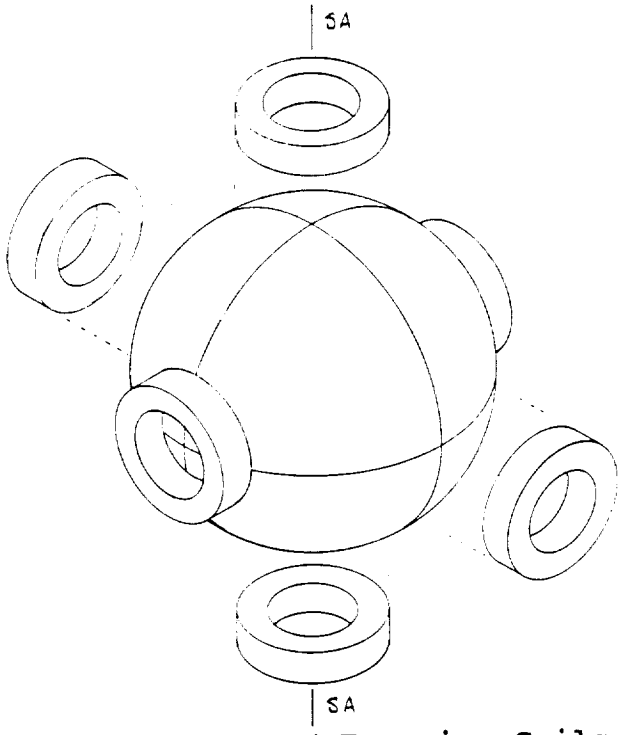

b) Thrust-force / Torquing Coils

Figure 36. Control Coils

6.2 Operation of the Superconducting LAMS

The superconducting LAMS has similarities to and differences from the conventional-technology approach described in Chapter 5. The LAMS designs are similar in that forces and torques are produced on a rotating magnetic field source as a result of interactions between the "source" field and currents in stationary "control" coils. The differences are: the mechanism which produces the source field and the construction of the rotating structure.

This section analyzes the force and torque interaction between the source and control coils. Relatively simple models are used to show the physical principles which are involved. In all cases, the spin axis of the rotor is assumed to be oriented in its nominal position.

6.2.1 Source Field

The magnetic field produced by an air-core solenoid, such as the source coil, may be approximated by the field of a concentrated magnetic dipole. The source dipole is located at the center of the real solenoid and has a dipole moment (m_S) which is equal to that of the solenoid. Although the predictive ability of this model is high, in a quantitative sense, only when the source and control coils are separated by a distance which is large in comparison to their dimensions, some valuable insights can be obtained through its use.

Figure 37 describes the geometry of a typical solenoid in terms of the inner radius (a) as well as the radial and axial aspect ratios (α and β, respectively). The dipole moment is calculated from the current density (J) in the solenoid, the inner radius (a_S), the outer radius (b_S), and the length (L_S).

$$\begin{aligned} m_S &= \frac{2}{3}\,\pi \cdot J \cdot (b_S^3 - a_S^3) \cdot L_S \\ &= \frac{2}{3}\,\pi \cdot J \cdot a^4 \cdot (\alpha_S^3 - 1) \cdot \beta_S \end{aligned} \tag{6.1}$$

Figure 27(b) shows the spherical coordinate system in which the components of the source field are most easily expressed [34]. The source field (B) is calculated from the moment of the source dipole (m_S), the spherical radius (R), and the declination angle (ϕ).

$$\begin{aligned} \vec{B} &= \frac{\mu_o}{4\pi}\,\frac{m_S}{R^3}\,[2\cos\phi\ \vec{u}_R + \sin\phi\ \vec{u}_\phi] \\ &= B_S\,[2\cos\phi\ \vec{u}_R + \sin\phi\ \vec{u}_\phi] \end{aligned} \tag{6.2}$$

6.2.2 Control Coils

A total of twelve control coils are used to produce forces and torques on the source solenoid. This section describes the shapes and locations of these coils and analyzes their interactions with the source field.

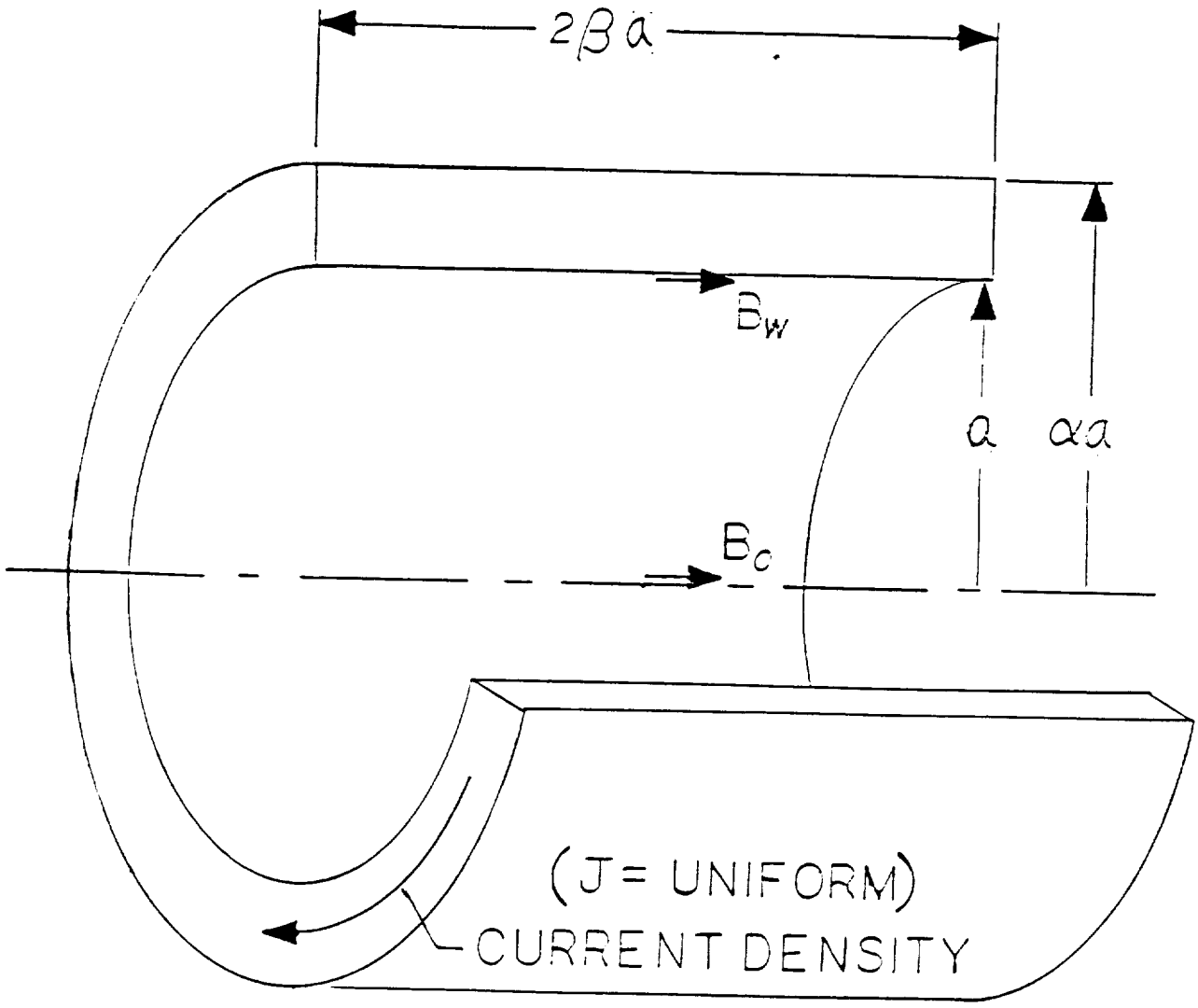

Figure 37. Typical Solenoid Geometry

6.2.2.1 Lateral-force Coils. Figure 38 shows two coils which are attached to the outer surface of the case of the superconducting CMG. The interaction of the magnetic field (B) produced by the source solenoid and the current (I) in each differential length (ds) of the coil produces a differential force vector (df).

$$\vec{df} = \vec{I} \times \vec{B} \tag{6.3}$$

The current vectors in the three sections of the upper lateral-force coil can be easily expressed in spherical coordinates.

$$\begin{aligned} \vec{I}_1 &= + I \, \vec{u}_\phi \\ \vec{I}_2 &= - I \, \vec{u}_\theta \\ \vec{I}_3 &= - I \, \vec{u}_\phi \end{aligned} \tag{6.4}$$

The Lorentz-force interaction (Equation 6.3) can be evaluated by substituting Equations 6.2 and 6.4. The results for the three sections of the upper lateral-force coil.

$$\begin{aligned} \vec{df}_1 &= - B_S \, I \, (2\cos\phi) \, \vec{u}_\theta \\ \vec{df}_2 &= B_S \, I \, [(-2\cos\phi) \, \vec{u}_\phi + (\sin\phi) \, \vec{u}_R] \\ \vec{df}_3 &= B_S \, I \, (2\cos\phi) \, \vec{u}_\theta \end{aligned} \tag{6.5}$$

The unit vectors used for spherical coordinates are easily related to those used in Cartesian coordinates [35].

$$\vec{u}_R = \sin\phi\cos\theta \, \vec{u}_x + \sin\phi\sin\theta \, \vec{u}_y + \cos\phi \, \vec{u}_z$$

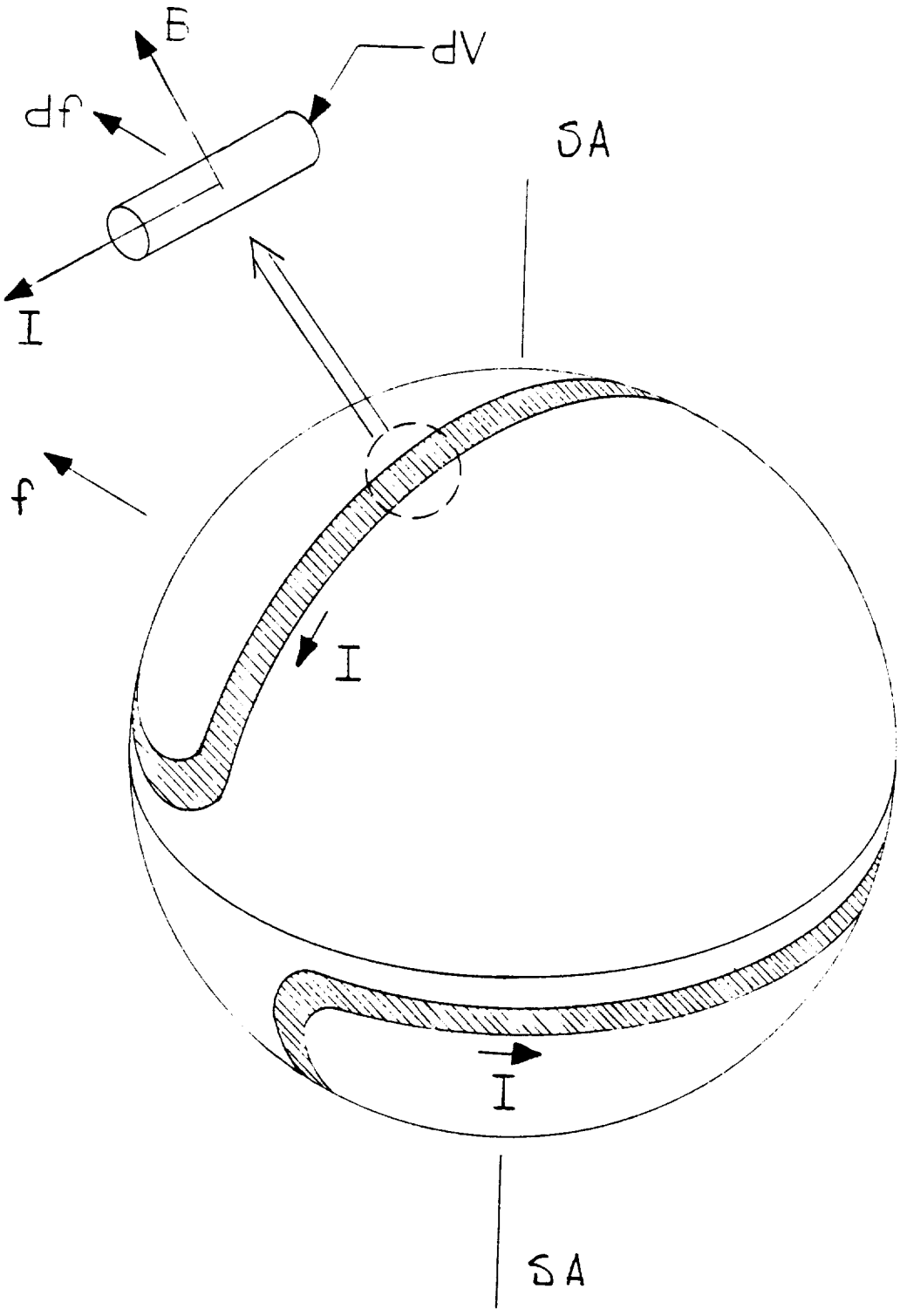

Figure 38. Lateral Force Operation of the Superconducting LAMS

$$\vec{u}_\phi = \cos\phi\cos\theta\ \vec{u}_x + \cos\phi\sin\theta\ \vec{u}_y - \sin\phi\ \vec{u}_z \qquad (6.6)$$

$$\vec{u}_\theta = -\sin\theta\ \vec{u}_x + \cos\theta\ \vec{u}_y$$

These expressions can be substituted into Equations 6.5 in order to provide an expression for the lateral components of the differential force vectors.

$$\vec{df}_1 = \vec{df}_3 = 2\ B_s\ I\ \cos\phi\ \vec{u}_x \qquad (6.7)$$

$$\vec{df}_2 = B_s\ I\ (\cos\theta\ \vec{u}_x + \sin\theta\ \vec{u}_y)$$

The net force (f) produced by the upper lateral-force coil is then found by integrating the differential Lorentz forces around the periphery of the loop. The loop is located on a sphere with radius (R).

$$\vec{f} = B_s\ I\ R\ \left[\ 2 \int_{-\pi/2}^{\pi/2} \cos\phi\ d\phi\ \vec{u}_x + \int_{-\pi/2}^{\pi/2} (\cos\theta\ \vec{u}_x + \sin\theta\ \vec{u}_y)\ d\theta\right] \qquad (6.8)$$

$$= 6\ B_s\ I\ R\ \vec{u}_x$$

The net force is therefore along the x axis. Two additional sets of concentric coils were shown in Figure 36(a). The y-axis coils operate in the same manner as the x-axis coils in order to produce lateral forces along the y-axis. The third set of coils is used to provide lateral radial forces when the spin axis has a large angular displacement from the z-axis (i.e. when z is a lateral axis of the solenoid).

6.2.2.2 Thrust-force Coils. Figure 36(b) showed six additional control coils. These coils are used to apply either thrust forces or torques about the lateral axes. In the discussion which follows, the spin axis of the flywheel is assumed to coincide with the z-axis.

Figure 39 shows the interaction of the current (I) in a coil which is coaxial with the source coil and the magnetic field produced by the source coil. Each differential length (ds) of the coil experiences a differential force (df).

$$\vec{I} = I\,\vec{u}_\theta \tag{6.9}$$

$$\vec{df} = B_S\, I \{ [\, (2\cos^2\phi - \sin^2\phi)\,(\cos\theta\,\vec{u}_x + \sin\theta\,\vec{u}_y)\,] - 3\cos\phi\sin\phi\,\vec{u}_z \} \tag{6.10}$$

The net result of this interaction is a force which acts along the z-axis as shown in Figure 39.

$$\vec{f} = \int_0^{2\pi} \vec{df}\, R\sin\phi\, d\theta = 6\pi\, B_S\, I\, R\cos\phi\sin^2\phi\,\vec{u}_z \tag{6.11}$$

The nominal radius (A) of the control coil can be substituted into this equation to provide an expression for the thrust force as a function of the relative sizes of the control coil and its spacing from the source dipole.

$$A = R\sin\phi \tag{6.12}$$

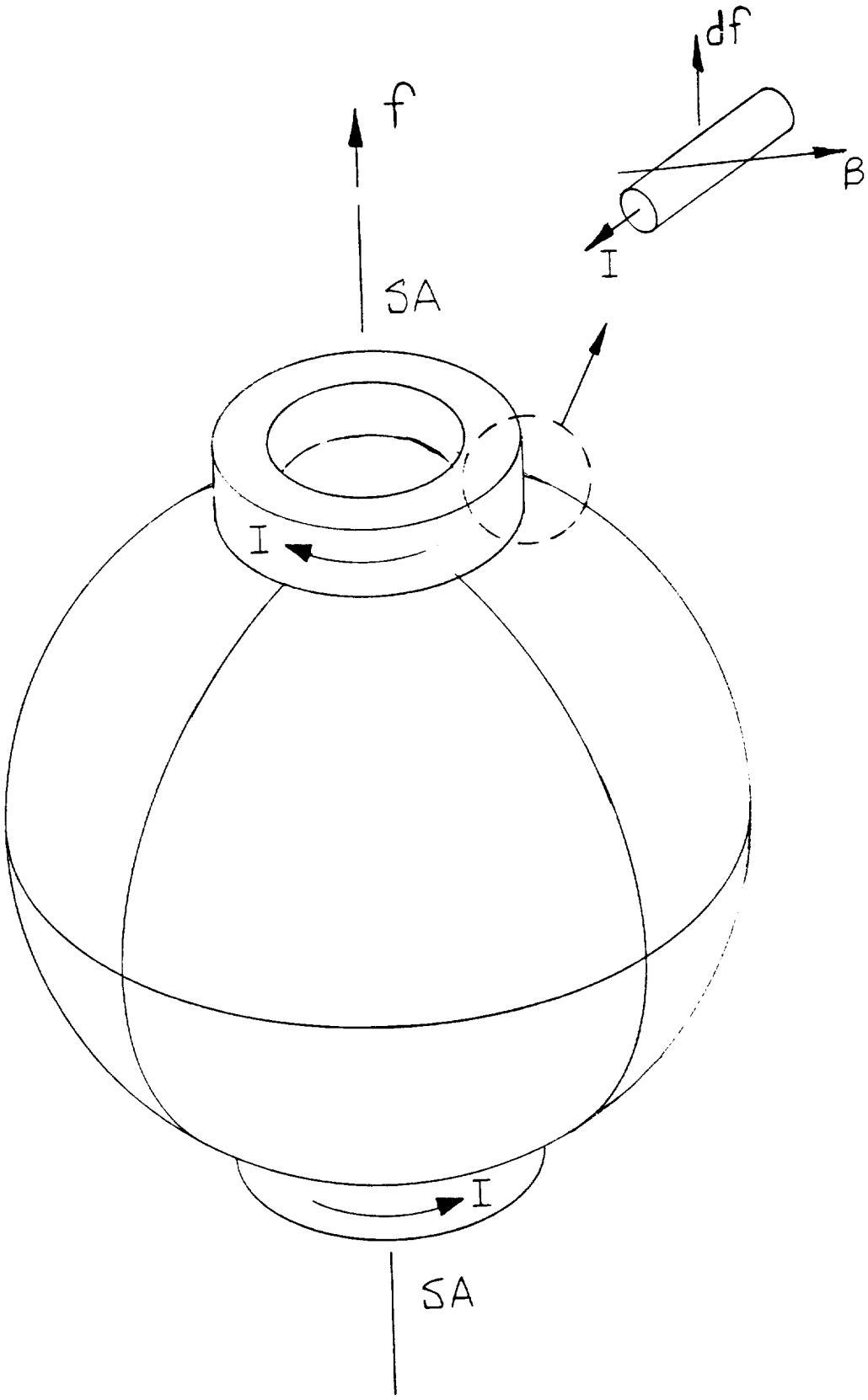

Figure 39. Thrust-force Operation of the Superconducting LAMS

$$\vec{f} = 6\pi\, B_S\, I\, A \left(\frac{A}{R}\right) \left[1 - \left(\frac{A}{R}\right)^2\right]^{1/2} \vec{u}_z \qquad (6.13)$$

6.2.2.3 Torquing Coils. The coils shown in Figure 36(b) which are not coaxial with the spin axis of the flywheel are used to apply torques to the flywheel. Figure 40 illustrates the torquing mechanism. Assuming that the spin axis is along the z-axis, the magnetic field at the location of the torquing coil (B), produced by the superconducting solenoid, is approximately parallel to the z-axis and constant. The torque (τ) results from integrating the moment of the Lorentz force interaction over the volume of the control coil.

$$\vec{\tau} = \iiint \vec{r} \times (\vec{df})\, dV \qquad (6.14)$$

When the flux density is constant, the torque interaction reduces to that of a dipole with moment (m_c). The dipole moment of the coil is related to the total current (I) in the normal coil and the relative geometry of the coil as follows.

$$m_C = \frac{2}{3} \pi \cdot J \cdot (b_C^3 - a_C^3) \cdot L_C \qquad (6.15)$$

$$I = J \cdot (b_C - A_C) \qquad (6.16)$$

$$m_C = \frac{2}{3} \pi \cdot I \cdot (b_C^2 + b_C a_C\, a_C^2) \cdot L_C \qquad (6.17)$$

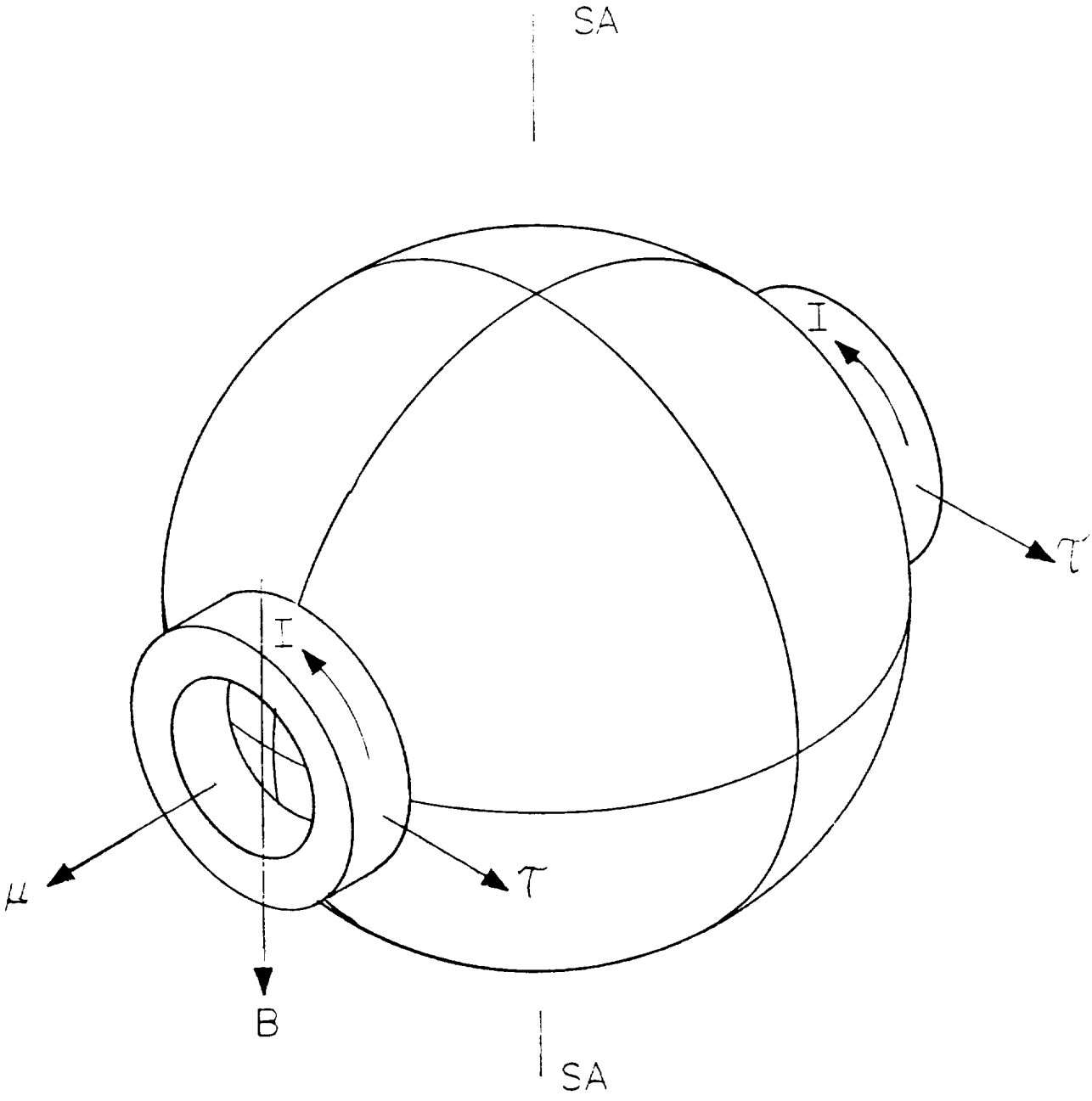

Figure 40. Torquing Operation of the Superconducting LAMS

The torque which results from this interaction is simply calculated from the cross product of the magnetic field produced by the source coil and the dipole moment of the control coil [36].

$$\vec{\tau} = \vec{m}_C \times \vec{B} \qquad (6.18)$$

6.3 Sizing Analysis for the Superconducting LAMS

This section presents a preliminary sizing analysis for the electromagnetic components of the superconducting LAMS. The analysis is based on the requirement that the LAMS produce half of the maximum required control torque (13.5 kNm). This assumes that the torque requirement is not limited by gimballing capability and that a scissored pair of CMGs are used.

6.3.1 Baseline Source Coil

For sizing purposes, a superconducting solenoid design from a previous program [37] was used as the baseline source coil. Table XV presents the dimensions and current density for this solenoid design.

Table XV. Baseline Source Coil

Dimensions	
Inner Radius	12.5 cm
Outer Radius	25.1 cm
Length	33.5 cm
Current Density	96 MA/m^2
Mass	444 kg

6.3.2 Source Field

With the source coil in the nominal orientation, the magnetic field at the location of the torquing coil is purely axial. The magnetic field (B) is parallel to the axis of the source coil and opposite in direction to the field in the bore of the solenoid.

The position of the torquing coil in relation to the source coil is shown in Figure 41(a). The location of the torquing coil is described by the center-to-center distance (R). The axial magnetic field (B) at the location of the torquing coil may then be approximated by the dipole model.

$$B = \frac{\mu_o m_s}{4\pi R^3} \tag{6.19}$$

Figure 41(b) shows the magnetic field predicted by Equation 6.19 and compares this with a more accurate method which considers the superposition of semi-infinite solid solenoids [37].

6.3.3 Torquing Coil Sizing

Each torquing coil must produce half of the torque of the CMG. Each CMG must provide half of the system control torque. The maximum interaction of each torquing coil with the source field must, therefore, produce one quarter of the system requirement.

$$\tau = \frac{1}{4} \tau_m = 6{,}750 \text{ Nm} \tag{6.20}$$

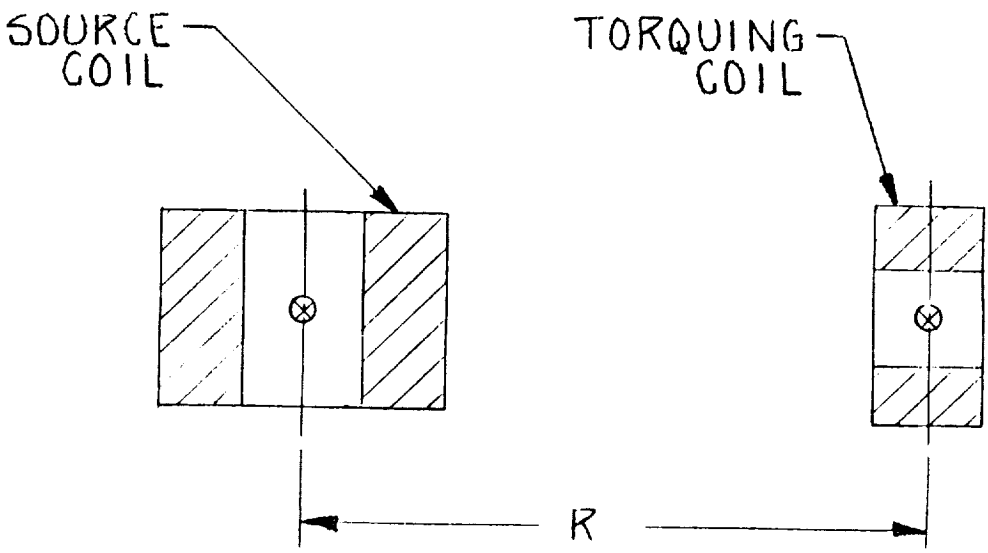

a) Torquing Coil Location

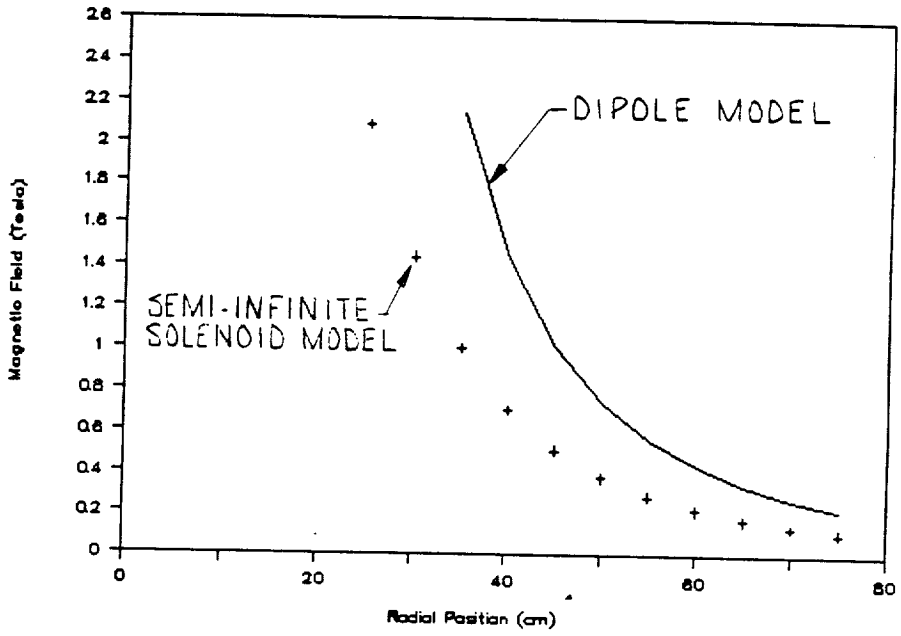

b) Analytical Predictions

Figure 41. Source Axial Magnetic Field

The maximum dipole moment (m_t) which each torquing coil will have to produce is calculated from Equations 6.18 and 6.20.

$$m_t = \frac{\tau_m}{4B} \tag{6.21}$$

Figure 42 shows this required dipole moment as a function of the position of the torquing coil. The semii-infinite-solenoid magnetic field model was used.

Given radial and axial aspect ratios (α_c and β_c), the inner radius (a_c), outer radius (b_c), and length (L_c) of the torquing coil can be determined.

$$a_c^4 = \frac{3\ m_t}{2\pi(\alpha_c^3 - 1)\beta_c \eta_w J_c} \tag{6.22}$$

$$b_c = \alpha_c \cdot a_c \tag{6.23}$$

$$L_c = 2 \cdot \beta_c \cdot a_c \tag{6.24}$$

Figure 43 shows these dimensions as a function of the coil location (R). A 71% fill factor (η_w) was assumed. The conductor current density (J_c) was set to be consistant with uncooled copper wire (4 MA/m^2). Radial (α_c) and axial (β_c) aspect ratios of 1.5 and 0.1 were assumed.

The mass of a control coil (M_c) is readily calculated from the dimensions and the density (ρ_c) of the conductor material and the volume (V_c) of the coil.

$$M_c = \rho_c \cdot \eta_w \cdot \pi \cdot (b_c^2 - a_c^2) \cdot L_c = \rho_c \cdot V_c \tag{6.25}$$

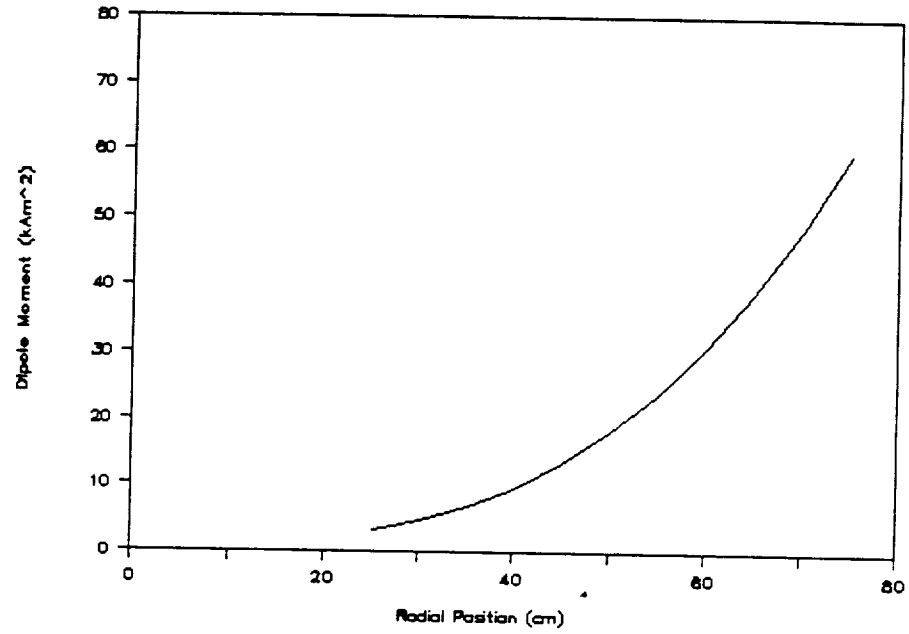

Figure 42. Required Dipole Moment of the Torquing Coil

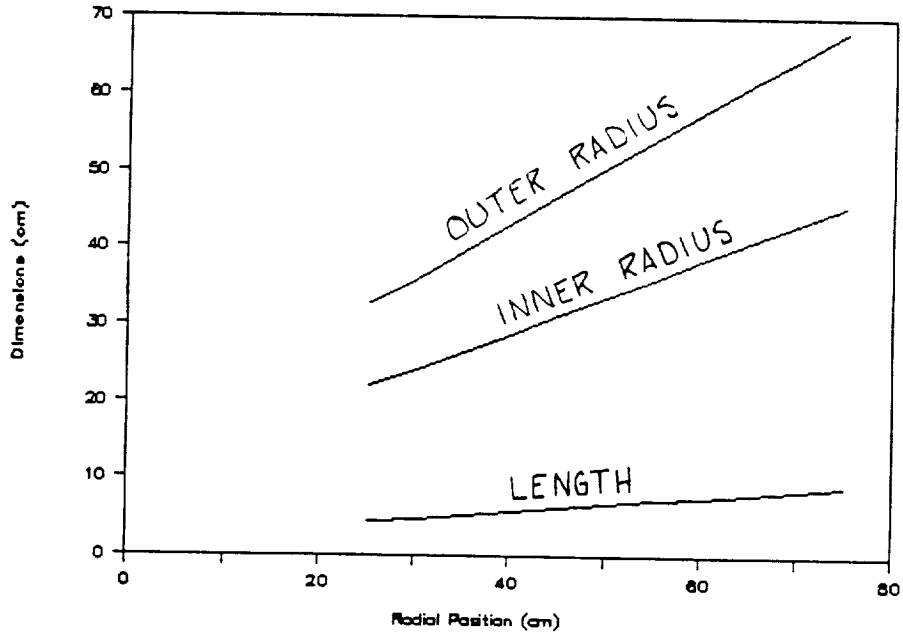

Figure 43. Dimensions of a Torquing Coil

The mass of a torquing coil is shown in Figure 44 as a function of coil position.

The amount of power (P) consumed in ohmic heating of the torquing coil is determined by the conductivity (σ_C) of the torquing coil.

$$P = \frac{J_C^2 \cdot V_C}{\sigma_C} \qquad (6.26)$$

Figure 45 shows the ohmic losses in a torquing coil as a function of the coil position. Both room temperature (300 degrees Kelvin) and cryoresistive (77 degrees Kelvin) copper coils were considered.

6.3.4 Baseline Superconducting LAMS

Table XVI presents a baseline design for the torquing coils of the superconducting LAMS. This design represents the minimum separation between the source and torquing coils. The dimensions and performance were interpolated from the data presented in Figures 42 through 45.

Table XVI. Characteristics of the Baseline Torquing Coil

Dimensions	
Inner Radius	25.2 cm
Outer Radius	37.7 cm
Length	5.03 cm
Mass	79 kg

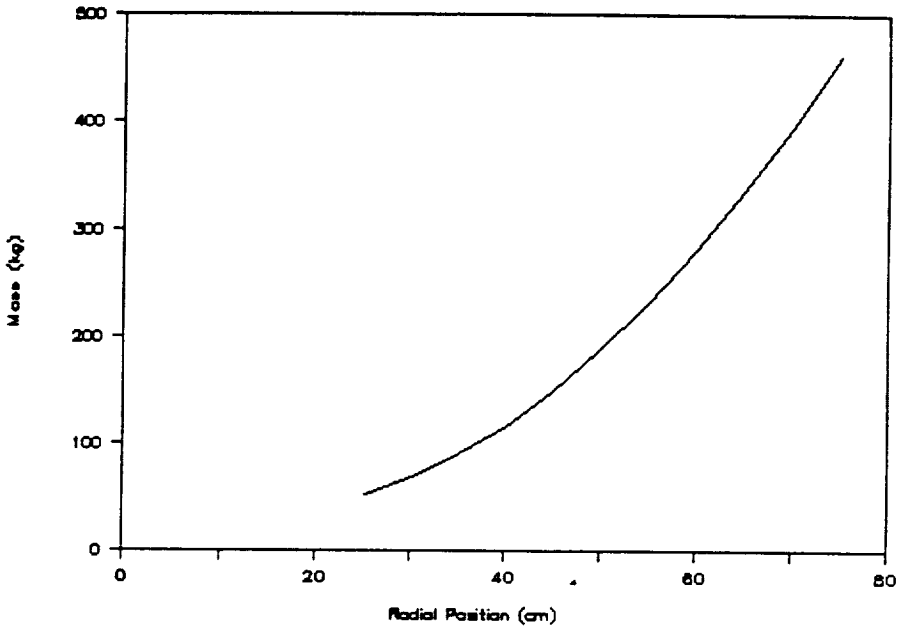

Figure 44. Mass of a Torquing Coil

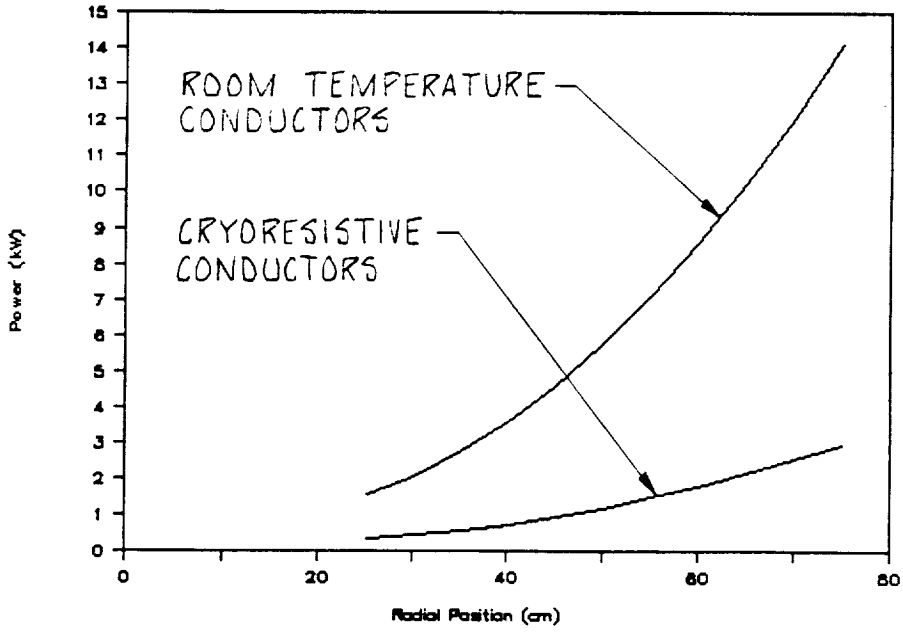

Figure 45. Power Consumption of a Torquing Coil

During torquing, the coil described in Table XVI would consume approximately 2,400 Watts at 300 degrees Kelvin and 500 Watts at 77 degrees Kelvin. Since two torquing coils provide the same excitation on each CMG, the total power consumption will be twice these numbers.

The total performance numbers (mass and power consumption) for an advanced-concept CMG are derived from the results presented in Table XVI. Six torquing/thrust-force coils are required as shown in Figure 36(b). Each of these coils will be identical to those described in Table XVI. Since the loads on the lateral-force coils described in Figure 36(a) will be small in space, the total mass of these coils was assumed to be equal to that of a single torquing coil. The mass tabulation and power requirements of each CMG are presented in Table XVII.

Table XVII. Superconducting LAMS Performance

Mass	Each	Total
Source Coil (1)	444 kg	444 kg
Lateral-force Coils (6)	13 kg	79 kg
Torquing/thrust-force Coils (6)	79 kg	474 kg
Total Mass		997 kg
Power Consumption		
300 degrees Kelvin		4,800 W
77 degrees Kelvin		1,000 W

7. SPIN MOTOR

The selection of the type and configuration for the spin motor of the advanced-concept CMG is dictated by two of the characteristics of the application. First, since the CMG will be magnetically suspended, any side-load introduced by the spin motor will impact the suspension controller. Side-load is present in any machine with magnetic iron on both the rotor and stator because a reduction in air-gap will reduce the system energy. This "unstable-spring" effect leads to minimum requirements for both bandwidth and gain of the magnetic suspension, impacting the controller design.

The second characteristic of this application which impacts the spin motor is the presence of extremely high magnetic fields due to the superconducting source coil (11 Tesla in the bore of the solenoid). This attribute has a direct effect on the use of both soft iron and permanent magnets. The presence of soft magnetic iron has no benefit in an area where the ambient field would drive it far into the region of magnetic saturation. Permanent magnets located in a field strength greater than their coercivity will simply remagnetize in the direction of that field. Thus, the techniques of conventional machine design must be re-examined in light of the high ambient flux density.

The remainder of this chapter presents the various machine types, both conventional and unconventional, which appear to have applicability as the spin motor for the CMG. In-depth analysis

of these configurations is beyond the scope of this program; such analysis and development of a candidate prototype will be required as the development of the CMG itself progresses. As such, the following is a description of both the operating principle of each machine, and the characteristics which make it potentially suitable for this application.

7.1 Candidate Machines

A list of the machine types which may have applicability as the spin motor for the CMG is shown in Table XVIII along with their qualitative attributes. Each machine is discussed in detail below.

Table XVIII. Machine Candidates

Type	Advantages	Disadvantages
Homopolar	Uses large bore field.	Requires brushes.
Induction	Rotor iron not required. No side-load.	Losses in cryostat.
Reluctance	Requires magnetic iron on rotor.	Losses in cryostat.
Electrostatic	Uses electric rather than magnetic fields.	Poor power density at reasonable voltages.

7.1.1 Homopolar

This machine is believed to be the only type which can make use of the large uniform magnetic field in the bore. It consists of a conductive disk to which a current is supplied such that there is a uniform radial current density (J) as shown in Figure 46. The interaction of the radial current density with the

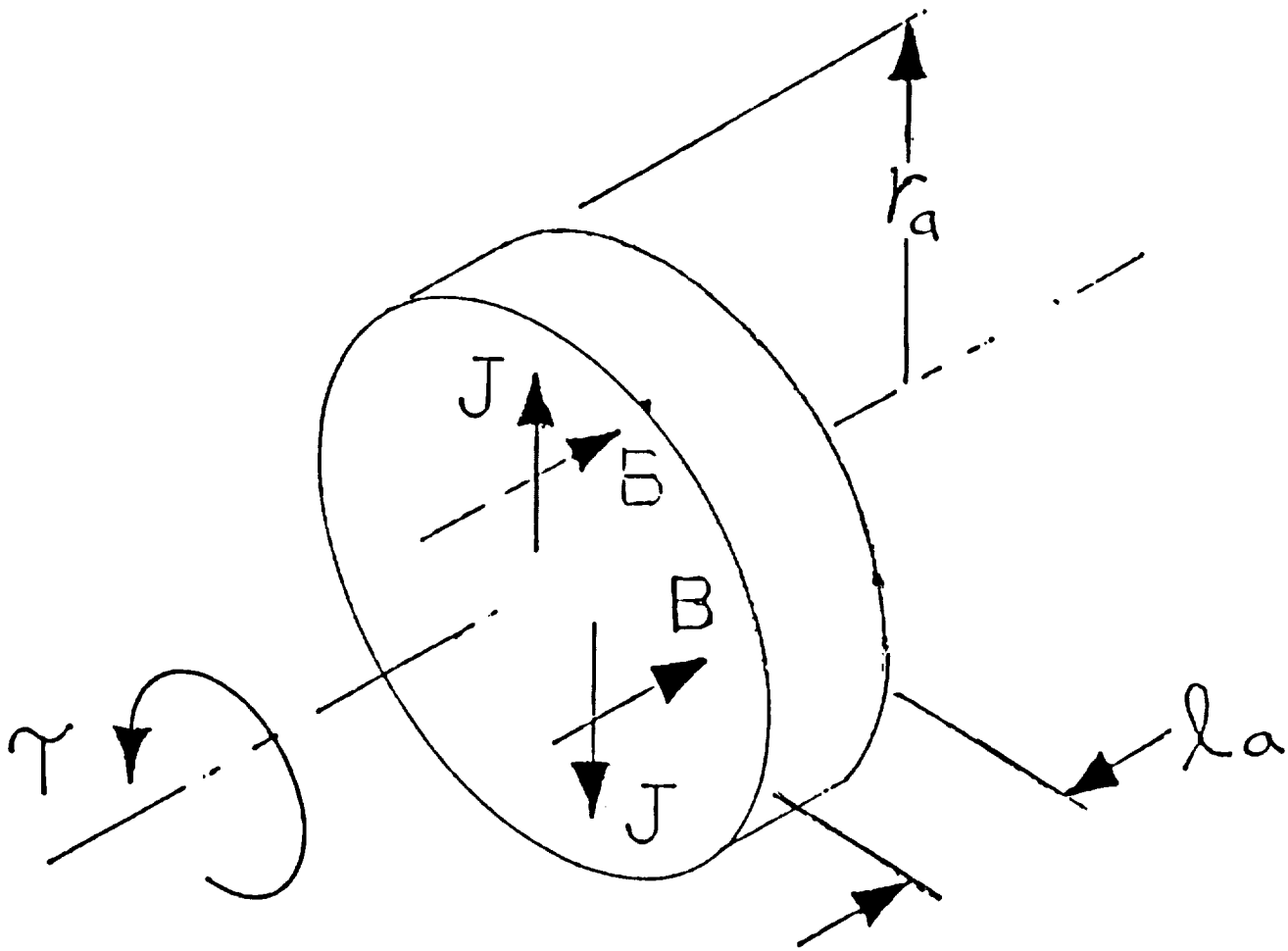

Figure 46. Homopolar Spin Motor

uniform magnetic field in the bore (B) will produce a torque

$$\tau = \iiint r \times (J \times B_z)\, dV$$

$$= \frac{2}{3} J\, B_z\, r_a\, V_a$$

where r_a and V_a are the radius and volume respectively of the disk. Unfortunately, since the reaction torque is produced, not on the superconducting solenoid, but on the circuit which supplies the current, operation of this device as a motor requires brushes for current transfer to the disk. This would place severe design constraints on both the magnetic suspension and the brushes themselves.

7.1.2 Induction

The induction machine operates on the principle of the reaction between induced currents in the rotor and the magnetic field in the air-gap. It typically consists of a wound rotor and a stator core made up of laminations carrying slot-embedded conductors (armature windings). Alternating current is supplied to the stator windings to create a rotating magnetic field in the air-gap. This magnetic field induces currents in the rotor conductors which react with the magnetic field to produce torque. Resistive losses occur in both the rotor and stator, which is a disadvantage since the rotor conductors would be inside the cryostat. The advantage of this machine type is that the rotor does not require the use of magnetic iron in the high-field

region near the superconducting solenoid. In the advanced-concept CMG a squirrel-cage could be incorporated into the design of the composite-material flywheel. A concept sketch of an induction spin motor is shown in Figure 47.

7.1.3 Reluctance

The reluctance machine employs the tendency of ferromagnetic materials to align in the presence of a magnetic field. The rotor typically consists of salient poles while the stator contains permanent magnets and/or armature windings to induce a magnetic field in the air-gap. Losses on the rotor are only those due to soft iron, i.e., hysteresis and eddy-current losses. This is somewhat disadvantageous in this application since the rotor losses occur inside the cryostat, but they should be minimal. The disadvantage of this machine type is the need for magnetic iron on the rotor in the vicinity of the large magnetic fields produced by the source coil. However, preliminary analysis of the magnetic field at the edge of composite flywheel indicates that its magnitude could be significantly below the saturation flux density of high-performance soft-irons such as vanadium permendur. As long as the iron is not heavily saturated, it can be utilized in the variable reluctance design required for this machine. Figure 48 shows the construction of the rotor of a reluctance spin motor. Soft-iron pole pieces are imbedded in the composite material. The stator is identical to that of the induction spin motor.

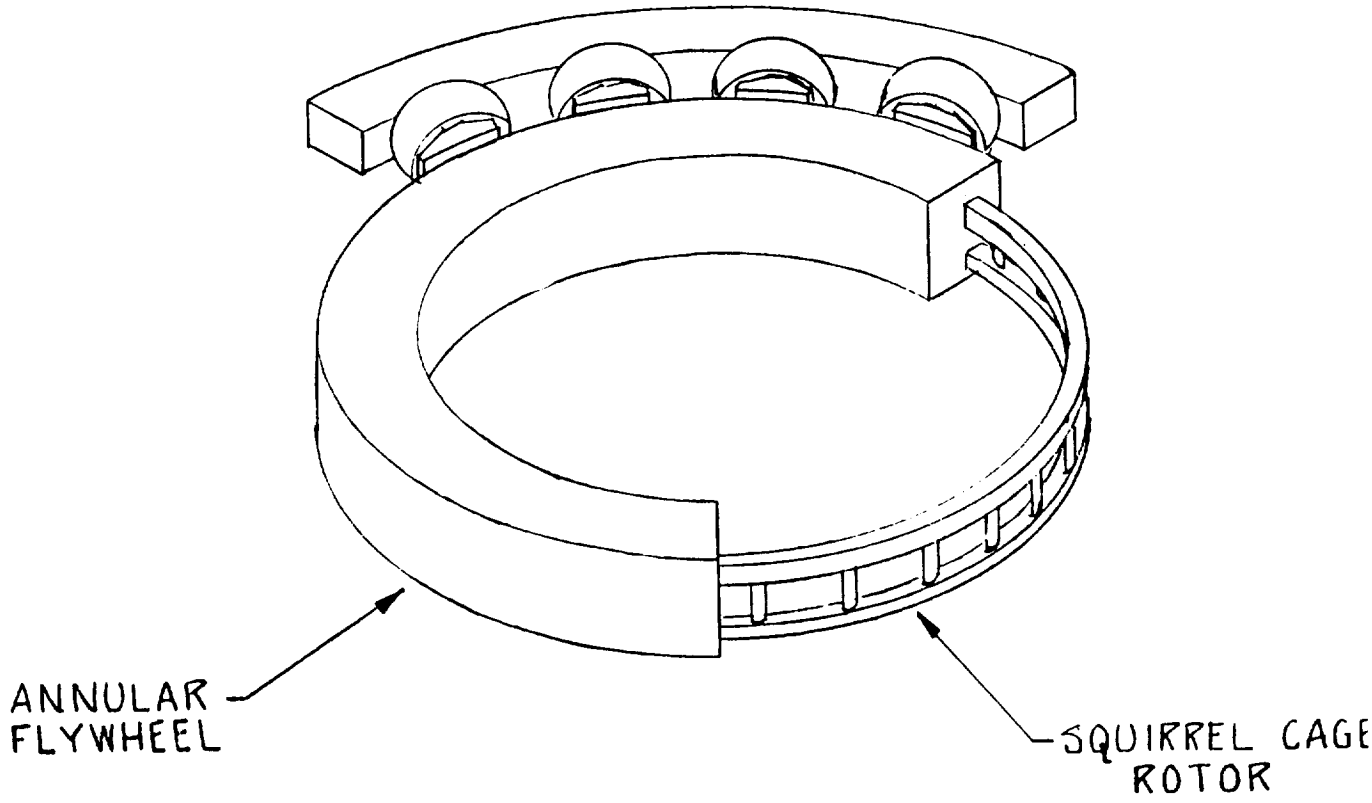

Figure 47. Induction Spin Motor

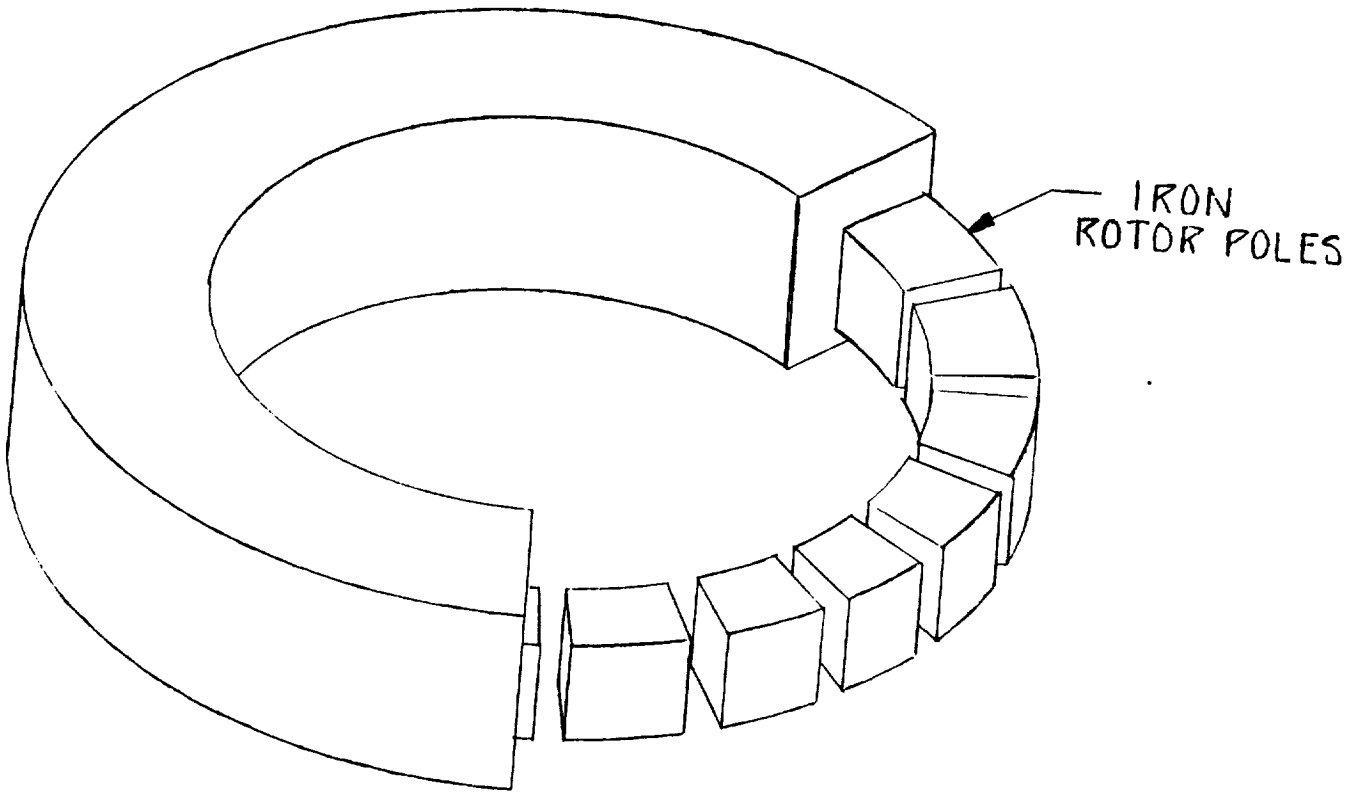

Figure 48. Reluctance Spin Motor

7.1.4 Electrostatic

The electrostatic machine operates on a principle analogous to the reluctance machine using electric fields and variable capacitance, i.e., the tendency of capacitive plates to align in the presence of an electric field. Since this process uses no soft iron and is insensitive to magnetic fields, it may be the ideal candidate for the CMG spin motor. However, given the practical limits on both voltage (dielectric breakdown) and capacitance (plate area), electrostatic torque is significantly weaker than reluctance torque for comparable machine dimensions. This would probably restrict the electrostatic machine to use as a constant-speed device, making up only for rotational losses of the CMG rather than as a power transfer device. Figure 49 shows a sketch of an electrostatic spin motor.

7.2 Spin Motor Summary

This chapter has qualitatively surveyed the potential candidates for the spin motor of the advanced-concept CMG. Of these, induction and reluctance machines are the only acceptable candidates if a constant-energy array is employed. Of these, the reluctance machine is the preferred choice based on reduced losses in the cryostat. If, however, a spin motor is required to only maintain the speed of the rotor, then an electrostatic machine would be used.

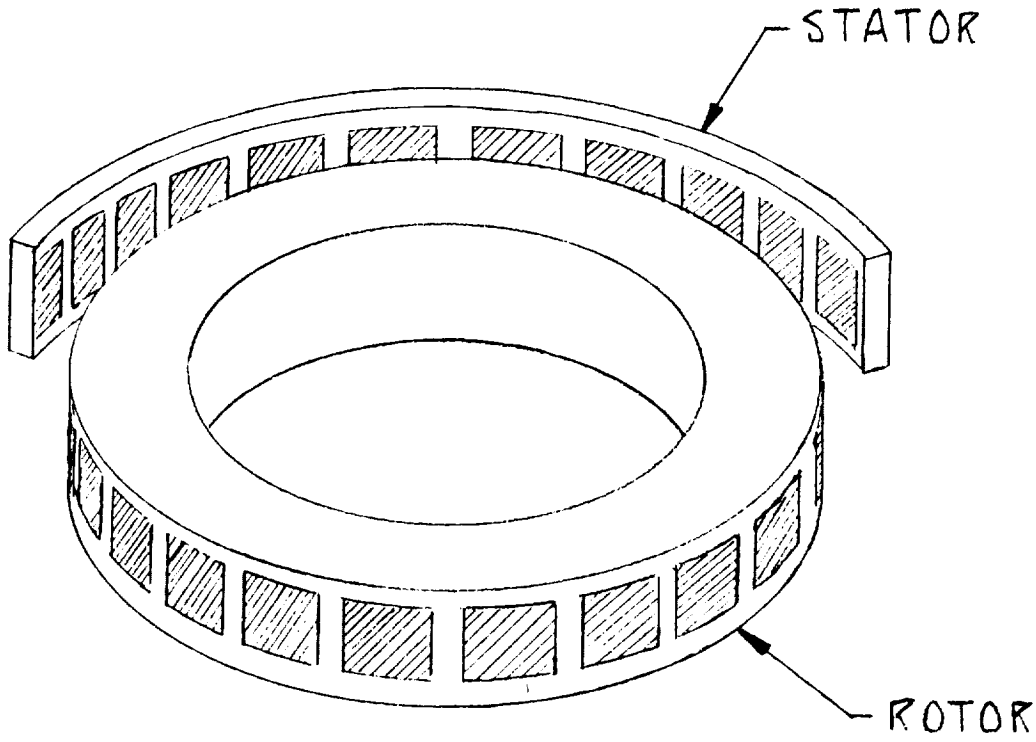

Figure 49. Electrostatic Spin Motor

8. CONCLUSIONS AND RECOMMENDATIONS

This report has described an advanced-concept CMG which could be used in a high-torque slew actuator for large space-based payloads. The advanced-concept design was motivated by deficiences in available component technologies which limit the performance of a CMG. As described in Chapters 3, 4, and 5, the use of conventional approaches to CMG construction produces a design which is excessively massive and consumes an inordinate amount of power.

The CMG employs several advanced component technologies in order to achieve performance that exceeds that which could be achieved through conventional approaches. These individual component technologies consist of magnetic bearings, a fiber composite flywheel, and a superconducting magnet. Although a magnetically-suspended rotating structure which consists of a superconducting magnet and a graphite/ epoxy flywheel is novel, each of the individual components is approaching the status of an available technology.

Magnetic bearings are clearly becoming a conventional technology. This can be easily seen by the amount of interest in this technology for Earth-based industrial as well as space-based applications. A recent flight demonstration of a magnetically-suspended reaction wheel has clearly demonstrated that this technology is near-term [4].

Superconducting magnets have been a basic tool for experimental research in physics for many years. The medical research community is currently employing superconducting magnets for magnetic resonance imaging (MRI). Recent advances in "high-temperature" superconducting materials have prompted many engineers to consider the use of this emerging technology in other applications. Superconducting materials could have a substantial impact on the design of magnetic bearings. This study suggests that a superconducting magnetic bearing could be applied in an application where flux saturation in conventional core materials either requires that a large magnetic structure be employed, or that the magnetic bearing consume a great deal of electrical power.

Graphite/epoxy composite materials are widely used in the aerospace industry for weight-sensitive, high-load components. The government has funded the design and fabrication of a large number of composite flywheel rotors including graphite/epoxy. This program was directed toward the development of energy storage flywheels, but the use of these rotors in angular momentum exchange actuators has also been considered.

8.1 Design Summary

Table XIX tabulates the masses of the magnetic components of an advanced-concept CMG. The mass of the LAMS is obtained from Table XVII. The mass of the graphite/epoxy flywheel ignores the contribution of the superconducting magnet to the total angular

Table XIX. Mass Tabulation for the Advanced-concept CMG

Superconducting LAMS	997 kg
Graphite/epoxy Flywheel	25 kg
Spin Motor	5 kg
Total	1,227 kg

momentum of the rotating assembly. The mass of the spin motor assumes that a homopolar machine has been employed. The mass of a homopolar machine is intermediate between those of an electrostatic machine and an induction or reluctance machine. Since the mass of the superconducting LAMS clearly dominates the system mass, these approximations are probably adequate.

The power consumed in ohmic heating of the normal torquing coils and the mechanical power delivered to the payload provide the conversion efficiency of the process. Table XX tabulates the efficiencies of room-temperature resistive and cryoresistive control coils as well as the continuous power of the slew actuator configured as a constant-energy array.

Table XX. Slew Actuator Power Consumption

	Coil Temperature (degrees Kelvin)	
	300	77
LAMS Power Consumption (W)	9,600	2,000
Mechanical Power (W)	9,400	9,400
Efficiency (%)	49.5	82.4
Continuous Power Input (W)	7,250	1,100

Cooling of the control coils to the temperature of boiling liquid nitrogen clearly has advantages in terms of reduced power

consumption for the LAMS. The use of a constant-energy array will further reduce the power requirement from the prime power source of the spacecraft.

8.2 Technology Development Needs

In order for the advanced-concept CMG to be demonstrated, a number of technical issues in the design of the system will have to be addressed. These issues deal with optimum component selection, as well as with specific technical questions related to the mechanical, magnetic, and controller design for the LAMS.

8.2.1 Optimum Component Selection

The selection of a baseline spin motor type was discussed as an unresolved issue in Chapter 7. In addition, the position of the rotor will have to be monitored by an array of sensors. The selection of either of these two components will impact the other. One possible approach to position sensing is a set of opposed capacitive plates on the rotor and stator. If, however, an electrostatic spin motor is used, then a capacitive sensor is probably not practical due to coupling. A capacitive position sensor would probably be the preferred choice if an induction or reluctance spin motor is employed.

8.2.2 Mechanical Design Challenges

The rotor and stator of the LAMS present several novel mechanical design challenges. The design of the source coil will be limited by a combination of rotational stresses and magnetically-induced stresses [32]. The fluid mechanic and

thermodynamic characteristics of high-speed rotation in a cryogenic fluid are also an area which poses design challenges. The mechanical properties of the flywheel material at cryogenic temperatures will have to be determined.

The design challenge for the stator of the LAMS deals with heat transfer into the cryostat. As discussed in Chapter 6, the fact that the superconducting magnet is supported without contact simplifies the thermal design of the cryostat. The use of normal resistive coils in the liquid nitrogen jacket, however, will increase the heat removal requirement for the refrigeration system.

8.2.3 Magnetic Design Challenges

A LAMS is a large scale applications of magnet technology, quite similar in certain ways to a synchronous machine. They require substantial flux density over relatively large volumes of space to have satisfactory force density. Superconductors, which offer large magnetomotive forces and high flux density, appear to be desirable in these situations. Flux densities substantially in excess of those possible with iron can be produced, and no ferromagnetic material is required.

The most common superconducting material in use today is niobium titanium. This is a strong, ductile material which is commonly fabricated into composite conductors with pure copper or mixed copper alloy matrices. At the boiling point temperature of liquid helium (4 degrees Kelvin) critical current and flux densities are on the order of 100 MA/m^2 and 5 Tesla respectively.

The less-commonly used niobium-tin material will maintain a superconducting state up to a critical flux density of about 12 Tesla. This material, however, is extremely brittle and therefore much more difficult to fabricate into coils than niobium titanium. Extremely high performance is available from niobium germanium aluminum superconductors. This material has a critical temperature which is slightly greater than 20 degrees Kelvin, but it is virtually impossible to fabricate into wire.

The principal difficulty in using available superconductors is, of course, the deep cryogenic temperatures at which they must operate. Because it takes several hundred Watts of refrigerator input power to remove one Watt of thermal dissipation of heat leak from a space operating at the temperature of boiling liquid helium, the use of superconductors operating at that temperature is impractical for all but the most demanding applications. These applications always involve high vacuum systems, thermal radiation shields and transfer piping which is complicated. Liquid helium systems are vulnerable to contamination because all other substances are solid at such low temperatures.

Because of these difficulties, the possibility of superconductors which can be operated in liquid nitrogen is thought to extend the number and range of applications of superconductivity. Critical temperatures of about 98 degrees Kelvin have been demonstrated in a class of materials which are, in fact, ceramics. A large amount of public attention has been attracted to these new materials.

The promise of higher operating temperatures is tempered by the relatively low useful current densities which have been demonstrated and by the nature of the materials themselves. In order to be useful, superconductors must be capable of carrying substantial currents in the presence of large magnetic fields.

Being ceramics, they are brittle and difficult to form into useful conductors. In addition, the class of materials which has been demonstrated is highly reactive, sensitive to water, and difficult to make connections to. Low performance but high temperature superconductors do not seem to be applicable here.

8.2.4 Controller Design Challenges

Controller design is typically the key to a successful magnetic suspension system. Designing the controller for a superconducting LAMS is complicated by the highly non-linear nature of the plant. Generating adequate system models will be difficult since conventional small-air-gap approximations will not be valid. The plant dynamics will depend heavily on the orientation of the source coil, leading to a computational-intensive design process and the use of a scheduled gain controller.

8.3 Recommendations

In order to address the remaining technical issues and to provide an affordable, yet conclusive, demonstration of the feasibility of this actuator concept, a series of small-scale component experiments should be performed. Initially, a

commercially available persistant-mode superconducting magnet could be used to suspend relative to a fixed array of control coils to demonstrate the control concepts and sensor technology. An intermediate result would be an improvement of analytical tools and verification of them. As a second step, the self-contained persistent mode coil would be replaced by a free-standing coil in a specially designed cryostat.

In parallel with these efforts, a research program directed toward optimizing the overall design of the CMG should be initiated. The goal of this effort would be to finalize the mechanical, magnetic, and thermal design of the system components. This would include the incorporation of the spin motor in the rotating structure and the identification of alternative control coil geometries, possibly including the use of the bore of the superconducting coil. Early emphasis on the thermal design of the cryostat would allow technology to be transferred to the controls demonstration experiment.

The controls demonstration would finally be upgraded to include a rotating assembly. This would follow subscale component tests of the rotor components.

The advanced-concept CMG appears to be a unique extension to magnetic bearing and suspension technology which will lead to a revision of conventional design practices. The elimination of soft-iron will allow many previously impossible design innovations to be considered. Further research in this area is strongly recommended.

REFERENCES

1. "Model 4500 CMG", CMGs and Momentum Wheels, Sperry Flight Systems, pp. 6.0-6.5.

2. Control Moment Gyros, Sperry Flight Systems, 1982.

3. Components for Space Applications, Teldix G.M.B.H., Heidelberg, April 1978, pp 26-29.

4. Gauthier, M. and J. Roland: "An Advanced and Low Cost 2 Degrees of Freedom Magnetic Bearing Flywheel," Proceedings of the 22nd Intersociety Energy Conversion Engineering Conference, Philadelphia, PA, pp. 846-851.

5. Downer, J.: Design of Large-Angle, Magnetic Suspensions, ScD Thesis, Massachusetts Institute of Technology, May 1986.

6. Strunce, R.: An Investigation of Enabling Technologies for Large Precision Space Systems, The Charles Stark Draper Laboratory, Inc., R-1499, Vol. 1, Prepared for DARPA under Contract No. F30602-81-C-0180, November 1981.

7. Breakwell, J.: "Optimal Feedback Slewing of Flexible Spacecraft," AIAA Journal of Guidance and Control, Vol. 4, No. 5, Sept-Oct 1981, pp. 472-479.

8. Roberson, R.: "Principles of Inertial Control of Satellite Attitude", Proceedings of the 9th International Congress of Astronautics, Amsterdam, Holland, August 1958.

9. Wertz, J.: Spacecraft Attitude Determination and Control, P. Reidel Publishing Co., 1978.

10. Kennel, H.: "A Control Law for Double-Gimbaled Control Moment Gyros Used for Space Vehicle Attitude Control," NASA TM X-64536, August 1970.

11. Gross, S.: "Study of Flywheel Energy Storage for Space Stations," NASA CR-171780, February 1984.

12. Oglevie, R. and D. Eisenhaure: Advanced Integrated Power and Attitude Control System (IPACS) Study, NASA CR-3912, November 1985.

13. Chang, G. (Editor): 1977 Flywheel Technology Symposium, San Francisco, CA, The U.S. Department of Energy, October 1977.

14. Barlow, T. (Editor): 1980 Flywheel Technology Symposium, Scottsdale, AZ, The American Society of Mechanical Engineers, October 1980.

15. Kulkarni, S.: "Flywheel Rotor and Containment Technology Development Program of the U.S. Department of Energy", presented at the Third International Conference on Composite Materials, 1980.

16. Keckler, C., G. Rodrigues, and N. Groom: Integrated Flywheel Technology 1983, NASA CP-2290, August 1984.

17. Keckler, C., R. Becktel, and N. Groom: An Assessment of Integrated Flywheel System Technology, NASA CP-2346, February 1984.

18. Olszewski, M., and D. O'Kain: "Advances in Flywheel Technology for Space Power Applications," Proceedings of the 21st Intersociety Energy Conversion Engineering Conference, San Diego, CA, August 1986.

19. Timoshenko, S.: Strength of Materials, Part II - Advanced Theory and Problems, Krieger Publishing Co., 1976

20. Anderson, W. and Groom, N.: "The Annular Momentum Control Device (AMCD) and Potential Applications," NASA TN-D 7866, 1975.

21. Eisenhaure, D., J. Downer, T. Bliamptis, and S. Hendrie: "A Combined Attitude, Reference, and Energy Storage System for Satellite Applications," AIAA-84-0565, Presented at the 22nd Aerospace Sciences Meeting, Reno, NV, January 1984.

22. Sindlinger, R.: "Magnetic Bearing Momentum Wheels with Magnetic Gimballing Capability for 3-Axis Active Attitude Control and Energy Storage," Conference on Attitude and Orbit Control Systems, ESA SP-128, Noordwijk, November 1977.

23. Murakami, C.: "Development Activities on Magnetic Bearings for Space Use in National Aerospace Laboratory of Japan," Proceedings of the Sixth International Workshop on Rare Earth Cobalt Permanent Magnets, Vienna, Aug.-Sept. 1982.

24. "Magnetic Bearing Momentum Wheel, Type MDR," Components for Space Applications, Teldix G.M.B.H., Heidelberg, April 1978, p. 26.

25. Magnetic Bearing Momentum Wheel, Type MSR," Components for Space Applications, Teldix G.M.B.H., Heidelberg, April 1978, p. 28.

26. Hendrickson, C., J. Lyman, and P. Studer: "Magnetically Suspended Momentum Wheels for Spacecraft Stabilization," Presented at the 12th AIAA Aerospace Sciences Meeting, January 1974.

27. Groom, N. and J. Miller: "A Microprocessor-Based Table Look-up Approach for Magnetic Bearing Linearization," NASA TP-1838, May 1981.

28. Oglevie, R. and D. Eisenhaure: "Integrated Power and Attitude Systems for Space Station," AIAA-85-0358, Jan. 1985.

29. Oglevie, R.: "Wheel Configurations for Combined Energy Storage and Attitude Control Systems," Presented at the AIAA Guidance and Control Conference, Snowmass, CO, August, 1985.

30. Anderson, W. and C. Keckler: "An Integrated Power/Attitude Control System (IPACS) for Space Vehicle Application," presented at the Fifth IFAC Symposium on Automatic Control in Space, Genoa, Italy, June 1973.

31. Parker, R. and R. Studders: Permanent Magnets and their Applications, John Wiley & Sons, Inc., 1962.

32. Wilson, M.: Superconducting Magnets, Clarendon Press, 1983.

33. Reed, R. and A. Clark, Editors: Materials at Low Temperatures, American Society for Metals, 1983.

34. Lorrain, P. and D. Corson: Electromagnetic Fields and Waves, Chapter 7, W. H. Freeman and Co., 1970.

35. Hildebrand, F.: Advanced Calculus for Applications, Prentice Hall, Inc., 1976.

36. Schwartz, M.: Principles of Electrodynamics, Chapter 4, McGraw-Hill Book Co., 1972.

37. Johnson, B. and R. Hockney: "Superconducting Linear Actuator", Magnetic Suspension Technology Workshop, (NASA LaRC, Hampton, Virginia), February 1988.

38. Wrigley, W., W. Hollister, and W. Denhard: Gyroscopic Theory, Design and Instrumentation, The MIT Press, 1969.

39. Jones, R.: Mechanics of Composite Materials, McGraw-Hill Book Co., 1975.

APPENDIX A SLEW MANEUVER DYNAMICS

This appendix presents a series of dynamic analyses which aid in the design definition for the slew actuator. A rapid slew is a dynamic maneuver which is amenable to closed form analysis. This appendix analyzes the rigid body kinematics of the payload, the gyroscopic coupling of a CMG slew actuator, and the transient requirements for the slew actuator power supply. The results of these analyses are employed in Chapters 2 and 3 to provide guidance for the sizing of the slew actuator.

A.1 Rotational Kinematics and Dynamics of the Maneuver

This section presents an example of the calculations which were used to determine the torque, angular momentum storage, and power handling capabilities which are required of an actuator for slewing a large space-based payload. The payload is modelled as a rigid body which has a specified moment of inertia about the axis of rotation. It is assumed that the payload must be reoriented through a specified angle in a specified time period.

A.1.1 Torque and Acceleration Profiles

Figure 50(a) shows the torque applied by the actuator to the payload, which has a moment of inertia (I_S) about the axis of the slew. A constant positive torque (τ_C) accelerates the payload for one half of the slew period ($0 < t < T_S/2$). A constant negative torque with the same magnitude then decelerates the payload for the remainder of the maneuver ($T_S/2 < t < T_S$). The

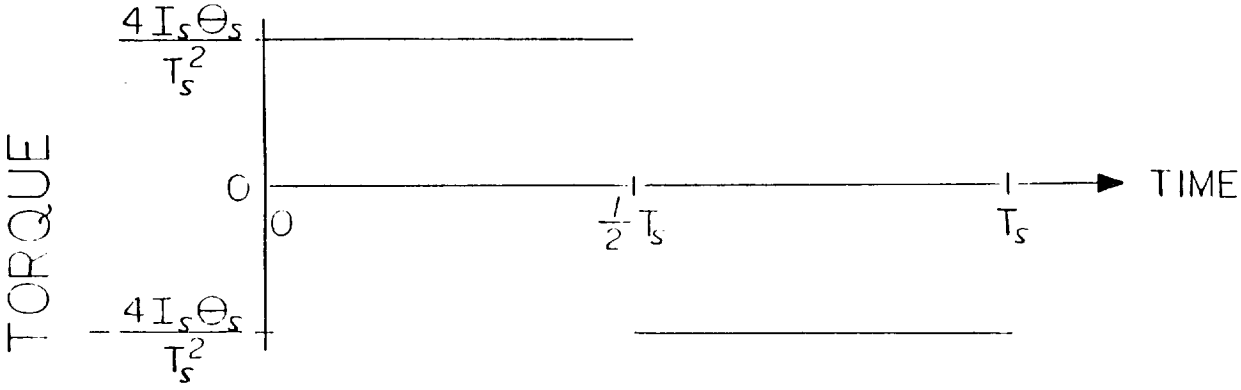

a) Torque

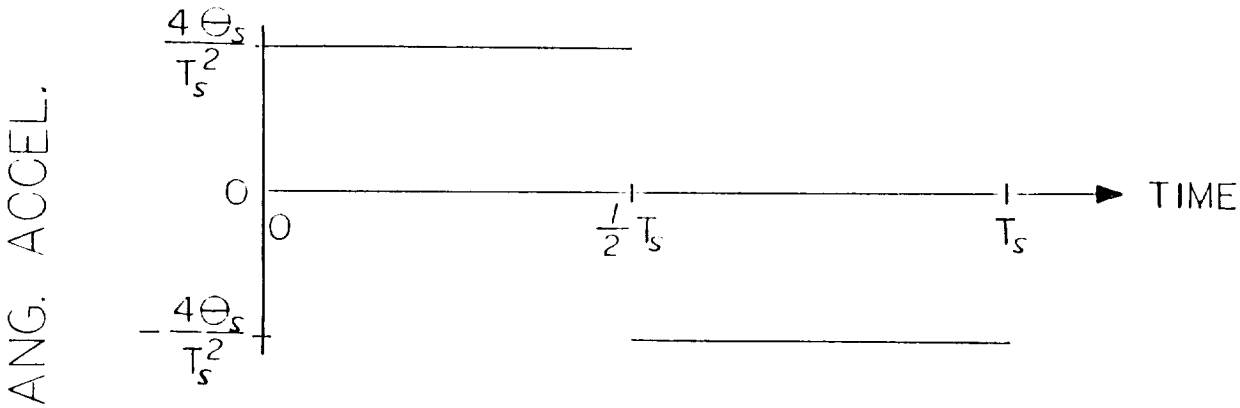

b) Angular Acceleration

Figure 50. Torque and Acceleration Profiles

resulting angular acceleration (α) profile of the payload is calculated from Newton's law for rotation (simplified for single-axis rotation). Equation A.1 below assumes that no external torques other than the control torques act on the payload.

$$\tau(t) = I_S \cdot \alpha(t) \tag{A.1}$$

Figure 50(b) shows the resulting payload acceleration.

(acceleration)
$$\alpha(t) = \frac{\tau_C}{I_S} \tag{A.2a}$$

(deceleration)
$$\alpha(t) = -\frac{\tau_C}{I_S} \tag{A.2b}$$

A.1.2 Angular Momentum and Velocity Profiles

A more general form of Equation A.1 may be used to determine the amount of angular momentum (H) that is absorbed by the payload during torquing. An equal and opposite amount of angular momentum is absorbed by the actuator.

$$\tau(t) = \frac{d}{dt}[H(t)] \tag{A.3}$$

$$H(t) = \int_0^t \tau(\xi) \cdot d\xi \tag{A.4}$$

Equation A.4 is readily integrated with respect to the dummy variable (ξ) in order to provide expressions for the time history of the angular momentum stored in the payload.

(acceleration)
$$H(t) = \tau_C \cdot t \tag{A.5a}$$

(deceleration)
$$H(t) = \tau_C (T_S - t) \tag{A.5b}$$

For the single-axis case, the angular velocity (Ω) and angular

momentum are related by the inertia of the payload about the axis of rotation.

$$H(t) = I_S \cdot \Omega(t) \tag{A.6}$$

The maximum values of the angular momentum (H_m) and angular velocity (Ω_m) occur at the midpoint ($t = T_S/2$) of the maneuver as is shown in Figure 51(a) and 51(b). The former quantity is the required angular momentum storage capacity of the slew actuator.

$$H_S = H(\frac{1}{2} T_S) = I_S \cdot \Omega_m = \frac{1}{2} \tau_C \cdot T_S \tag{A.7}$$

A.1.3 Angular Position of the Payload

The angular velocity of the payload is the time rate of change of the angular position (θ) of the payload about the slew axis.

$$\Omega(t) = \frac{d}{dt} [\theta(t)] \tag{A.8}$$

$$\theta(t) = \int_0^t \Omega(\xi) \cdot d\xi \tag{A.8}$$

This equation is readily integrated to provide expressions for the angular position of the payload as a function of time. The angular position is plotted in Figure 52.

(acceleration) $$\theta(t) = \frac{\tau_C}{2 \cdot I_S} t^2 \tag{A.9a}$$

(deceleration) $$\theta(t) = \frac{\tau_C}{4 \cdot I_S} [4T_S t - 2t^2 - T_S^2) \tag{A.9b}$$

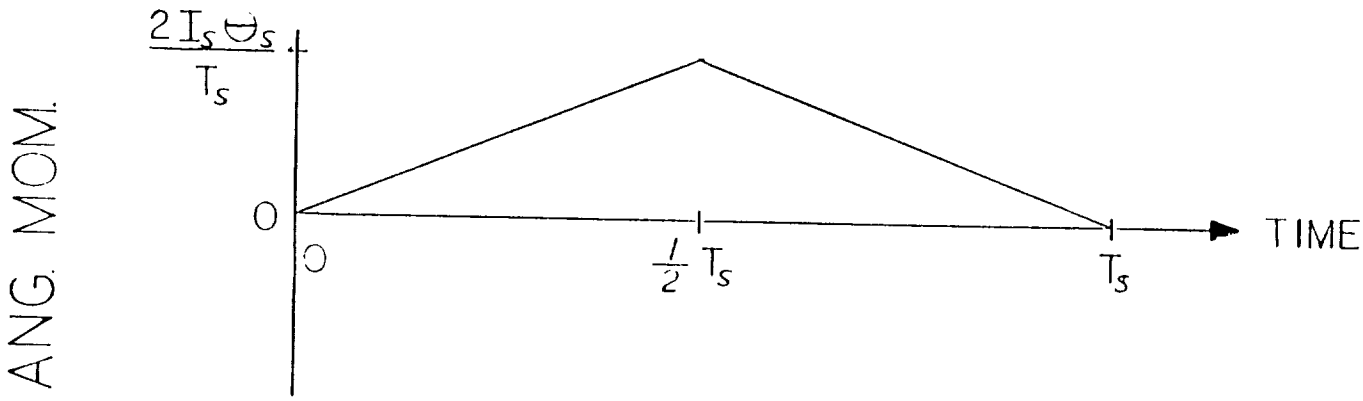

a) Angular Momentum Profile

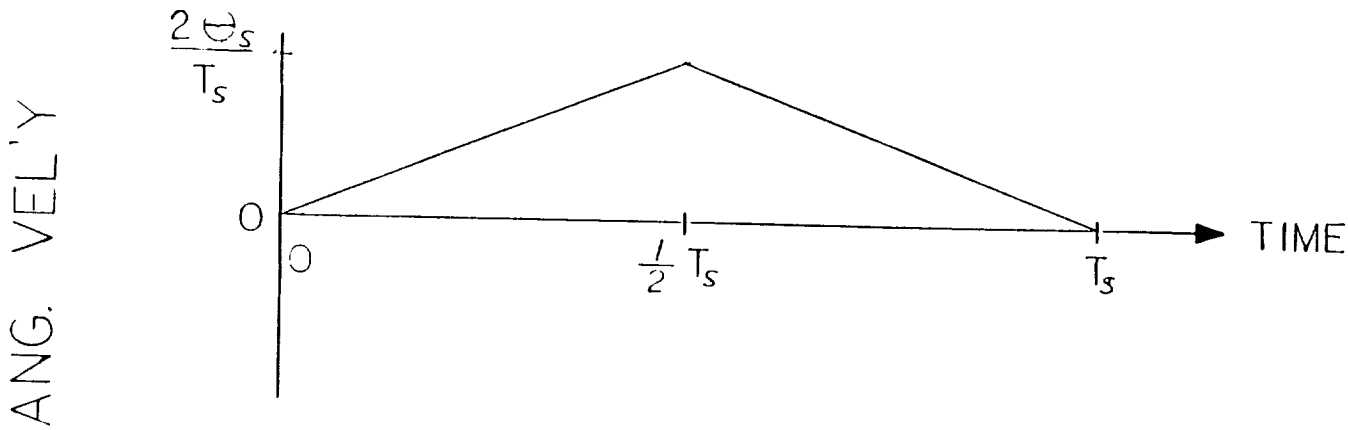

b) Angular Velocity

Figure 51. Angular Momentum and Velocity Profiles

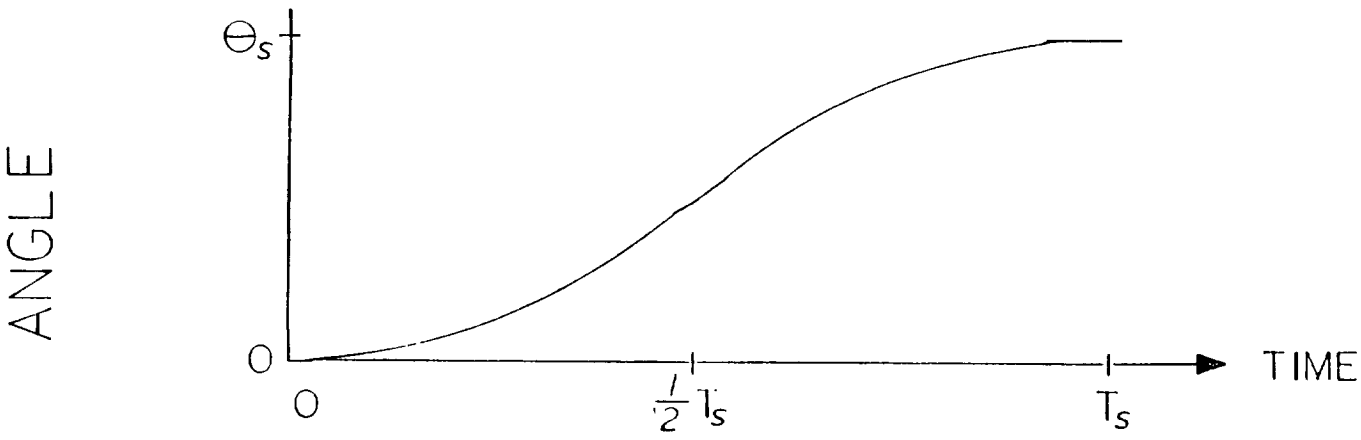

Figure 52. Angular Position Profile

The angular position of the payload at the end of the slew is the desired slew amplitude (θ_s).

$$\theta_s = \theta(T_s) = \frac{\tau_c \cdot T_s^2}{4 \cdot I_s} \qquad (A.10)$$

A.1.4 Mechanical Power

The mechanical power (P) delivered to the payload is the product of the torque angular velocity as shown in Figure 53.

$$P(t) = \tau_c \cdot \Omega(t) \qquad (A.11)$$

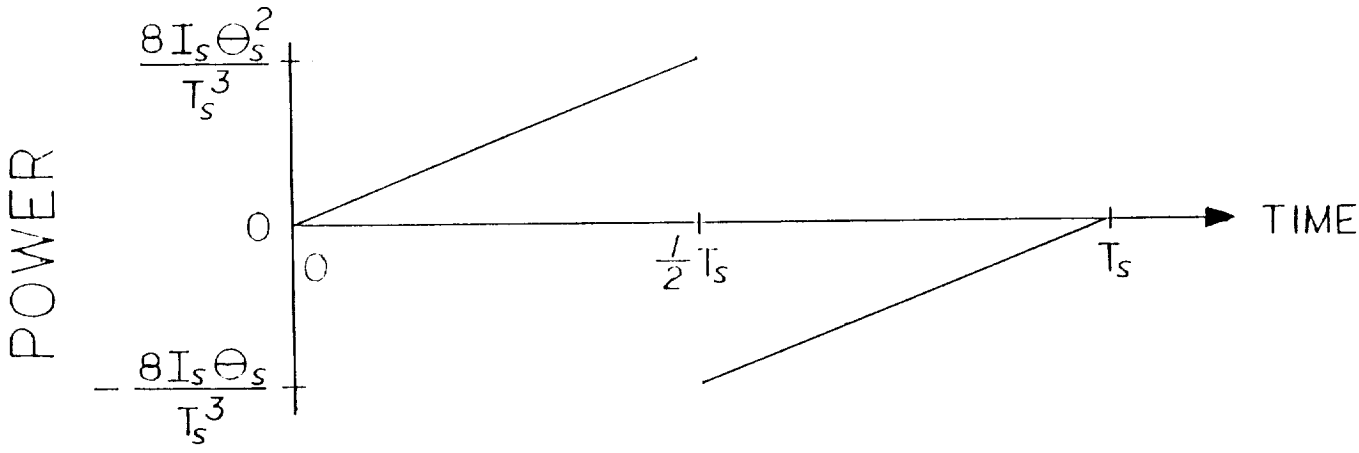

Figure 53. Mechanical Power Profile

(acceleration) $$P(t) = \frac{\tau_c^2}{I_s} t \qquad \text{(A.12a)}$$

(deceleration) $$P(t) = -\frac{\tau_c^2}{I_s} [T_s - t] \qquad \text{(A.12b)}$$

The maximum value (P_s) occurs at the midpoint of the slew. This quantity sizes the power handling capability of the actuator.

$$P_m = P(\frac{1}{2} T_s) = \frac{\tau_c^2 \cdot T_s}{2 \cdot I_s} \qquad \text{(A.13)}$$

A.1.5 Actuator Requirements

Equations A.7, A.10, and A.13 are best used to fix the hardware requirements for the actuator (τ_s,H_s,P_s) as a function of the slew parameters (θ_s,T_s).

$$\theta_s,\ T_s = \text{Given} \tag{A.14a}$$

$$\tau_c = \frac{4I_s\theta_s}{T_s^2} \tag{A.14b}$$

$$H_m = \frac{2I_s\theta_s}{T_s} \tag{A.14c}$$

$$P_m = \frac{8I_s\theta_s^2}{T_s^3} \tag{A.14d}$$

These equations are used in Chapter 2 to provide specifications for the slew actuator.

A.2 Precession Torques for Scissored-pair CMGs

The section analyzes the mechanism by which a scissored pair of CMGs exchanges angular momentum with a payload. The CMGs are modelled as flywheels with fixed spin rates, but variable orientation with respect to the payload. A bang-bang command shape is assumed. Figure 10 showed the basic scissored-pair CMG configuration. Two initially counter-rotating flywheels, each having spin-axis angular momentum (h_f) precess through an angle (δ) in a plane in order that the net momentum of the payload (H) and the flywheels is zero.

$$H(t) = I_s\Omega(t) = 2h_f \sin\delta(t) = \tau_c t \tag{A.15}$$

The plane which contains the spin axes of the flywheels rotates at the angular rate of the payload (Ω). The Law of Coriollis [38] requires that a precession torque (τ_p) be applied to cause its spin axis to follow the payload.

$$\begin{aligned} \tau_p(t) &= \Omega(t) \times h_f \\ &= \Omega(t) h_f \sin [\pi/2 + \delta(t)] \\ &= \Omega(t) h_f \cos \delta(t) \end{aligned} \qquad \text{(A.16)}$$

The required spin-axis angular momentum is specified by the maximum angular momentum of the payload (H_m) and the maximum gimbal angle (δ_{max}).

$$H_m = 2 h_f \sin \delta_{max} = \frac{T_c T_s}{2} \qquad \text{(A.17)}$$

$$h_f = \frac{t_c T_s}{4 \sin \delta_{max}} \qquad \text{(A.18)}$$

If Equation A.18 is substituted into Equation A.15, the time history of the gimbal angle during the acceleration phase of the slew can be determined.

$$\tau_c t = \frac{\tau_c T_s}{2} \left[\frac{\sin \delta(t)}{\sin \delta_{max}} \right]$$

$$\sin \delta(t) = \sin \delta_{max} \frac{2t}{T_s} \qquad \text{(A.19)}$$

The third form of Equation A.19 can now be written in terms of the maximum gimbal angle, maximum control torque, and slew maneuver parameters

$$\tau_p(t) = \frac{H(t)}{I_s} h_f \cos \delta(t)$$

$$= \frac{\tau_c t}{I_s} \frac{H_m}{2 \sin \delta_{max}} \cos \delta(t) \qquad (A.20)$$

$$= \frac{\tau_c t \theta_s}{T_s \sin \delta_{max}} \cos \delta(t)$$

$$= \frac{\tau_c \theta_s}{\sin \delta_{max}} \frac{t}{T_s} \left[1 - \left(\frac{2t}{T_s} \right)^2 \sin^2 \delta_{max} \right]^{1/2}$$

There will be a time, during the slew maneuver, when the precession torque is a maximum. The time at which the maximum torque occurs (t_m) can be found by differentiating the last form of Equation A.20 with respect to t and setting the result to zero.

$$t_m = \frac{T_s}{2 \sqrt{2} \sin \delta_{max}} \qquad (A.21)$$

When this value of time is substituted into the last form of Equation A.20, an expression for the maximum precession torque (τ_{pm}) results.

$$\tau_{pm} = \tau_p(t_m) = \frac{\tau_c \theta_s}{4 \sin^2 \delta_{max}} \qquad (A.22)$$

This result is used in Chapter 3 to specify the maximum gimbal angle for the slew actuator.

A.3 Power Requirements

The maximum power requirement shown in Equation A.14d is the mechanical power which must be delivered to the payload. An

external power source such as that shown in Figure 54 would have to supply the mechanical power requirement and any internal losses within the actuator. This section analyzes the power supply requirements for the slew actuator. The bang-bang command shape is again assumed.

A.3.1 Requirements without Energy Storage

When no energy storage is present, the power flow described in Figure A.6 can be analyzed as a quasi-steady-state process. During acceleration, the power delivered by the supply (P_S) must meet both the load demand and the losses within the actuator. The actuator losses are modelled by considering the device to have a constant efficiency (η_C).

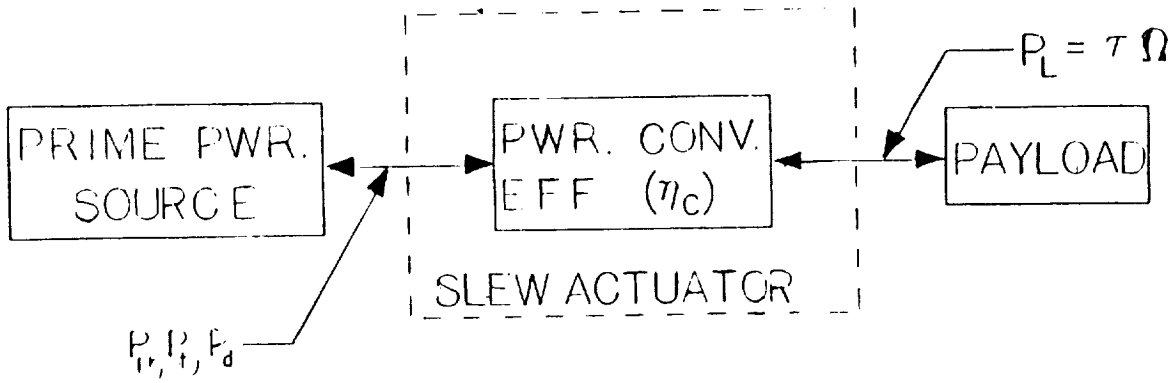

Figure 54. Power Flow for Slew Actuator without Energy Storage

$$\eta_C P_S(t) = \tau_C \Omega(t) \tag{A.23}$$

$$P_S(t) = \frac{16\, I_S \theta_S^2}{\eta_C T_S^4}\, t = \frac{2P_m t}{\eta_C T_S} \tag{A.24}$$

During deceleration, the supply must sink the difference between the power derived from the payload and the losses.

$$P_S(t) = \eta_C \tau_C \Omega(t) \tag{A.25}$$

$$P_S(t) = \frac{-16\eta_C I_S \theta_S^2}{T_S^4}\,(T_S - t) \tag{A.26}$$

$$= -\frac{2P_m \eta_C}{T_S}\,(T_S - t)$$

The peak power delivered by the supply (P_{pk}) occurs at the end of the acceleration phase of the slew maneuver.

$$P_{pk} = P_S\left(\frac{T_S}{2}\right) = \frac{P_m}{\eta_C} \tag{A.27}$$

The average power (P_d) delivered by the prime source during a slew maneuver is defined as follows.

$$P_d T_S = \int_0^{T_S} P_S(t)\, dt \tag{A.28}$$

The average power is that amount of power which the source would have to supply continuously in order to transfer the same amount of energy. When Equations A.24 and A.26 are substituted into Equation A.28 and the integration is performed, a simple expression for the average power results.

$$P_d = P_m \frac{1 - \eta_c^2}{4\eta_c} = P_{pk} \frac{1 - \eta_c^2}{4} \tag{A.29}$$

Equation A.29 implies that in the limit as the conversion efficiency approaches unity, no average power is delivered by the prime source. This, of course, assumes that the kinetic energy of the payload may be recovered for later use.

A better measure of the prime source is the average power transferred. This is a measure of the power handling capability of the supply.

$$P_{avg}T_s = \int_0^{T_s} |P_s(t)|\, dt \tag{A.30}$$

$$P_{avg} = P_m \frac{1 + \eta_c^2}{4\eta_c} = P_{pk} \frac{1 + \eta_c^2}{4} \tag{A.31}$$

Equation A.31 implies that, even if the conversion is perfect, the power handling components have to be sized for half of the peak power.

A.3.2 Requirements with Energy Storage

Figure 55 describes a configuration in which a unidirectional prime source provides a continuous power input (P_C) during the slew. The energy required for the slew is extracted from a storage during acceleration and returned during deceleration. The continuous power input makes up for dissipative losses. This section analyzes the dynamics of this system.

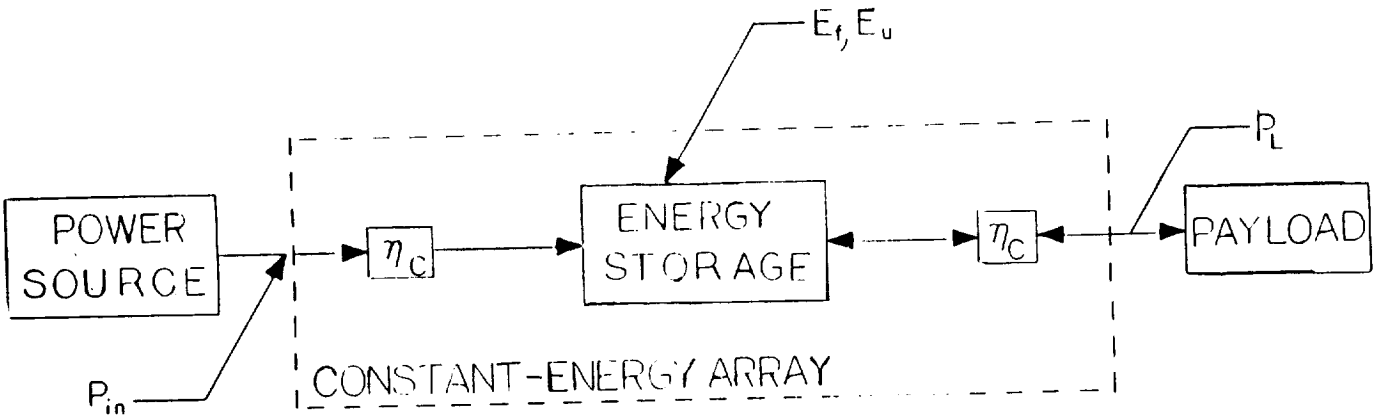

Figure 55. Power Flow for Slew Actuator with Energy Storage

A.3.2.1 Acceleration. During acceleration of the payload, the amount of energy stored (E) is increased by the power input and reduced by load power.

$$\frac{dE(t)}{dt} = \eta_c P_c - \frac{2P_m t}{\eta_c T_s} \tag{A.32}$$

$$E(t) - E(o) = \int_0^t (\eta_c P_c - \frac{2P_m t}{\eta_c T_s}) \, dt \tag{A.33}$$

Assuming that the energy storage device is initially charged to its full capacity (E_s), Equation A.33 is readily integrated to provide an expression for the state of charge as a function of time.

$$E(0) = E_s \tag{A.34}$$

$$E(t) = E_s + \eta_c P_c t - \frac{P_m t^2}{\eta_c T_s} \tag{A.35}$$

At the end of the acceleration phase of the slew, some fraction (the depth of discharge, η_{dod}) of the stored energy will have been extracted. This is the useful capacity of the energy storage device.

$$E(\frac{T_s}{2}) = (1 - \eta_{dod})E_s = E_s + \frac{\eta_c P_c T_s}{2} - \frac{P_m T_s}{4\eta_c} \tag{A.36}$$

$$E_u = \frac{P_m T_s}{4\eta_c} - \frac{\eta_c P_c T_s}{2} \tag{A.37}$$

A.3.2.2 Deceleration. During the deceleration phase of the slew, both the continuous power input and the energy recovered from the payload act to recharge the energy storage device.

$$\frac{dE(t)}{dt} = \eta_C P_C + \frac{2P_m\eta_C}{T_S}(T_S - t) \qquad (A.38)$$

$$E(t) - E(\frac{T_S}{2}) = \int_{T_S/2}^{t} \eta_C P_C + \frac{2P_m\eta_C}{T_S}(T_S - t)\, dt \qquad (A.39)$$

Using Equation A.36 to represent the initial state of charge for the deceleration phase, Equation A.39 is readily integrated.

$$E(t) = E_S + \eta_C P_C t + P_m\left(- \frac{\eta_C t^2}{T_S} + 2\eta_C t - \frac{3}{4}\eta_C T_S - \frac{T_S}{4\eta_C} \right) \qquad (A.40)$$

At the end of the deceleration phase, the energy storage device should be at its full state of change.

$$E(T_S) = E_S = E_S + \eta_C P_C T_S - P_m T_S \left(\frac{1}{4\eta_C} - \frac{\eta_C}{4} \right) \qquad (A.41)$$

A.3.2.3 Requirements. The required continuous power input can now be determined as a function of the maximum mechanical power and the conversion efficiency.

$$P_C = P_m \frac{1 - \eta_C^2}{4\eta_C} \qquad (A.42)$$

Equation A.42 can then be substituted into Equation A.37 to provide a similar expression for the required useful energy storage capacity.

$$E_u = P_m T_s \frac{1 + \eta_c^2}{8\eta_c} \tag{A.43}$$

The full and useful capacities of the energy storage device are related by the depth of discharge.

$$E_s = \frac{E_u}{\eta_{dod}} = P_m T_s \frac{1 + \eta_c^2}{8\eta_c \eta_{dod}} \tag{A.44}$$

APPENDIX B. SIZING PROCEDURE FOR ANNULAR COMPOSITE FLYWHEELS

This appendix summarizes a procedure for sizing an annular composite flywheel which will store a given amount of kinetic energy at a given rotational speed. Figure 18 showed a cut-away drawing of an annular flywheel which is used to present the parameters which describe the geometry of the flywheel.

The sizing procedure is based on a macroscopic model for the composite material [39]. The maximum radial stress in the flywheel is limited to the recommended working strength of the matrix material, while the maximum tangential stress is limited to the recommended working strength of the filament.

B.1 Stress Analysis

Closed-form solutions for the radial (σ_r) and tangential (σ_θ) stresses in a rotating annulus are readily available in a number of textbooks [19]. The present analysis begins with expressions for the maximum values (σ_{rm}, $\sigma_{\theta m}$) of these stresses in terms of the density of the material (D_m), the Poisson's ratio of the material (μ), peripheral speed of the flywheel (v), and the radial aspect ratio (ID/OD = α).

$$\sigma_{rm} = D_m v^2 \frac{(3 + \mu)}{8} (1 - \alpha)^2 \qquad (B.1)$$

$$\sigma_{\theta m} = D_m v^2 \frac{(3 + \mu)}{4} \left[1 + \frac{(1 - \mu)}{(3 + \mu)} \alpha^2\right] \qquad (B.2)$$

The kinetic energy (e) which is stored in the flywheel is easily related to the mass (m), the moment of inertia (I), the radius (r), and the rotational speed (ω).

$$e = \frac{1}{2} I \omega^2 \tag{B.3}$$

$$= \frac{mv^2}{4} (1 + \alpha^2) \tag{B.4}$$

The energy density (D_e) of the flywheel is simply the ratio of the kinetic energy to the mass [18].

$$D_e = \frac{e}{m} = \frac{1}{4} v^2 (1 + \alpha^2) \tag{B.5}$$

When Equation B.5 is solved for the peripheral velocity and the result is substituted into Equations B.1 and B.2, equations for the maximum stresses in the flywheel, in terms of the energy density, are obtained.

$$\sigma_{rm} = D_e D_m \frac{(3 + \mu)}{2} \frac{(1 - \alpha)^2}{(1 + \alpha^2)} \tag{B.6}$$

$$\sigma_{\theta m} = D_e D_m \frac{[(3 + \mu) + (1 - \mu)\alpha^2]}{(1 + \alpha^2)} \tag{B.7}$$

B.2 Stress-limited Designs

In order to design a flywheel which stores a given amount of kinetic energy, the energy density should be maximized subject to the constraint that the maximum stresses are less than or equal to working levels (σ_{rw} and $\sigma_{\theta w}$). In general, for a given aspect ratio, only one of the stress components may be arbitrarily

assigned. For a given radial aspect ratio (α), the optimum energy density causes one of the stress components to be at its working level and the other stress component to be less than its working value. In order to accomplish this analysis, both radial-stress- and hoop-stress-limited cases are considered.

B.2.1 Radial-stress-limited Flywheel

A radial-stress-limited flywheel ($\sigma_{rm} = \sigma_{rw}$) will be an acceptable design if the hoop maximum stress is less than the working hoop stress ($\sigma_{\theta m} < \sigma_{\theta w}$). Equation B.6 is readily solved to yield an expression for the energy density of a radial-stress-limited flywheel.

$$D_{er} = \frac{\sigma_{rw}}{D_m} \left[\frac{1 + \alpha^2}{(1 - \alpha)^2}\right] \left(\frac{2}{3 + \mu}\right) \tag{B.8}$$

This result can now be substituted into Equation B.7 and the result divided by the working hoop stress to obtain a normalized hoop stress.

$$\left.\frac{\sigma_{\theta m}}{\sigma_{\theta w}}\right|_{\sigma_{rm} = \sigma_{rw}} = \left(\frac{2\,\sigma_{rw}}{\sigma_{\theta w}}\right) \frac{[(3 + \mu) + (1 - \mu)\alpha^2]}{(3 + \mu)(1 - \alpha)^2} \tag{B.9}$$

When this ratio is less than unity, the design is acceptable.

B.2.2 Hoop-stress-limited Flywheel

A hoop-stress-limited flywheel ($\sigma_{\theta m} = \sigma_{\theta w}$) will be an acceptable design if the hoop maximum stress is less than the working radial stress ($\sigma_{rm} < \sigma_{rw}$). The equations for this case

which are analogous to Equations B.8 and B.9 are given below.

$$D_{e\theta} = \left(\frac{\sigma_{\theta w}}{D_m}\right) \frac{(1 + \alpha^2)}{[(3 + \mu) + (1 - \mu)\alpha^2]} \qquad \text{(B.10)}$$

$$\left.\frac{\sigma_{rm}}{\sigma_{rw}}\right|_{\sigma_{\theta m} = \sigma_{\theta w}} = \left(\frac{\sigma_{\theta w}}{2\,\sigma_{rw}}\right) \frac{(3 + \mu)(1 - \alpha)^2}{[(3 + \mu) + (1 - \mu)\alpha^2]} \qquad \text{(B.11)}$$

B.2.3 Cross-over Aspect Ratio

For given material properties, the aspect ratio of the flywheel will determine whether the design is limited by the radial or hoop stress. Figure 56 shows Equations B.9 and B.11 plotted with the aspect ratio of the flywheel. At the cross-over aspect ratio (α_o), the maximum radial and hoop stresses in the flywheel are at their working levels. For flywheels which are have a thick-walled cross section ($\alpha < \alpha_o$), the flywheel design is limited by radial stresses. For thin-walled flywheels ($\alpha > \alpha_o$), hoop stresses limit the flywheel design. Figure 57 shows the resulting energy density for a graphite/epoxy flywheel.

B.3 Flywheel Sizing

The parameters which describe the flywheel design (mass, peripheral speed, and physical dimensions) are obtained in a relatively straight-forward manner. This section contains the equations which relate these parameters.

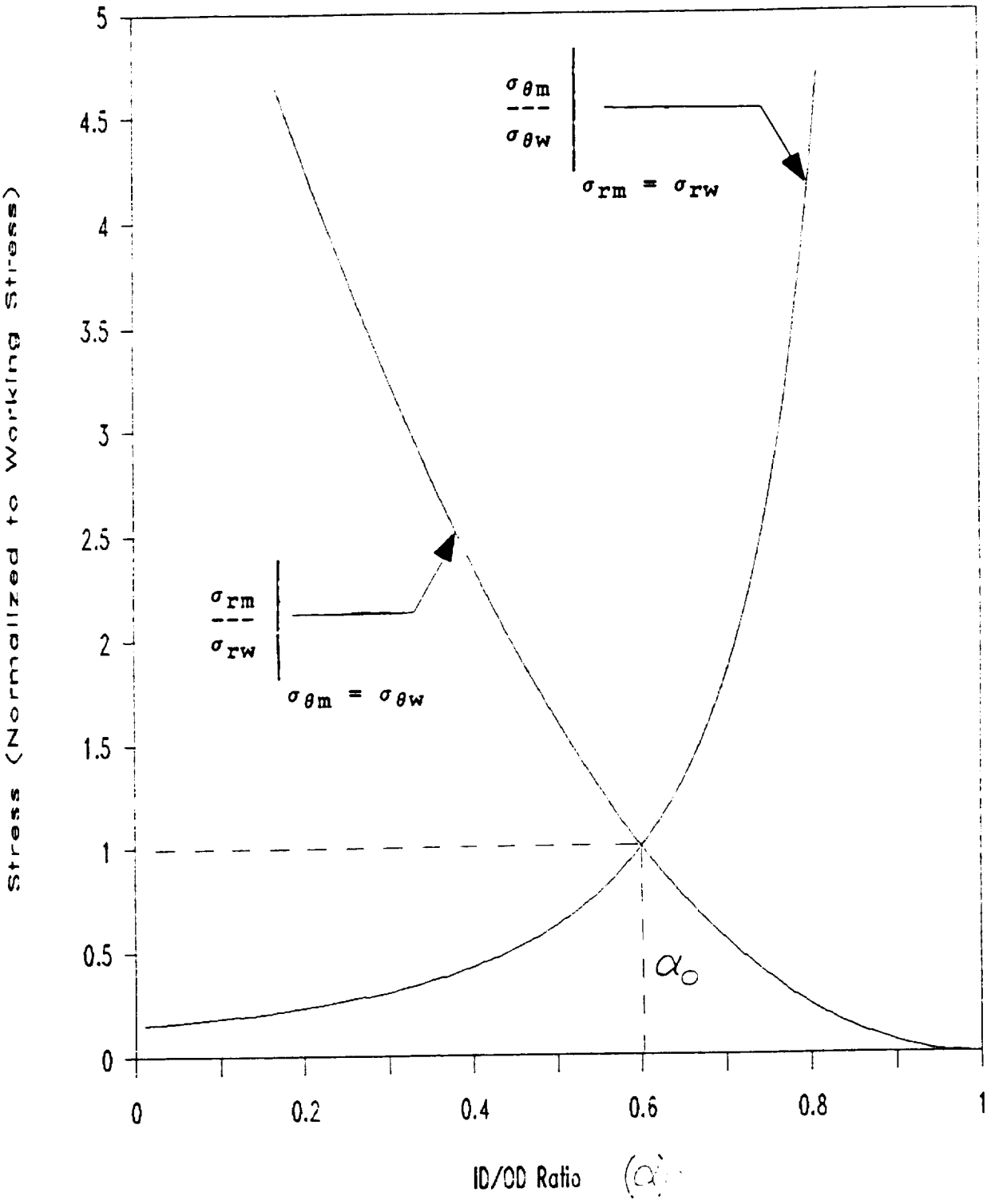

Figure 56. Stresses in an Annular Flywheel

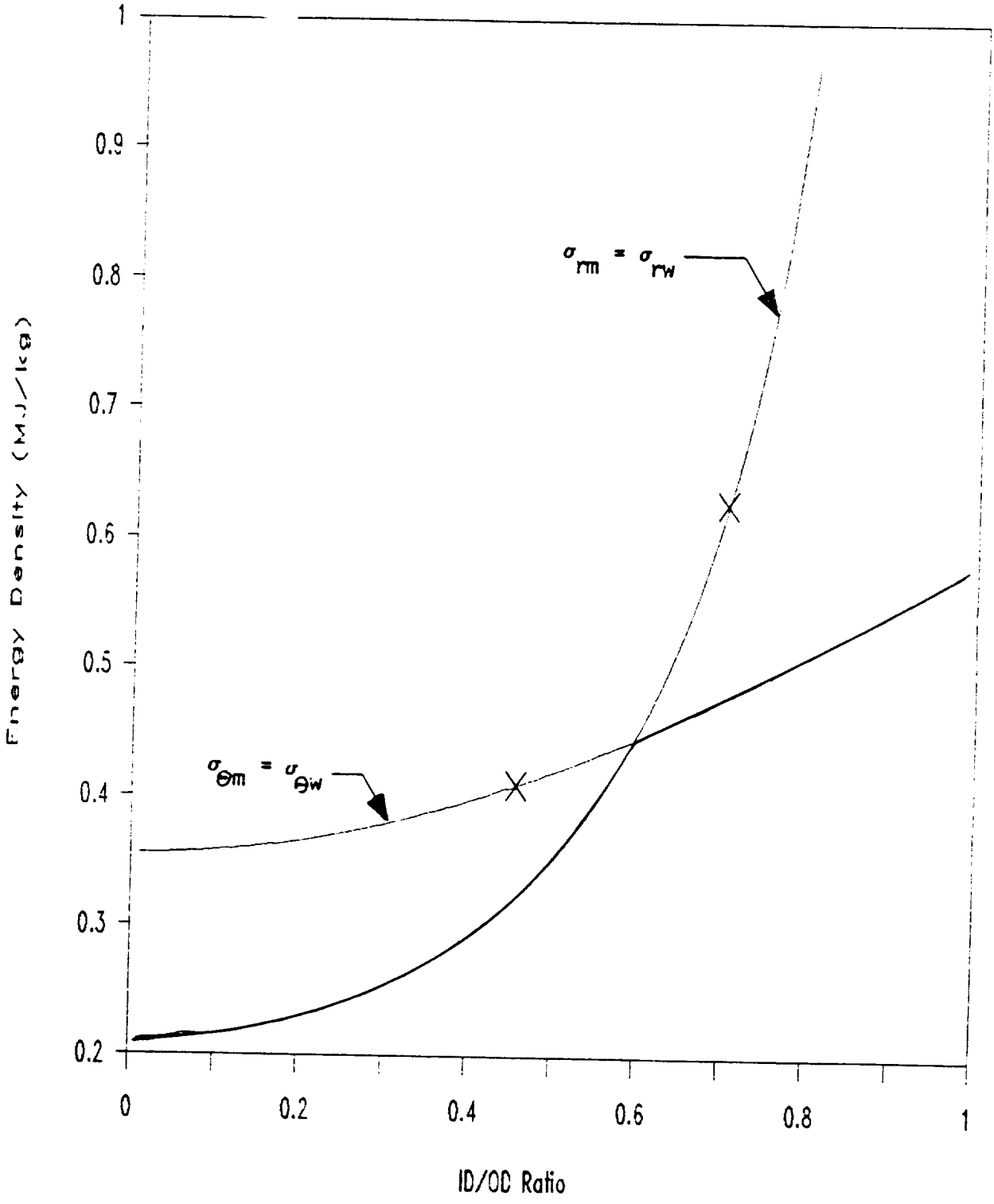

Figure 57. Energy Density of an Annular Flywheel

The maximum peripheral speed of the flywheel is related to the energy density by Equation B.5. This is readily rearranged to yield the following expression.

$$v = 2 \left[\frac{D_e}{1 + \alpha^2}\right]^{(1/2)} \tag{B.12}$$

The outer radius (r_o) of the flywheel is determined from the maximum peripheral speed and the maximum rotational speed.

$$r_o = \frac{v}{\omega} \tag{B.13}$$

The inner radius of the flywheel is fixed by the specified radial aspect ratio of the flywheel.

$$r_i = \alpha\ r_o \tag{B.14}$$

The mass of flywheel needed to store the required amount of kinetic energy is used to determine the axial length (l) of the flywheel.

$$m = \frac{e}{D_e} = \pi\ D_m\ [(r_o)^2 - (r_i)^2]\ l \tag{B.15}$$

$$l = \frac{m}{\pi\ D_m\ [(r_o)^2 - (r_i)^2]} \tag{B.16}$$

NASA
National Aeronautics and Space Administration

Report Documentation Page

1. Report No.	2. Government Accession No.	3. Recipient's Catalog No.
NASA CR-4179		

4. Title and Subtitle	5. Report Date
An Advanced Actuator for High-Performance Slewing	September 1988
	6. Performing Organization Code

7. Author(s)	8. Performing Organization Report No.
James Downer, David Eisenhaure, and Richard Hockney	R05-87
	10. Work Unit No.
	506-46-11-01

9. Performing Organization Name and Address	11. Contract or Grant No.
SatCon Technology Corporation 71 Rogers Street Cambridge, MA 02142	NAS1-18322
	13. Type of Report and Period Covered
	Final Contractor Report

12. Sponsoring Agency Name and Address	14. Sponsoring Agency Code
National Aeronautics and Space Administration Langley Research Center Hampton, VA 23665-5225	

15. Supplementary Notes

Langley Technical Monitor: C. R. Keckler

16. Abstract

A conceptual design for an advanced momentum exchange actuator for application to spacecraft slewing is described in this report. The particular concept is a magnetically-suspended, magnetically gimballed control moment gyro (CMG). A scissored pair of these devices is sized to provide the torque and angular momentum capacity required to reorient a large spacecraft through large angle maneuvers.

The concept described herein utilizes a composite material rotor to achieve the high momentum and energy densities to minimize system mass, an advanced superconducting magnetic suspension system to minimize system weight and power consumption. The magnetic suspension system is also capable of allowing for large angle "gimballing" of the rotor, thus eliminating the mass and reliability penalties attendant to conventional gimbals. Descriptions of the various subelement designs are included in this document along with the necessary system sizing formulation and material.

17. Key Words (Suggested by Author(s))	18. Distribution Statement
Magnetic suspension, Superconducting magnetic bearing, large angle magnetic suspension, momentum exchange device, large angle maneuver, control of large spacecraft	Unclassified - Unlimited Subject Category 31

19. Security Classif. (of this report)	20. Security Classif. (of this page)	21. No. of pages	22. Price
Unclassified	Unclassified	168	A08

NASA FORM 1626 OCT 86 For sale by the National Technical Information Service, Springfield, Virginia 22161-2171 NASA-Langley, 1988

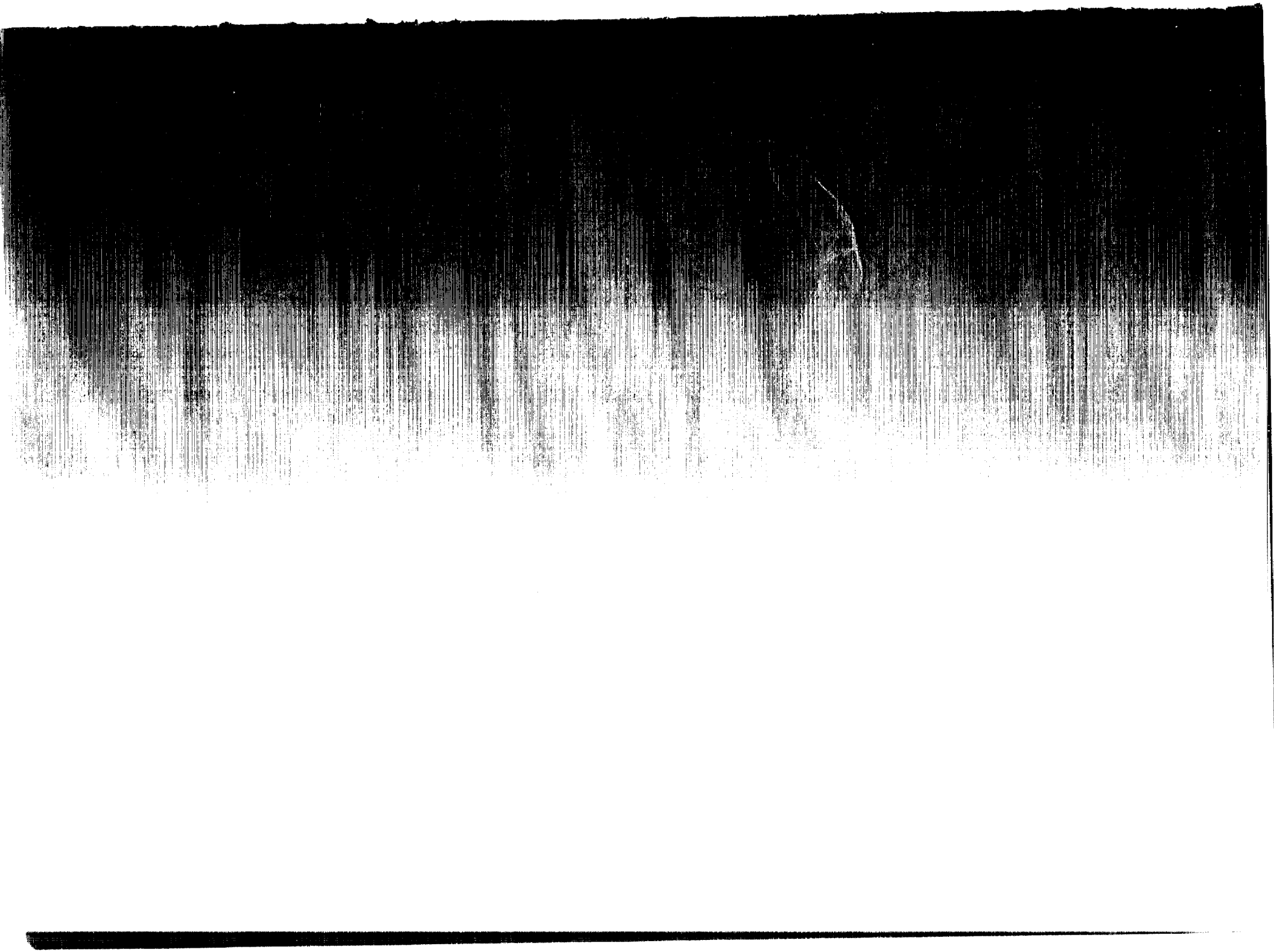

National Aeronautics and
Space Administration
Code NTT-4

Washington, D.C.
20546-0001

Official Business
Penalty for Private Use, $300

NASA

National Aeronautics and
Space Administration

Washington, D.C.
20546

Postage and Fees Paid
National Aeronautics and
Space Administration
NASA-451

Official Business
Penalty for Private Use $300

SPECIAL FOURTH CLASS MAIL
BOOK

NASA
SCIEN & TECH INFO FACILITY
ACCESSIONING DEPT
P O BOX 8757 BWI AIRPT
BALTIMORE MD 21240

NASA